FROM SINGLE CELLS TO THE BRAIN: ELECTROCHEMICAL IMAGING OF TRANSMITTER RELEASE

A Dissertation

Presented to the Faculty of the Graduate School

of Cornell University

in Partial Fulfillment of the Requirements for the Degree of

Doctor of Philosophy

by

Khajak Nazaret Barbarian

May 2009

FROM SINGLE CELLS TO THE BRAIN: ELECTROCHEMICAL IMAGING OF TRANSMITTER RELEASE

Khajak Nazaret Barbarian, Ph.D.

Cornell University 2009

The main object of study of this dissertation is neurotransmitter release, a fundamental biological process implicated in memory and learning, emotions and behavior, as well as many other crucial cellular functions. Transmitter release is impaired in many diseases of the nervous system, including neurodegenerative diseases.

Chapter 1 is an introduction to the mechanism of transmitter release by exocytosis and related biological concepts studied in the current work. The physicochemical techniques utilized to study exocytosis are introduced in Chapter 2. The roles of filamentous actin and nonmuscle myosin II in chromaffin cell exocytosis as examined by fluorescence microscopy, amperometry and cell-attached capacitance methods are analyzed in Chapter 3. Improved microfabricated electrochemical detector arrays, and their utilization in novel single cell measurements are demonstrated in Chapter 4. Chapter 5 describes random walk simulations and time domain deconvolution methods for modeling transmitter release and diffusion. Monitoring dopamine levels in the brain of freely moving research animals using a wired setup is presented in Chapter 6. Also in Chapter 6, the initial development of a wireless sensor for monitoring *in vivo* levels of dopamine is demonstrated.

BIOGRAPHICAL SKETCH

The author graduated from the Department of Electrical and Computer Engineering, at the National Technical University of Athens (NTUA), in Athens Greece in May 2002. He joined the PhD program of the Department of Biomedical Engineering at Cornell University in 2003. During his dissertation, the author developed novel electrochemical, computational and microfabrication techniques to study the biological process of exocytosis in isolated single cells, as well as in the brain of freely moving research animals.

Dedicated to my beloved parents, Nazaret and Eva.

ACKNOWLEDGEMENTS

I am indebted to many people who helped me in the process of completing my dissertation. I would like to express my particular gratitude to:

Prof. Manfred Lindau, for being an inspirational and patient thesis advisor, and teaching me critical thinking and perseverance. Prof. David L. Deitcher and Prof. Abraham D. Stroock, for serving on my thesis committee.

Prof. M.G. Kaplitt at the Weill Medical College of Cornell University, Prof. D. Sulzer at Columbia University, and Prof. R.M. Wightman at the UNC Chapel Hill for the opportunity to visit and work in their labs. Dr. E.V. Mosharov for help with single cell electrochemistry. Prof. G.M. Malliaras for his advice and support. Prof. N.K. Uzunoglu at the NTUA, for supporting my applications to attend graduate school in the United States.

The Lindau group members, in particular Dr. Qinghua Fang for assistance with the patch-capacitance technique and his great friendship, Joan Lenz for keeping the lab in order, Kassandra Kisler for help with the fluorescence measurements, and Dr. Ray Molloy for helpful discussions. The Cornell NanoScale Facility staff, in particular D. Woodie, Dr. M. Guillorn and Dr. R. Ilic for help with the microfabrications. The administrative assistants and the staff of the machine shop at Cornell University's School of Applied and Engineering Physics and Department of Biomedical Engineering.

The Armenian community of Ithaca for the memorable times. Prof. Vahakn Dadrian, Prof. Yervant Terzian and Prof. Vatche Sahakian for their invaluable support. Dr. Andre Mkhoyan, whose friendship and advice were priceless. Olga Escanilla, for the great moments we shared in Ithaca.

My parents, Nazaret and Eva, my siblings, Shaghig and Hrag, my aunt, Ani for all their love and support.

TABLE OF CONTENTS

LIST OF TABLES

LIST OF FIGURES

CHAPTER 1

INTRODUCTION

1.1 Exocytosis

The communication between neurons is currently one of the more fascinating subjects in cell biology (Fig. 1.1). A key process in neuronal communication is exocytosis, during which membrane bound vesicles fuse with the cell plasma membrane and secrete their compounds into the extracellular space [1] (Fig. 1.1 inset). Exocytosis forms a *constitutive secretory pathway* with which proteins and lipids on the vesicle membrane reconstitute the cell plasma membrane, maintaining the plasma membrane functionality. Exocytosis is also the means with which cells produce and secrete many of the glycoproteins and proteoglycans of the extracellular matrix. In addition to this constitutive pathway, which is found in all cell types, exocytosis also forms a *regulated secretory pathway*, which is found primarily in cells that are required to secrete compounds at high concentrations in response to specific stimulation. Depending on the cell type, the released compounds can be hormones, neurotransmitters, peptides, enzymes or other mediators.

Exocytosis of vesicles includes several steps, such as *trafficking*, which is the translocation of vesicles from the Golgi apparatus to the cell membrane, *tethering*, *docking* and *priming*, which associate vesicles closely with the cell plasma membrane, *fusion* of the vesicle membrane with the cell plasma membrane, and *secretion* of the intravesicular compounds into the extracellular space [2].

Key proteins in vesicle exocytosis are the SNARE (SNAP receptors, where

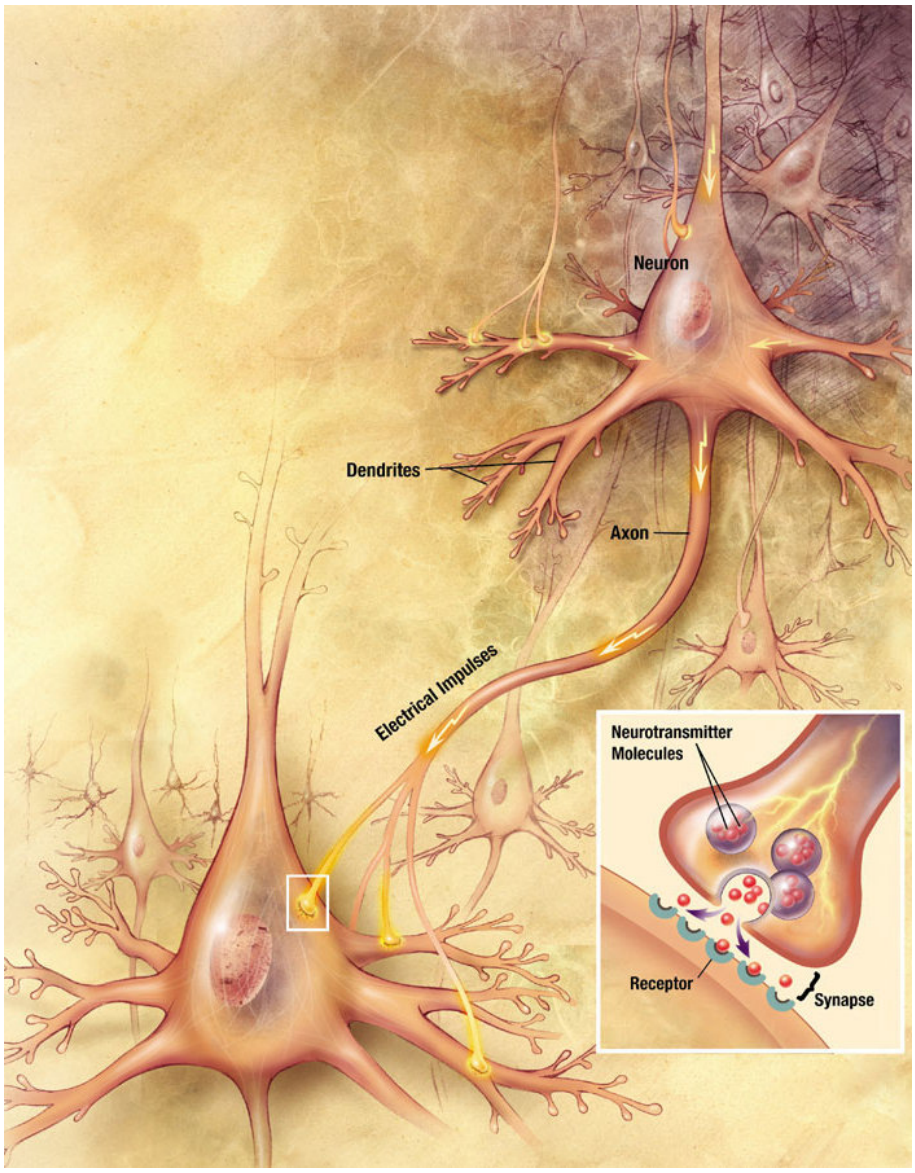

Figure 1.1: A presynaptic and a postsynaptic neuron. Inset: zoomed-in view of the synapse formed between the two neurons. Four synaptic vesicles filled with neurotransmitter molecules can be seen inside the presynaptic neuron. One of the vesicles is undergoing exocytosis, secreting neurotransmitters into the synaptic cleft. Image from the National Institutes of Health (NIH).

SNAP stands for soluble NSF-attachment protein, and NSF stands for N-ethylmaleimide-sensitive fusion protein) proteins [3]. In synaptic vesicle exocytosis the SNARE proteins include the vesicular protein VAMP (vesicle as-

sociated membrane protein), also known as Synaptobrevin, and the plasma membrane proteins Syntaxin and SNAP-25 (abbreviation for synaptosome-associated protein of mass 25 *kDa*). According to the SNARE hypothesis [4], the formation of a tight "SNARE complex" drives vesicle fusion [5]. Immediately following vesicle fusion with the cell plasma membrane, a nanometer size connection is formed between the intravesicular and the extracellular spaces, called the fusion pore [6]. Various compounds located within the vesicle are secreted into the extracellular space through the fusion pore.

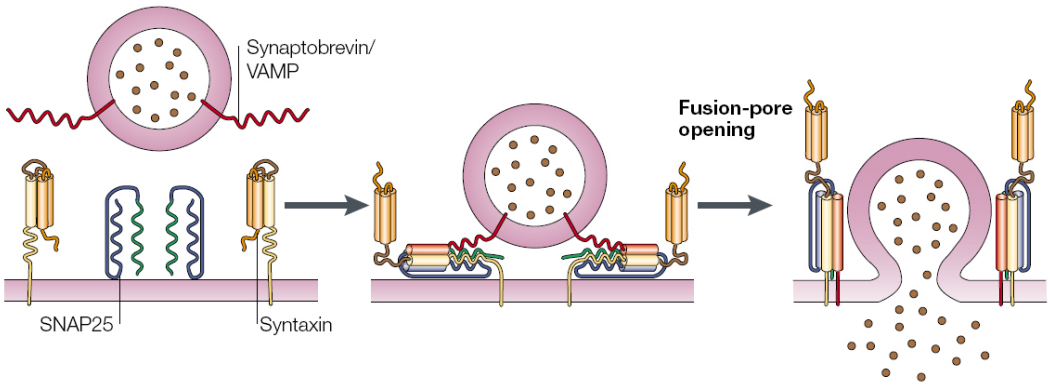

Figure 1.2: (Left) A vesicle depicted near the cell plasma membrane. The schematic shows the three SNARE proteins: VAMP or Synaptobrevin, Syntaxin and SNAP-25. (Middle) The formation of the "SNARE" complex associates the vesicle and cell plasma membranes very closely. (Rigth) The schematic shows a formed fusion pore through which molecules are secreted into the extracellular space. Figure modified from [5].

1.2 Actin and myosin II

In addition to the SNARE proteins, which play a fundamental role in vesicle exocytosis, there is a multitude of intracellular proteins which also contribute to the process of single vesicle exocytosis. One aim of the present work is to illu-

minate the role of two proteins, actin and myosin II, in the process of exocytosis.

Actin is a globular protein found in almost all eukaryotic cells. Inside the cell, actin monomers dynamically polymerize to form filamentous actin in an adenosine triphosphate (ATP) dependent manner (Fig. 1.3). Actin filaments are essential for vesicle motility, particularly when the vesicles are in close proximity to the cell plasma membrane.

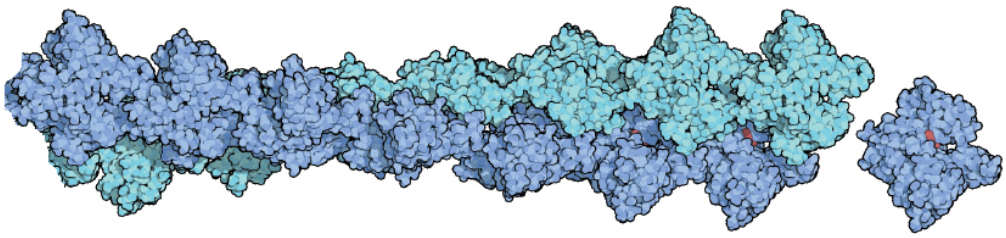

Figure 1.3: A schematic depicting an actin monomer (dark blue at the right) about to be associated with filamentous actin. Image from the Protein Data Bank.

nonmuscle myosin II is a molecular motor protein implicated in actin based vesicle motility. Fig. 1.4 shows a myosin molecule. Nonmuscle myosin II contains two heavy chains, which comprise the molecule's two heads. The two heavy chains converge to the neck region and continue to form the tail. Two light chains (one known as "regulatory" and the other as "essential") bind each heavy chain at the neck region, such that each nonmuscle myosin II molecule contains four light chains [7].

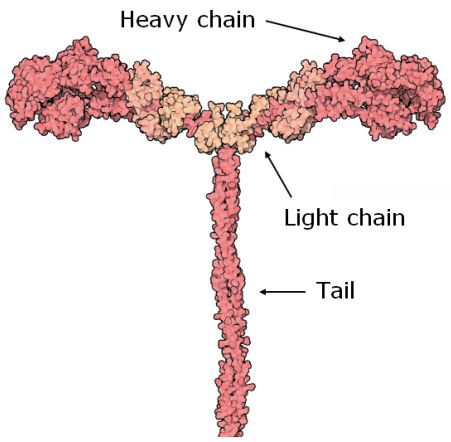

Figure 1.4: The two heads of a myosin molecule converge to the neck and form the tail. Only a small part of the tail is shown in this figure. Image from the Protein Data Bank.

1.3 Chromaffin and mast cells

Chromaffin cells (Fig. 1.5) are neuroendocrine cells, found in the medulla of the adrenal gland. These cells contain large dense core vesicles (LDCVs), which store and secrete the catecholamine hormones norepinephrine and epinephrine among other compounds. Exocytosis in chromaffin cells depends on entry of Ca^{2+} ions inside the cells. Chromaffin cells constitute a model system to study exocytosis, since the fusion of LDCVs with the cell plasma membrane can be detected via capacitance measurement techniques (see section 2.2). Moreover, LDCVs contain large amounts of electroactive catecholamines, the secretion of which can be electrochemically (see section 2.3) monitored.

Mast cells (Fig. 1.6) are part of the immune system and they are best known for their role in allergies. Mast cells are also known for their protective role, since they are involved in wound healing and defense against pathogens. In addition to being rich in histamine and heparin, mast cell granules also contain the electroactive compound serotonin, which can be electrochemically monitored.

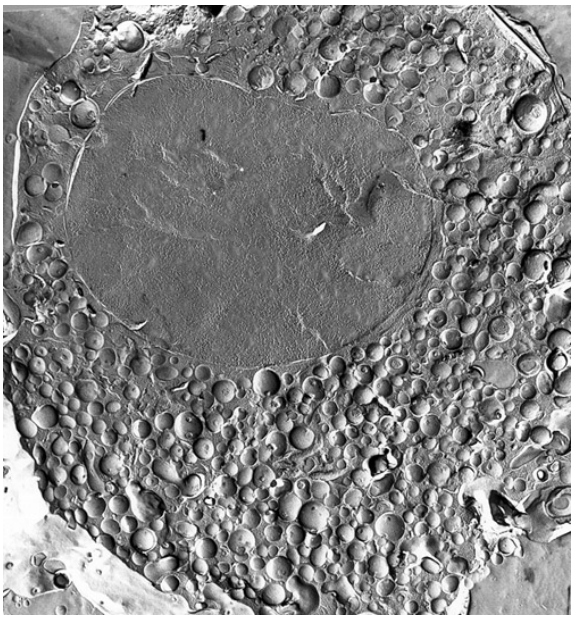

Figure 1.5: A transmission electron micrograph of a chromaffin cell. Chromaffin cells contain 20,000 to 30,000 vesicles. The large oval body is the cell nucleus. This image was obtained by quick-freezing and fracturing a chromaffin cell. The fractured surface was stained using platinum and carbon. Image from: http://webpages.ull.es/users/isccb12/ChromaffinCell/Primer.html

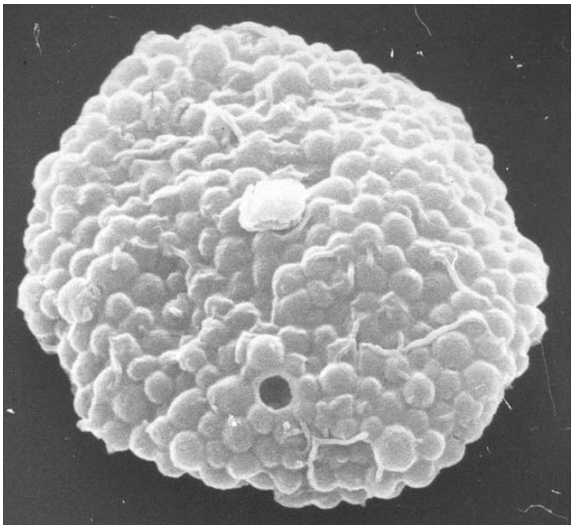

Figure 1.6: Scanning electron micrograph of a rat peritoneal mast cell. A widely open fusion pore can be seen on the cell surface. Figure from [6].

1.4 Measuring transmitter release *in vivo*

A fascinating system to study transmitter release is the brain, where neurotransmitter secretion modulates, amongst others, behavior, thought, memory, learning, sexual behavior, and drug addiction. *In vivo* measurements of the electroactive compound dopamine (DA) are particularly interesting in the striatum. The bodies of dopaminergic neurons located in the substantia nigra project their axons into the striatum (Fig. 1.7).

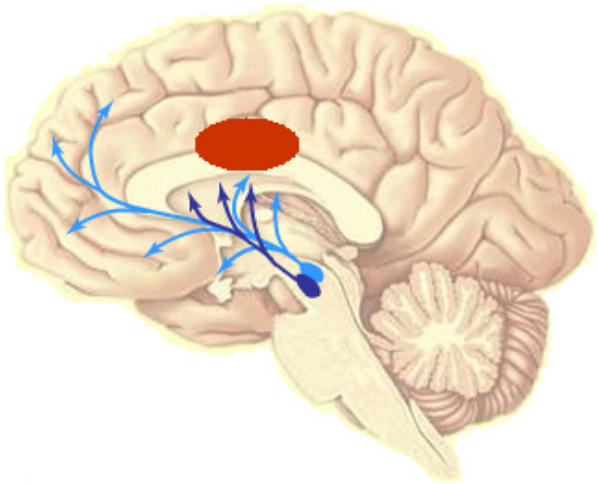

Figure 1.7: A schematic depicting the projection of dopaminergic neurons from the ventral tegmental area (light blue) and the substantia nigra pars compacta (dark blue) to the striatum (maroon). Image modified from: www.thebrain.mcgill.ca

Individual neurons secrete the neurotransmitter DA into the striatum, where DA regulates motor function. In Parkinson's disease, impaired DA release results in the symptoms characterizing the patients of this disease, such as uncontrollable tremor and slowness of movement. Although DA is electroactive and its concentration can be monitored electrochemically, the amount of DA secreted by a single neuron is very low and can not be detected. However, when

stimulated, a large number of neurons may simultaneously secrete DA into the striatum. In this case, the amount of striatal DA reaches relatively high concentrations, allowing the detection of *in vivo* DA levels using electrochemical techniques. These *in vivo* measurements have only been achieved recently in the brain of freely moving research animals [8], and have allowed researchers to correlate DA function with behavior [9].

CHAPTER 2

TECHNIQUES FOR MONITORING EXOCYTOSIS

During the late 1940s and early 1950s the pioneering work of Sir Bernard Katz and his colleagues Paul Fatt and Jose del Castillo, led to the discovery that the endplate region of skeletal muscles was the site of spontaneous electrical activity, caused by the discharge of packets of acetylcholine from nerve terminals [10]. Katz and his colleagues demonstrated that these 'miniature endplate potentials' represented the basis of chemical synaptic transmission. The recognition that transmitter release was quantal coincided with the discovery of presynaptic vesicles by electron microscopists. Katz and his colleagues related these two findings and suggested the 'vesicle hypothesis' as the underlying physical mechanism for quantal release.

Since the proposal of the 'vesicle hypothesis', vesicular fusion and release has become the object of intense research by many scientists in various educational and governmental institutions. Several techniques have been employed to investigate single exocytotic events, including epifluorescence and total internal reflection fluorescence microcopy [11, 12, 13, 14, 15], whole cell patch clamp capacitance measurements [16, 17, 18, 19], cell-attached capacitance measurements [20, 21, 22, 23], carbon fiber amperometry [24, 25, 26], and patch amperometry [27, 28, 29]. For the purposes of the present dissertation the author utilized several biophysical techniques, a brief introduction to the basic concepts of which follows.

2.1 Fluorescence microscopy

Single vesicle exocytosis can be monitored using fluorescence microscopy. Fluorescence is the physical process wherein molecular absorption of a photon leads to the subsequent emission of a photon of longer wavelength (or lower frequency). There are many fluorophores that stain biological cells yielding fluorescence images. For example, the Lysotracker probes from Invitrogen (Molecular Probes, Invitrogen Co.) are membrane permeable dyes which penetrate and stain cell vesicles. During vesicular release, the probe is secreted along with transmitter molecules and the secretion process may be monitored using fluorescence microscopy techniques.

With the advent of the green fluorescent protein (GFP) and its derivatives, cells can be tagged with fluorophores in an extremely specific manner, making fluorescence microscopy a fundamental biophysical tool. Tagging fluorescent proteins in a specific manner has allowed the investigation of the role that various proteins play during exocytosis [30].

Another interesting fluorophore is Fura-2, which is a ratiometric fluorescent dye widely used to measure Ca^{2+} concentrations [31]. Fura-2 selectively binds to Ca^{2+} ions with a dissociation constant of 100-200 nM. Fig. 2.1 shows the excitation spectrum of Fura-2 measured at 510 *nm* emission wavelength, for different free Ca^{2+} concentrations. Interestingly at 358 *nm* excitation wavelength (*isosbestic* point), the fluorescence does not depend on the free Ca^{2+} concentration. The ratio of the measured fluorescence intensities at a given excitation wavelength over that at the isosbestic point is proportional to the level of free Ca^{2+}. Fura-2 thus provides an excellent tool to monitor in real time the effect of phar-

macological treatment of cells on the level of free intracellular Ca^{2+}. To deliver Fura-2 in the intracellular environment one typically uses a patch-pipette in the whole cell configuration [32]. Alternatively one could use Fura-2AM, which is a membrane permeable derivative of Fura-2 that gets trapped inside the cells and binds to free intracellular Ca^{2+}.

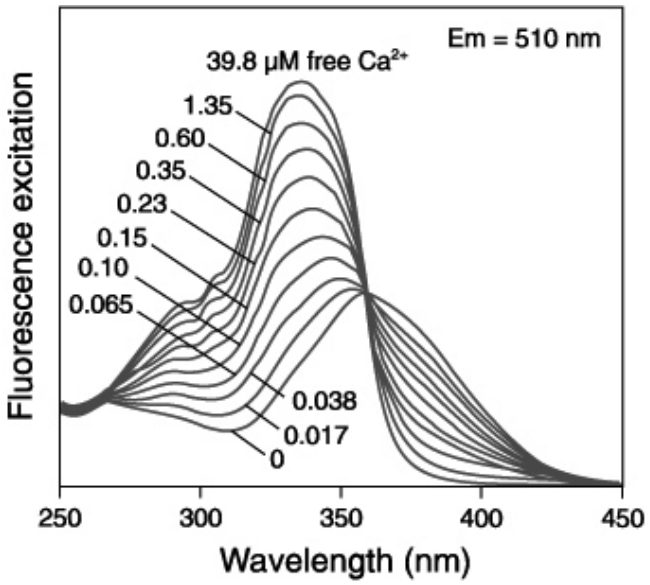

Figure 2.1: Excitation spectrum of the ratiometric dye Fura-2 used for measuring Ca^{2+} concentrations. Image from: http://www.invitrogen.com

In the present work Fura-2AM was utilized to visualize the effect of pharmacological treatments of chromaffin cells on the level of free intracellular Ca^{2+}, before and after ionophore stimulation. These experiments were done to confirm that the observed effects of pharmacological treatments were due to their specific inhibitory function and not because of side effects on Ca^{2+} channels, affecting Ca^{2+} concentration at rest or following stimulation.

2.2 Cell-attached capacitance measurements

The space occupied by a biological cell is defined by the cell membrane. Cell membranes are composed of lipid bilayers and membrane proteins, which are dielectric materials. The ions present in the intra- and extracellular spaces are separated by the cell membrane, forming the equivalent of an electrical capacitor. The specific capacitance of biological membranes is $\sim 0.8 - 1\ \mu F/cm^2$. The membrane capacitance C is given by the equation:

$$C = \frac{\epsilon \epsilon_0 A}{d} \tag{2.1}$$

where ϵ is the dielectric constant of the biological membrane, $\epsilon_0 = 8.85x10^{-12}$ F/m the permittivity of vacuum, A the cell membrane area, and d the membrane thickness. During exocytosis, a vesicle fuses with the cell plasma membrane. This fusion leads to an increase in the area of the cell plasma membrane, and thus an increase in the cell capacitance. Therefore individual fusion events can be detected as discrete capacitance steps [33]. For this purpose, standard patch-clamp techniques [32] are used to form a giga-seal in the cell-attached configuration [32, 21, 34] (Fig. 2.2).

To measure the cell-patch complex admittance, a reference electrode (chlorinated silver wire: Ag|AgCl) is immersed in the extracellular solution, while a second Ag|AgCl wire is inserted in the patch pipette, and a sine wave is applied to the wire [33, 35]. Using a dual lock-in amplifier the real and imaginary parts of the complex admittance are obtained.

For the cell-attached configuration, it can be shown that the complex admittance of the patch-cell is given by [19, 20]:

$$Y = \frac{G_P + R_A G_P^2 + \omega^2 C_P^2 R_A + i\omega C_P}{(1 + R_A G_P)^2 + (\omega C_P R_A)^2} \tag{2.2}$$

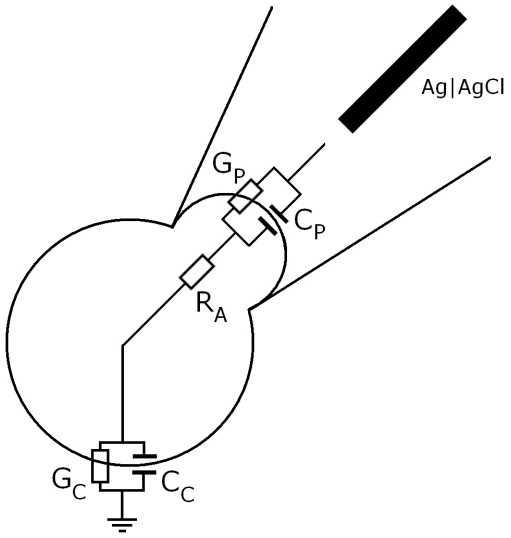

Figure 2.2: A schematic of a fire-polished glass pipette with a Ag|AgCl wire in it. A slight suction applied to the glass pipette seals the cell surface creating a patched membrane. The patched membrane area has a capacitance C_P and condunctance G_P. The equivalent circuit also contains the access resistance R_A, the total cell membrane capacitance C_C and the cell membrane conductance G_C.

where C_P and G_P are the capacitance and conductance of the patched area, R_A is the access resistance, ω the angular frequency of the applied sine wave, and i the imaginary unit. Equation (2.2) is derived with the assumption that the total cell membrane capacitance C_C can be ignored, since $C_C >> C_P$.

When a vesicle fuses with the cell plasma membrane a transient fusion pore forms (Fig. 2.3). It can be shown that in the cell-attached configuration and under proper phase compensation, the vesicle capacitance C_V and the fusion pore conductance G_V are given by [19, 20]:

$$C_V = \left[\left(Re^2 + Im^2\right)\right)/Im\Big]/\omega \tag{2.3}$$

$$G_V = \left(Re^2 + Im^2\right)/Re \tag{2.4}$$

where Re and Im are the real and imaginary parts of the complex admittance respectively. Therefore, measuring the real and imaginary parts of the admit-

tance provides information about the vesicle size (capacitance) and the fusion pore size (conductance).

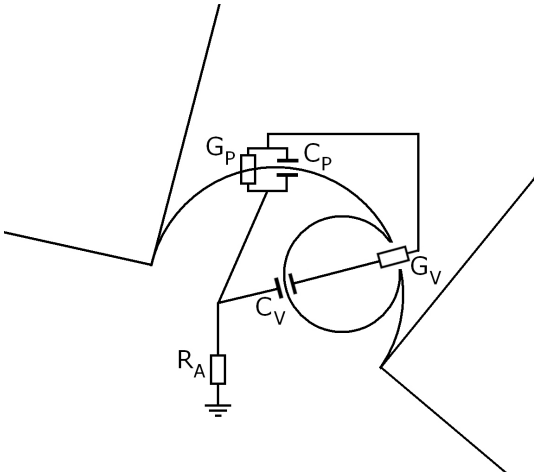

Figure 2.3: A schematic of the patched area depicting a single vesicle fusion event. C_P and G_P are the patched area capacitance and condunctance. C_V and G_V are the vesicle capacitance and the fusion pore conductance. R_A is the access resistance.

2.3 Electrochemistry

Upon fusion with the cell plasma membrane, chromaffin vesicles secrete their compounds into the extracellular space. The secreted compounds include the catecholamines norepinephrine and epinephrine, which are electroactive, and as such can be detected via electrochemical techniques. Most electrochemical techniques utilized in biological experiments require a working electrode, a reference electrode, and in some cases, a counter electrode. In the vast majority of biological electrochemical experiments, the working electrode is a carbon fiber electrode (CFE) [36]. When a CFE is immersed in physiological saline, electrical current can not flow across the electrode-electrolyte interface. In the CFE, current is carried by electrons, while in the solution current is carried by ions.

When a voltage is applied to the working electrode, excess charge accumulates at the electrode surface facing the solution. To achieve electroneutrality, this charge is compensated by counter ions spanning a finite distance in the solution, known as the Debye layer. When electroactive molecules diffuse to the electrode surface, electrons are transferred leading to a current flow [37]. The reference electrode is typically a Ag|AgCl, however it is not uncommon to use a saturated calomel electrode [38]. Probably the two electrochemical techniques most widely utilized by biophysicists are *amperometry* and *fast-scan cyclic voltammetry*.

2.3.1 Amperometry

The goal of amperometry is to reveal the time course of arrival of catecholamine molecules to the working electrode, typically a CFE. For this purpose, the CFE is held at a relatively high potential, usually +700 mV, such that upon contact with the CFE surface, the two hydroxyl groups of the catecholamine benzene ring (Fig. 2.4) are immediately oxidized. This oxidation leads to the donation of two electrons per catecholamine molecule to the detection apparatus and the conversion of the catecholamines to their ortho-quinone form (Fig. 2.5).

In a typical amperometric recording from a chromaffin cell, the CFE is in close proximity to the cell surface, in some cases even in contact (Fig. 2.6). Since chromaffin cell exocytosis depends on Ca^{2+} influx into the cell, a glass pipette containing a high concentration of K^+ ions is approached near the cell and a slight pressure is applied to the pipette. This changes the balance of K^+ ions between the intra- and extracellular spaces, leading to a net inward K^+ current,

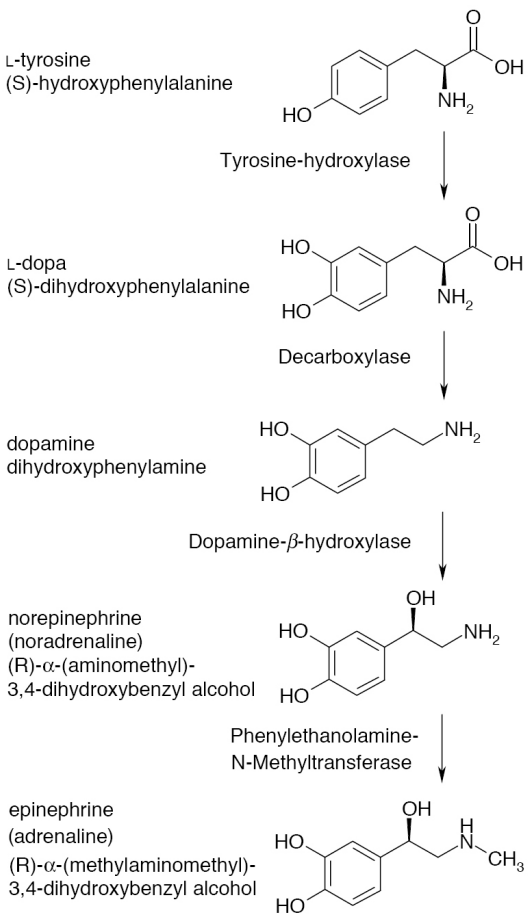

Figure 2.4: The biosynthetic pathway of catecholamines. Chromaffin cells convert dopamine to norepinephrine in a reaction catalyzed by dopamine-β-hydroxylase. Some chromaffin granules also contain the enzyme phenylethanolamine-N-Methyltransferase, which catalyzes the conversion of norepinephrine into epinephrine.

which in turn depolarizes the cell membrane and activates Ca^{2+} channels. Ca^{2+} entry into the cell stimulates exocytosis, and amperometric spikes are detected (Fig. 2.7).

The oxidation current depends on the time course of secretion of catecholamines from individual vesicles, as well as the time course of catecholamine diffusion towards the CFE surface. Upon close examination (Fig. 2.8), individual current spikes have significantly different time courses, indicating that both

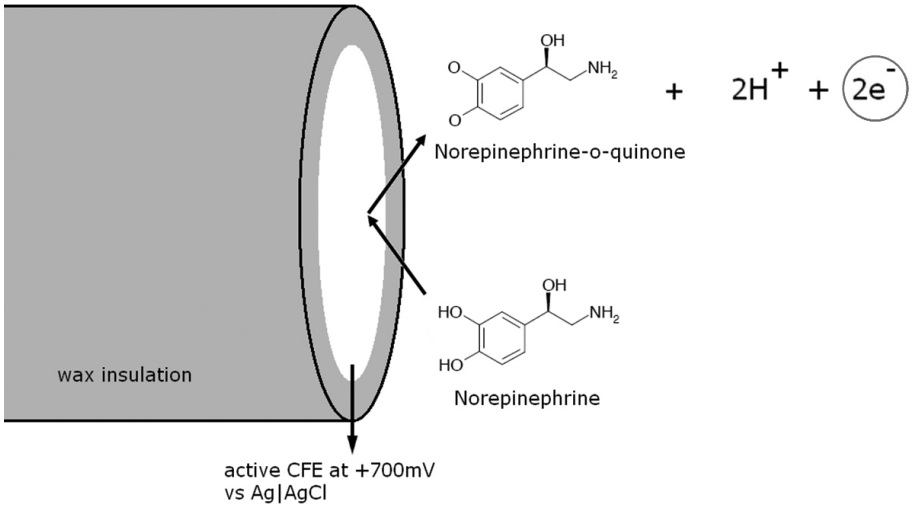

Figure 2.5: A CFE (gray: wax insulation, white: active electrode) in amperometric mode (electrode potential is held constant at +700 mV. Upon contact with the CFE surface, norepinephrine or epinephrine molecules are immediately oxidized to their ortho-quinone form. This oxidation generates two protons and two electrons (enclosed in the gray circle at the top right). The two electrons contribute to the amperometric current.

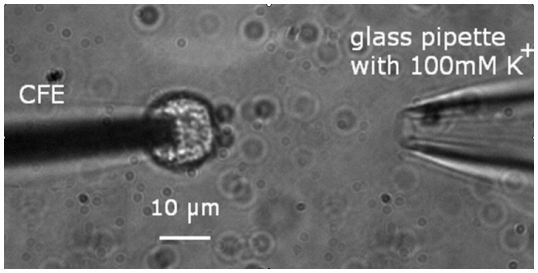

Figure 2.6: A CFE in contact with a bovine chromaffin cell. A glass pipette containing 100 mM KCl solution is approached to the right of the cell. When pressure is applied to the glass pipette, K^+ ions stimulate the cell and exocytotic activity is monitored via the CFE.

vesicular secretion and catecholamine diffusion may vary between individual exocytotic events.

A small 'foot' occurs at the initial phase of many amperometric spikes [25] (Fig. 2.9). This amperometric current, known as the "foot-signal" [25] indi-

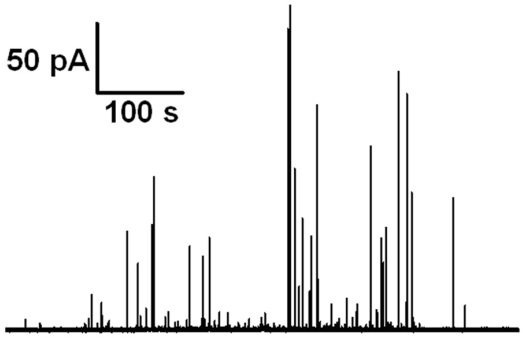

Figure 2.7: Amperometric spikes detected by a CFE in contact with a chromaffin cell.

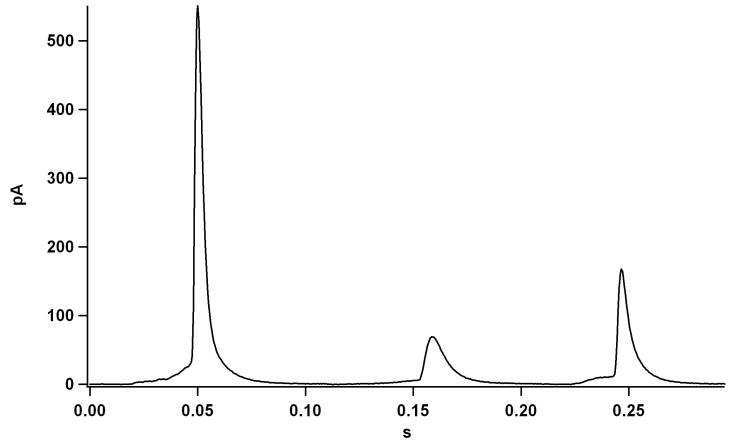

Figure 2.8: Three amperometric spikes shown on an expanded time scale. The spikes were measured by a CFE in contact with the surface of a bovine chromaffin cell.

cates the catecholamine flux during the initial fusion pore formed when a vesicle fuses with the cell plasma membrane [27].

Integration of the amperometric current spike (Fig. 2.9) reveals the measured charge, which is directly proportional to the amount of oxidized catecholamine molecules:

$$Q(t) = \int Idt = zeN \tag{2.5}$$

where z is the number of electrons transferred per reacted molecule (two for

catecholamines), $e = 1.6x10^{-19}\ C$ the elementary charge, and N the number of oxidized catecholamine molecules.

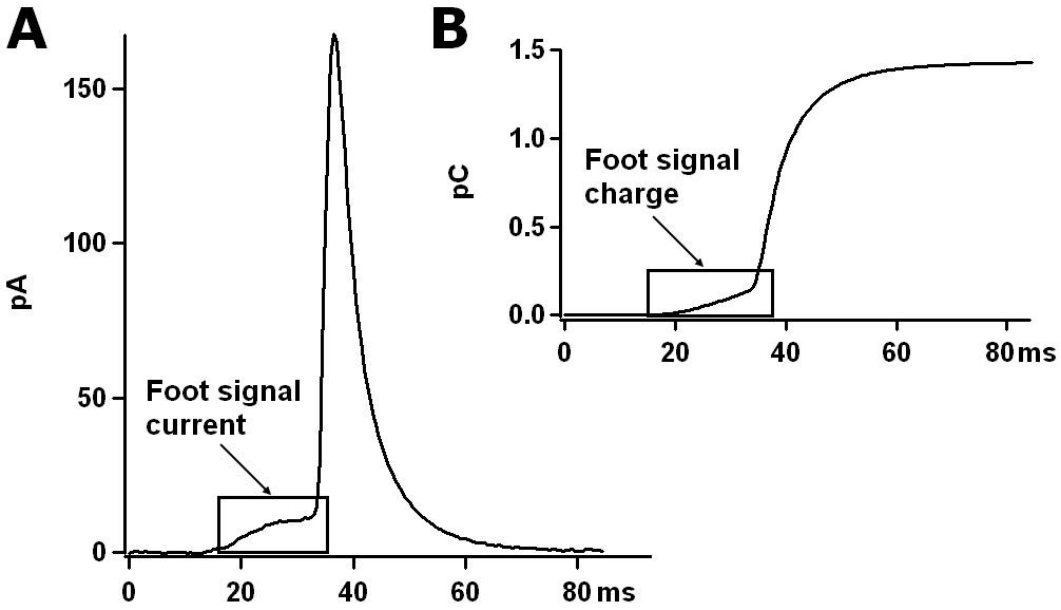

Figure 2.9: A single amperometric spike (A) and its integrated trace (B). The integrated trace reveals the charge measured by the electrode, and is directly proportional to the number of oxidized catecholamine molecules. The two rectangles indicate the foot signal current and charge.

2.3.2 Fast-scan cyclic voltammetry

Amperometry detects any electroactive compound but provides no information about the nature of the compounds. The goal of fast-scan cyclic voltammetry (FSCV) is to monitor the concentration of a specific analyte with subsecond temporal resolution. For this purpose, a periodic triangular waveform is applied to the CFE (Fig. 2.10).

During the anodic ramp (positive slope) of the triangular waveform, catecholamines in contact with the CFE surface are oxidized to their ortho-quinone

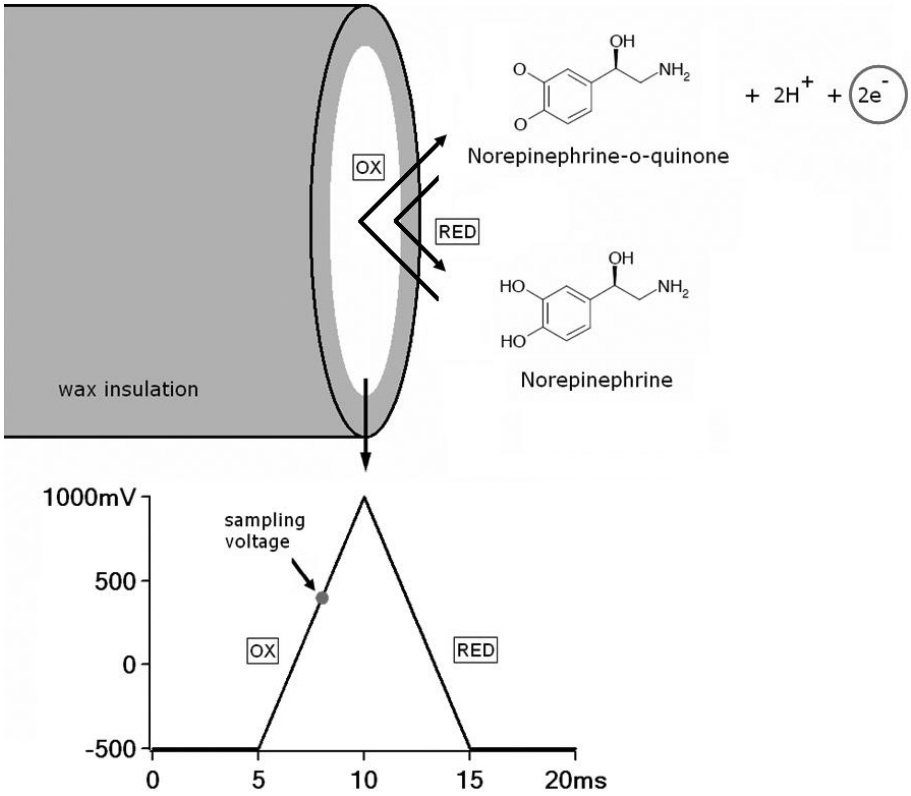

Figure 2.10: A CFE (gray: wax insulation, white: active electrode) in FSCV mode: a periodic triangular voltage waveform is repetitively applied to the electrode. During the anodic ramp of the triangular waveform, norepinephrine or epinephrine molecules are oxidized to their ortho-quinone form, while during the subsequent cathodic ramp the ortho-quinones are reduced back to the original catecholamines. The gray circle shows the two electrons that are detected during the anodic ramp. Two electrons are donated back during the cathodic ramp. The gray dot on the anodic ramp shows the potential at which the current is sampled to monitor voltammetric spikes (see text).

form, in a fashion similar to amperometry. However, during the subsequent cathodic ramp (negative slope), the ortho-quinones are reduced back to the original catecholamines (Fig. 2.10). Therefore the catecholamines are not consumed as in amperometry and the time course of voltammetrically measured spikes reveals the time course of diffusion of catecholamines away from the CFE surface.

As mentioned above, when an electrode is immersed in an electrolyte, a dif-

fuse double layer is created to compensate the electrode potential. This forms a capacitor, which is charged and discharged [38] during the applied voltage ramps, resulting in a large capacitive current, known as the *background* current (Fig. 2.11, dashed black trace). Therefore the redox current, also known as the *faradaic* current, is superimposed onto the background current (Fig. 2.11, solid red trace). To reveal the identity of the detected molecule, the background current must be subtracted from the total current, such that only the faradaic current remains (Fig. 2.11, blue trace). Plotting the faradaic current versus the applied potential produces the background-subtracted voltammogram (Fig. 2.12). The advantage of FSCV is that molecules can be distinguished based on the different background-subtracted voltammograms.

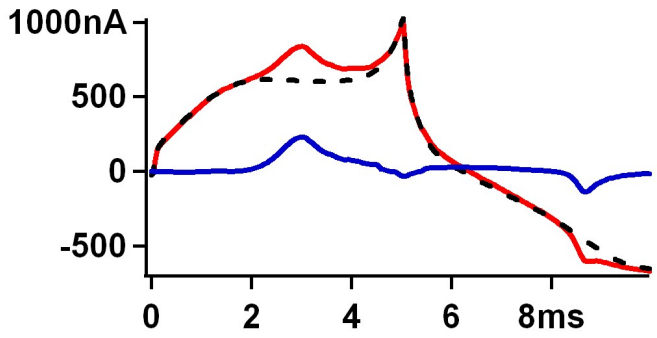

Figure 2.11: Background (dashed black trace) and background plus faradaic (solid red trace) currents plotted versus time. The difference between the two reveals the faradaic current (blue trace).

FSCV in single chromaffin cells revealed that some vesicles secrete norepinephrine, some others epinephrine, yet a few both of these catecholamines [39]. Fig. 2.13A shows a voltammetric recording from a single chromaffin cell, where multiple FSCV spikes are detected. Fig. 2.13B shows the background-subtracted voltammogram for the spike indicated by the arrow in Fig. 2.13A. The voltammogram reveals the chemical identity of catecholamine

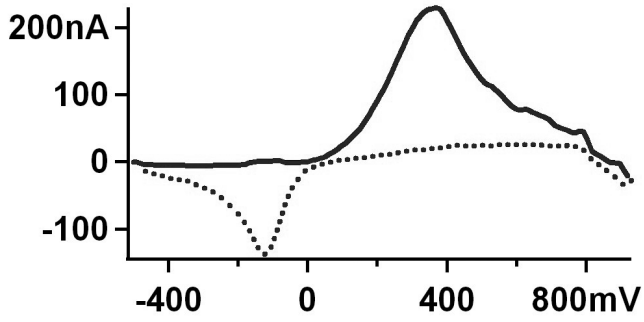

Figure 2.12: The faradaic current is plotted versus the applied potential and reveals the background-subtracted voltammogram for catecholamine molecules. During the anodic ramp catecholamines are oxidized to their quinone form (solid trace), while during the cathodic ramp the quinones are reduced back to the original catecholamine (dotted trace).

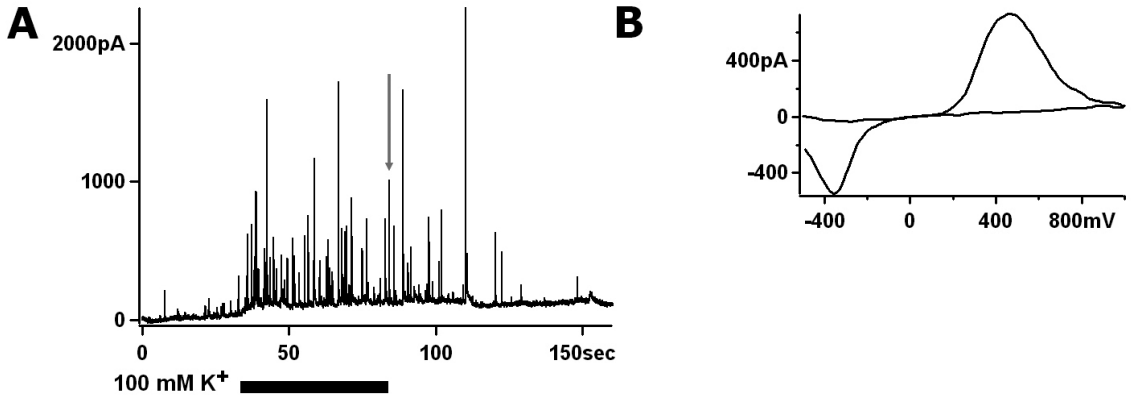

Figure 2.13: (A) Voltammetric spikes recorded from a bovine chromaffin cell using a CFE. The current was sampled at the +400 *mV* potential of the anodic ramp. The horizontal bar indicates the duration of the K^+ application. (B) The background-subtracted voltammogram for the spike indicated by the arrow in (A) reveals the identity of catecholamine molecules.

molecules. Fig. 2.14 shows, on an expanded time scale, a single FSCV spike with a foot signal of ~100 *ms* duration. The background-subtracted voltammograms during the foot and the spike peak are of different amplitude but similar shape, because they indicate the same secreted compound at different concentrations (inset of Fig. 2.14).

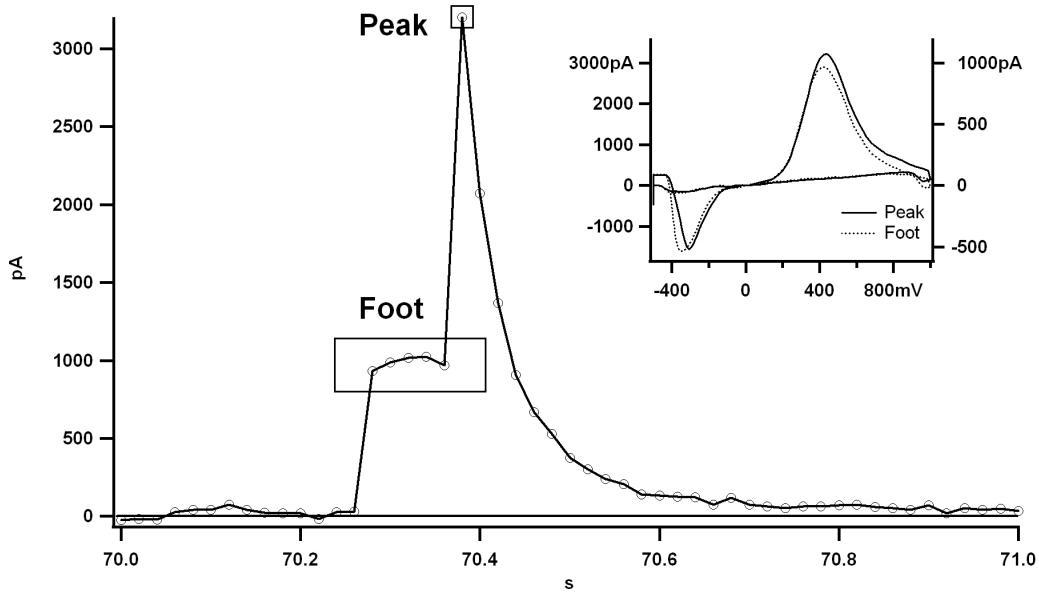

Figure 2.14: A single voltammetric spike is shown on an expanded time scale. The voltammetric current is sampled at the +400 mV potential of the anodic ramp. The background subtracted voltammograms (shown in the inset) for the peak and the foot are identical and correspond to catecholamine molecules.

2.4 Microfabrication techniques

Since the famous 1959 speech of Richard Feynman "There's Plenty of Room at the Bottom" [40] microtechnology has forever changed many scientific fields. Very recently, and with a delay of several decades from the invention of the transistor, innovative researchers started adopting microfabrication technologies for biological research.

Micro- and nanofabricated devices emerge as powerful tools to study cellular function on the nanoscale. An excellent example of utilizing microtechnologies to study cell function are the electrochemical detector (ECD) arrays [41]. ECD arrays of platinum microelectrodes have been fabricated to monitor chromaffin cell exocytosis with simultaneous amperometric recording and fluores-

cence imaging [42]. Amperometric recording with platinum electrodes are of similar quality as CFE recordings and the measured signals are consistent between the two types of electrodes [42]. This approach allowed correlation of amperometrically detected release with fluorescence signals with precision of a few hundred nanometers. In the present work we demonstrate advances in the ECD array fabrication process, which allow for improved spatiotemporal characterization of exocytosis and stimulus-secretion coupling.

2.5 Random walk simlations

Diffusion is the random motion of molecules in a medium. Passive transport of molecules from a region of higher to another of lower concentration occurs by diffusion. When no external forces are present, and the temperature in the system is uniform, diffusion will eventually equilibrate the concentration. Interestingly, diffusion is the mechanism with which neurotransmitters secreted from a presynaptic terminal transverse the synaptic cleft to reach receptors at the postsynaptic neuron. Diffusion is also the means with which catecholamines secreted from a vesicle reach the CFE surface. Thus the amperometric or voltammetric spike time course also contains information about the diffusion of catecholamines towards the CFE surface. The diffusive flux J is related to the concentration C of the diffusing species according to Fick's first law:

$$J = -D \bigtriangledown c = -D\left(\frac{\partial}{\partial x} + \frac{\partial}{\partial y} + \frac{\partial}{\partial z}\right)c \tag{2.6}$$

where D is the diffusion constant. Fick's second law relates the diffusion to the resulting change in concentration:

$$\frac{\partial}{\partial t}c = D \bigtriangledown^2 c = D\left(\frac{\partial^2}{\partial x^2} + \frac{\partial^2}{\partial y^2} + \frac{\partial^2}{\partial z^2}\right)c \tag{2.7}$$

For the case of a single CFE placed directly in front of a chromaffin cell, and assuming instantaneous catecholamine release from the vesicles, the measured amperometric current can be approximated by an analytical solution of the one dimensional diffusion equation [25]:

$$I = \sum_{i=-n}^{n+1} (-1)^i \frac{N(z - 2iz)}{2t\sqrt{\pi D t}} exp\left(\frac{-(z - 2iz)^2}{4Dt}\right) \tag{2.8}$$

where z is the cell-detector distance, N the number of detected molecules, D the diffusion constant, t the time, and the summation is extended from -7 to +8.

However, if complicated cell-electrode geometries are to be utilized, as in the case of ECD arrays (see above, section 2.4), Fick's second law can not be integrated to provide an analytical expression for the measured oxidation currents. Note that one can not numerically integrate Green's function over the ECD arrays, because this will not take into account the molecules reflected at the glass coverslip between the active electrodes. A different approach in this case is to model catecholamine diffusion as a random walk [43], such that the trajectory of each molecule consists of consecutive random jumps. Although computationally slow for large number of molecules, this method provides a solution to modeling diffusion in an arbitrary geometry.

CHAPTER 3

F-ACTIN AND MYOSIN II ACCELERATE CATECHOLAMINE RELEASE FROM CHROMAFFIN GRANULES

3.1 Abstract

The roles of nonmuscle myosin II and cortical actin filaments in chromaffin granule exocytosis were studied by confocal fluorescence microscopy, amperometry, and cell-attached capacitance measurements. Fluorescence imaging indicated decreased mobility of granules near the plasma membrane following inhibition of myosin II function with Blebbistatin. Slower fusion pore expansion rates and longer fusion pore lifetimes were observed after inhibition of actin polymerization using cytochalasin D. Amperometric recordings revealed increased amperometric spike half-widths without change in quantal size after either myosin II inhibition or actin disruption. These results suggest that actin and myosin II facilitate release from individual chromaffin granules by accelerating dissociation of catecholamines from the intragranular matrix possibly through generation of mechanical forces.

3.2 Introduction

Chromaffin cells of the adrenal gland are a widely used model system to study exocytosis [2]. The kinetics of catecholamine release from single chromaffin granules has been characterized in great detail using various approaches, such as amperometry [24], capacitance measurements [21] and patch-

amperometry [27]. The small foot signal preceding amperometric spikes [25] is an indication of catecholamine release through the fusion pore formed between the vesicular lumen and the extracellular space, upon fusion of the secretory vesicle with the cell plasma membrane [27].

Experimental evidence has been accumulated suggesting a role for the actin cytoskeleton in regulating neuroendocrine cell exocytosis [44]. According to the current view, a meshwork of filamentous actin (F-actin) underneath the plasma membrane acts as a physical barrier to exocytosis [45] that must be disassembled for vesicles from a reserve pool to enter the release-ready pool [46]. However, this model has been challenged by recent findings that suggest the participation of molecular motors, such as myosin Va, nonmuscle myosin II and other actin binding proteins [44] in dynamic interactions with actin, supporting a more specific role for actin in the process of exocytosis.

Biochemical studies have demonstrated association of myosin Va with chromaffin granules and reduction in secretion with anti-myosin V antibodies in permeabilized chromaffin cells has been reported [47]. More recently, it was shown that pharmacological inhibition of myosin II and overexpression of an unphosphorylatable mutant of the regulatory light chain (RLC) of myosin II slowed down chromaffin granule movement as well as catecholamine release from single chromaffin vesicles [48, 49].

However, the interaction between the actin cytoskeleton and the myosin molecular motors and how their interplay regulates secretion is unclear, specifically because myosin V but not myosin II has been found to interact with chromaffin granules [47]. If the modulation of release kinetics by myosin II is mediated by interactions with actin filaments, then inhibiting actin polymeriza-

tion would be expected to also affect individual secretory events. To investigate the roles of actin and myosin II in chromaffin granule exocytosis, in particular fusion pore properties, and catecholamine release from single vesicles, we performed fluorescence microscopy, amperometry and cell-attached capacitance recordings on single chromaffin cells following inhibition of either actin polymerization or the ATPase activity of myosin II.

3.3 Materials and Methods

3.3.1 Cell preparation, reagents and solutions

Bovine chromaffin cells were prepared as previously described [50]. The buffered solution used for all the amperometric, capacitance and fluorescence measurements contained (in mM) 140 NaCl, 5 KCl, 5 $CaCl_2$, 1 $MgCl_2$, 10 HEPES/NaOH, 20 glucose (pH 7.3). The pipette solution used for the capacitance recordings contained (in mM) 50 NaCl, 100 TEA-Cl, 5 KCl, 5 $CaCl_2$, 1 $MgCl_2$, 10 HEPES/NaOH (pH 7.3). Ionomycin was purchased from Sigma and stock solution was prepared in ethanol. (-)-blebbistatin, cytochalasin D, 1-(5-Iodonaphthalene-1-sulfonyl)-1H-hexahydro-1,4-diazepine hydrochloride (ML-7), and latrunculin A were all purchased from Sigma and stock solutions were prepared in dimethylsulfoxide. Immediately prior to the beginning of an experimental session, stock solutions were diluted in the bath solution at a final concentration of 10 μM for Ionomycin, 4 μM for cytochalasin D, 10 μM for blebbistatin, 3 μM for ML-7, and 2 μM for latrunculin A. Chromaffin cells were incubated with the different inhibitors for 15 min at 37^oC and 10% CO_2 immediately

prior to the recordings. A similar incubation was performed for control cells in order to take into account possible temperature effects on exocytotic activity [51].

3.3.2 Fura-2 calcium imaging

Coverslips containing the chromaffin cells were placed in a Petri dish containing 3 μM cell permeant Fura-2AM (Molecular Probes, Invitrogen Co.) for 15 *min*. The cells were then gently washed twice with buffer solution such that the dye was removed and either buffer solution (control), 10 μM blebbistatin, or 4 μM cytochalasin D was added onto the cells. The dishes were mounted on a custom built stage for an inverted microscope (Zeiss Axiovert 135 TV) equipped with a Zeiss FT425 dichroic filter and a Schott GG495 emission filter, and protected from light for a period of 10 *min* prior to imaging. The fluorescence intensity was recorded using 100 *ms* exposures at a rate of 0.2 *Hz* for a total period of 150 *s* using a charge-coupled device (iXon EMCCD, Andor Technology). At each time point a pair of images was acquired, using a filter wheel (Lambda 10-2, Sutter Instruments) to switch between 358 *nm* and 390 *nm* excitation wavelengths. Images were stored as 16-bit integer matrices and were analyzed using custom written procedures in Igor Pro. The background fluorescence intensity was determined for each image at each wavelength in the sequence of images by taking the average plus three standard deviations of the intensity measured from a ~20 μm^2 square region in each image in an area which did not contain any cells or floating particles. For each image the background was subtracted from the average fluorescence intensity from a ~20 μm^2 square region within each cell. The ratio of the Ca^{2+} sensitive (390 *nm*) over the Ca^{2+} insensitive (358

nm) channel was then obtained. The response from all the cells within a treatment group was averaged at each time point. The data is presented as MEAN ± SEM, where n=12 cells for control, 24 cells for blebbistatin, and 15 cells for cytochalasin D-treated cells. Student's unpaired T-test was used to obtain the statistical significance of the measured data.

3.3.3 Quantification of cortical actin

Chromaffin cells treated with the different inhibitors were fixed with 3.7% formaldehyde for 10 *min* after 30 *min* incubation with the inhibitor at 37^oC. Cells were then permeabilized with 0.1% Triton X-100 for 5 *min* and actin filaments labeled with Alexa 568 phalloidin. Confocal microscopy was performed with a Leica TCS SP2 system with an acoustic optic-tunable filter and a 63x 0.9 NA water immersion objective. The density of cortical actin was quantified at the equatorial plane by integrating the total fluorescence intensity in an annular region containing the cell plasma membrane and dividing by the annulus area. The annular width was kept constant to 1.5 μm.

3.3.4 Vesicle tracking

Chromaffin granules were labeled with 3 μM LysoTracker Green (Molecular Probes, Invitrogen Co.) for 5 *min* before imaging. Confocal microscopy was performed using the system described above with an optical slice thickness of $\sim$ 0.9 μm at the interface between the glass surface and the cell plasma membrane. Images were acquired at a frame rate of 1.67 s^{-1} and the coordinates of

individual vesicles were obtained by using the public domain program ImageJ. The vesicle tracking plug-in used was an implementation of an algorithm previously described [52]. Vesicles were automatically detected by the program after setting criteria for vesicle image size (circular spot of $\leq$ 500 *nm* diameter) and cut-off intensity (50% of the brightest particles detected). Vesicles were followed for several frames as long as they remained detected as a particle by the program. All tracks were overlaid with the original time series and visually inspected for accuracy. Only tracks longer than 10 frames were used for the analysis. After setting the selection criteria for vesicle size, cut-off intensity and trajectory length, 9-17 vesicles per cell were left for analysis from which the 9-10 brightest were chosen per cell to ensure that the tracking occurred for a similar number of vesicles per cell for all treatment groups. Mean squared displacements (MSD) were calculated as described [53] using a custom MATLAB (MathWorks) routine using the equation:

$$MSD(n\delta t) = \frac{1}{N-n}\sum_{j=1}^{N-n}\Big((x(j\delta t + n\delta t) - x(j\delta t))^2 + (y(j\delta t + n\delta t) - y(j\delta t))^2\Big) \qquad (3.1)$$

where n and j are positive integers with $n = 1, 2, ...(N-1)$. $(x(j\delta t), y(j\delta t))$ and $(x(j\delta t + n\delta t), y(j\delta t + n\delta t))$ are the granule's coordinates at time $j\delta t$ and $j\delta t + n\delta t$ respectively [54]. Data was fitted to a simple diffusion model: $MSD(n\delta t) = 4Dn\delta t + c$, where D is the diffusion coefficient and c is a constant that accounts for the limited accuracy of the experimental setup [54]. All experiments were carried out in 35 *mm* Petri dishes with coverglass bottoms (0.16 – 0.19 *mm*, MatTek, Ashland, MA).

3.3.5 Amperometry

Amperometry was performed using custom made CFEs and a patch-clamp amplifier (EPC-8, HEKA-Elektronik, Germany). The current was low pass filtered at 500 Hz using the built-in analog low pass filter of the EPC-8 amplifier. The CFE was in touch with the cell surface, as verified visually by a slight deformation of the cell membrane. The CFE voltage was held at +700 mV versus a Ag|AgCl reference electrode. A glass pipette with ~2.5 μm tip diameter containing 10 μM ionomycin solution was positioned ~40 μm away from the cell and a 3 s 3.5 x 10^4 Pa puff was applied to the pipette using a pressure application system (PicoSpritzer II, Parker-Hannifin/General Valve, Fairfield, NJ) to stimulate exocytosis. Amperometric recordings were performed for 10 min after stimulation and the data was digitized at 2 kHz rate by a 16-bit resolution NIDAQ board (BNC-2090, National Instruments, Austin, TX). A digital notch filter at 60 Hz (Igor Pro, WaveMetrics, Lake Oswego, OR) was used to remove line frequency noise. Recordings were analyzed as previously described (Mosharov and Sulzer, 2005). Spikes with amplitude less than 10 pA, or half-width more than 300 ms, and overlapping spikes were excluded from the analysis. The 10 pA threshold was high enough for amperometric signals to be discerned from noise and low enough for the majority of amperometric spikes in all treatment groups to be included in the data analysis. The thresholds used for identifying foot signals were 1 pA amplitude and 5 ms duration.

3.3.6 Cell-attached capacitance measurements

High resolution capacitance measurements were performed in the cell-attached configuration as previously described [21] using a HEKA EPC-7 amplifier and patch pipettes of nominal resistance between 1 and 2 $M\Omega$. A dual lock-in amplifier (SR 830, Stanford Research Instruments, Sunnyvale, CA) was used to obtain the complex admittance using a 50 mV-rms amplitude and 20 kHz frequency sine wave applied to the patch pipette. The lock-in amplifier outputs were digitized at 1 kHz rate by two 16-bit resolution channels of the NIDAQ board. Custom written software [34] in Igor Pro converted the two orthogonal traces (real and imaginary parts) into measurements of vesicle capacitance C_V (units of fF) and fusion pore conductance G_V (units of nS) as described [21]. From these recordings, vesicle size C_V, fusion pore lifetime, fusion pore conductance, and fusion pore expansion rate were derived as described [34]. For this analysis, only exocytotic events with lifetime ≥15 ms were used [34], since shorter events were heavily affected by the lock-in low-pass filters (τ=1 ms, 24 dB, which corresponds to 10 - 90% risetime of 5 ms) and their conductance properties are not reliably determined. The fusion pore initial expansion rate was calculated as the slope of a linear fit to the initial 15 ms segment of the conductance trace. The fusion pore lifetime was the time from fusion pore opening until the fusion pore conductance value exceeded 2 nS [34].

3.3.7 Statistical analysis

All reported signal parameters, amperometric (quantal size, half-width, spike amplitude, mean foot signal amplitude and foot duration) and patch-

capacitance (vesicle size, fusion pore initial and average conductance, fusion pore initial expansion rate and fusion pore lifetime), were statistically analyzed by taking the median values of the events from individual cells and subsequently averaging these values per treatment group. Therefore, data is represented as MEAN ± SEM, where n is the number of cells in each treatment group. Differences were considered to be statistically significant for $p < 0.05$ as assessed by Student's unpaired T-test for both the amperometric and patch-capacitance data. All experiments were performed at room temperature at day 1 after cell isolation. The data came from two and four different cell preparations for amperometry and capacitance respectively.

3.4 Results

To investigate the roles of actin and nonmuscle myosin II in exocytosis of chromaffin granules we used cytochalasin D and latrunculin A, which inhibit actin polymerization, blebbistatin, a specific inhibitor of nonmuscle myosin II [55], and ML-7, an inhibitor of myosin light chain kinase (MLCK).

3.4.1 Calcium levels are not affected by blebbistatin or cytochalasin D treatment

In order to evaluate the specificity of these pharmacological manipulations it was first confirmed that the drug treatments did not affect intracellular Ca^{2+} levels at rest or Ca^{2+} influx following stimulation by ionomycin. For this purpose, chromaffin cells were labeled with the ratiometric dye Fura-2 and imaged

using fluorescence microscopy. The ratio of the fluorescence intensity at 390 *nm* over 358 *nm* excitation wavelength was measured before addition of ionomycin and found to be similar between control and blebbistatin ($p > 0.64$) and between control and cytochalasin D ($p > 0.65$) treated cells (Fig. 3.1A). This indicates that the pharmacological manipulations used in our study had no effect on the levels of intracellular Ca^{2+} at rest.

Another possible indirect effect of the pharmacological agents would be to influence Ca^{2+} influx following stimulation by ionomycin. To test this, a glass pipette with ~5.0 μm tip diameter containing 10 μM ionomycin solution was positioned ~20 μm away from the cells and a 30 s 1.0 x 10^4 Pa puff was applied to the pipette using a pressure application system (PicoSpritzer II, Parker-Hannifin/General Valve, Fairfield, NJ) to promote Ca^{2+} entry into the cells. The Ca^{2+} dynamics were monitored as fluorescence intensity ratios obtained every 5 s for a total of 150 s (30 images). The response of all the cells per treatment group was averaged at each time point to obtain the average time course of intracellular Ca^{2+} levels for each treatment group. No significant difference was observed between control, blebbistatin and cytochalasin D-treated cells (Fig. 3.1B). The minimum of the averaged ratios, which occurs when the intracellular Ca^{2+} amount is maximum, was similar for all treatment groups (control and blebbistatin: $p = 0.46$, control and cytochalasin D: $p = 0.80$). These results thus clearly indicate that there is no difference between treatment groups in the intracellular Ca^{2+} levels at rest (Fig. 3.1A) or in the amount of Ca^{2+} influx following ionomycin stimulation of chromaffin cells (Fig. 3.1B). Furthermore, the results indicate that following ionomycin stimulation of chromaffin cells, intracellular Ca^{2+} levels remain relatively high and do not return to the pre-stimulus baseline (Fig. 3.1B).

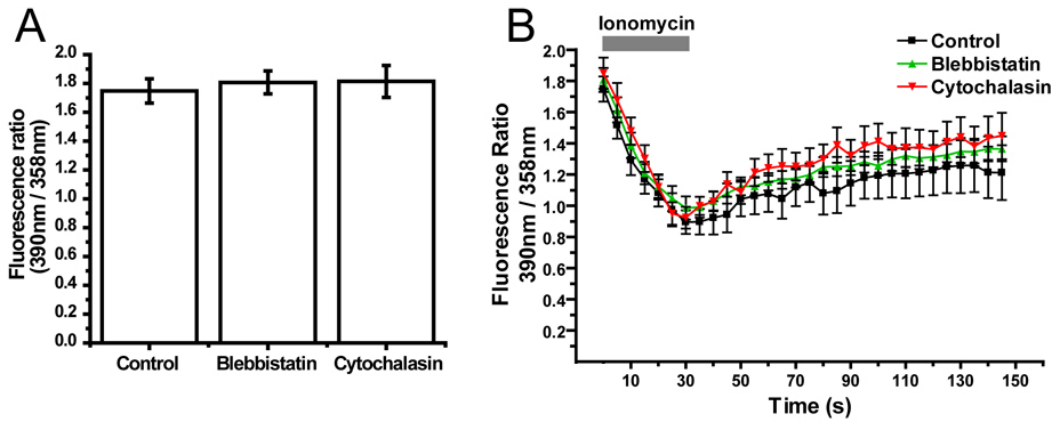

Figure 3.1: Effects of cytochalasin D and blebbistatin on chromaffin cell calcium levels. Ratio of fluorescence intensity excited at 390 *nm* over 358 *nm*. Response from cells at rest (A) and following addition of ionomycin (B). Data is mean ± SEM, n=12 cells for control, 24 cells for blebbistatin and 15 cells for cytochalasin D.

3.4.2 Blebbistatin treatment decreases vesicular motion

Myosin II and the actin cytoskeleton have been implicated in vesicular motion [48]. We characterized vesicular movement in unstimulated cells using confocal microscopy focused on the actin rich cortical region of the cell (Fig. 3.2A).

For this purpose, we tracked the motion of 94 vesicles from 9 untreated cells and 92 vesicles from 10 cells treated with blebbistatin. The x and y coordinates of each vesicle were tracked in a series of images (Fig. 3.2B) and converted into MSD for that particular vesicle. These were then averaged for all the cells per treatment group and plotted versus time (Fig. 3.2C). A linear fit to the data (Fig. 3.2C), revealed the apparent diffusion coefficient for the vesicles in each treatment group. The resulting apparent diffusion coefficients were 2.07 ± 0.06 $x10^{-3}$ $\mu m^2/s$ for control cells and 6.8 ± 0.8 $x10^{-4}$ $\mu m^2/s$ for blebbistatin-treated cells, thus ~3 fold lower in cells where the ATPase activity of myosin II was

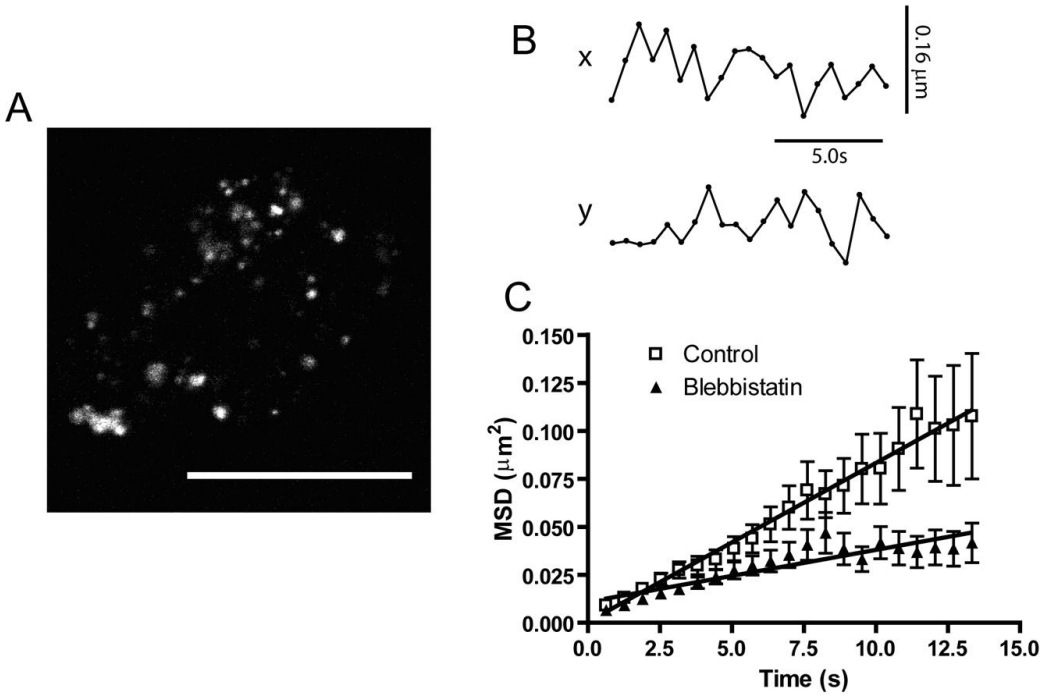

Figure 3.2: (A) Confocal micrograph of a representative cell used for vesicle tracking. Vesicles were labeled with Lysotracker green for 5 *min* and then imaged at 25^oC without stimulation. Scale bar represents 20 μm. (B) Trace of typical xy coordinates followed by a single vesicle taken from control cells. (C) Plots of two dimensional MSD calculated for control and blebbistatin-treated cells. Data is presented as mean ± SEM for 94 vesicles from 9 control cells, and 92 vesicles from 10 blebbistatin-treated cells.

specifically inhibited compared to control cells.

3.4.3 Cytochalasin D but not blebbistatin affects cortical actin distribution

To test if the decreased mobility following inhibition of myosin II is a consequence of cortical actin destabilization, fluorescence microscopy was used

to determine how cytochalasin D and blebbistatin treatment affected the distribution of cortical actin fluorescence. As expected, cytochalasin D-treated cells, showed disruption of cortical actin in contrast to blebbistatin-treated cells, which showed a similar distribution as control cells (Fig. 3.3A). Quantitative analysis (Fig. 3.3B) showed a 44% decrease in cortical actin fluorescence intensity ($p < 0.001$) in cytochalasin D-treated cells, while blebbistatin-treated cells showed no significant difference ($p > 0.35$) when compared to control cells (Fig. 3.3C). These results indicate that the observed changes in vesicle mobility as well as the observed changes in release event properties (see below) are a direct consequence of myosin II inhibition in the absence of cortical actin disintegration.

3.4.4 Inhibition of myosin II slows individual release events

The kinetics of catecholamine release from single vesicles was determined by carbon fiber amperometry. Fig. 3.4A shows a typical recording from a chromaffin cell under control conditions. To characterize the average release kinetics an average amperometric spike shape was constructed (Fig. 3.4B). All amperometric signals detected from a single cell with amplitude >10 pA and half-width <300 ms were normalized to their peak amplitude, aligned in time at the point of their maximum slope (occurring shortly before the spike maximum) and averaged, providing the average spike shape for this cell. Subsequently, the average spikes from each cell in a treatment group were again averaged in the same way to obtain the average spike shapes for the different groups. Last, the averaged spikes for the three groups were normalized such that they all had the same quantal size, consistent with the statistical analysis of integrated amperometric

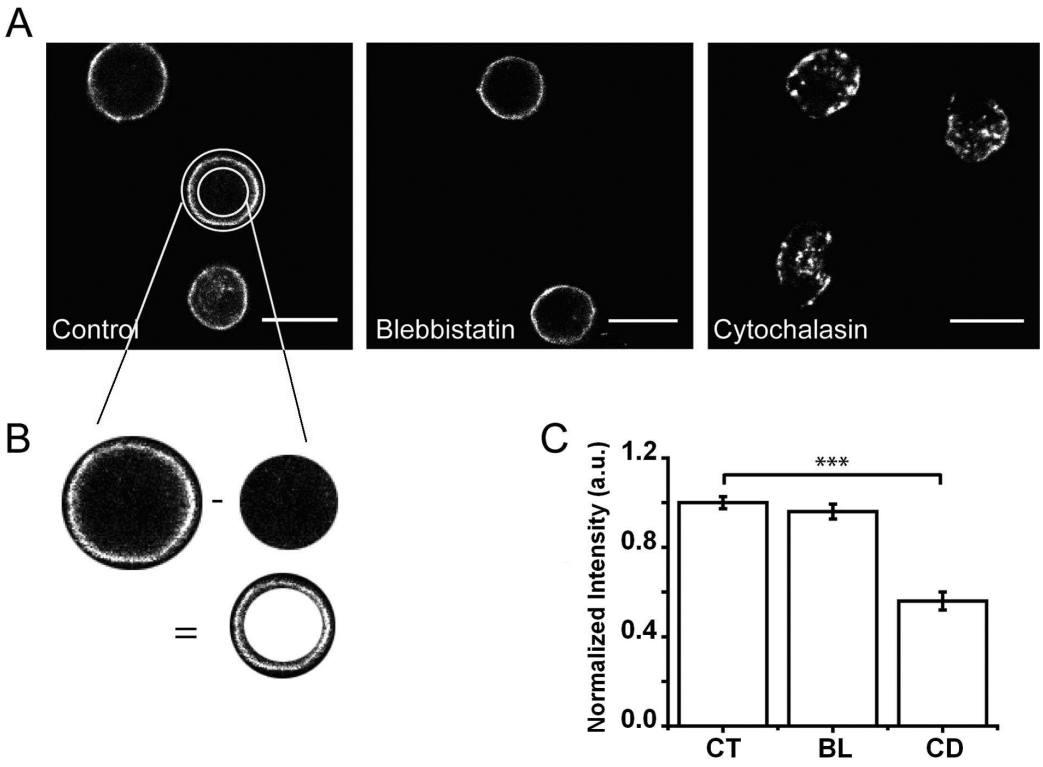

Figure 3.3: Effects of inhibition of actin polymerization and myosin II function on cortical actin distribution. (A) Confocal micrographs of chromaffin cells in control condition, and treated with 10 μM blebbistatin or 4 μM cytochalasin D. Cells were fixed after 30 *min* incubation with the inhibitor and stained for F-actin with Alexa 568 phalloidin. Scale bar represents 20 μm. (B) Schematic depicts the quantification of cortical actin. A circular region of interest inside the cell was subtracted from another region covering the entire cell. The annular width was kept equal to 1.5 μm for all cells. (C) Quantified fluorescence of Alexa 568-palloiding labeled F-actin on the cortical region. Fluorescence values were normalized to the mean value for control cells. Data is presented as MEAN ± SEM from a total of 20 cells per group, triple asterisks represent $p < 0.001$ from Student's unpaired t-Test.

charge (see below). Both, blebbistatin and cytochalasin D-treated cells showed reduced spike amplitude with increased half-width.

To determine the statistical significance of the changes in amperometric spike properties, five parameters were determined for each spike: quantal size, amperometric spike half-width, peak amplitude, mean foot current amplitude

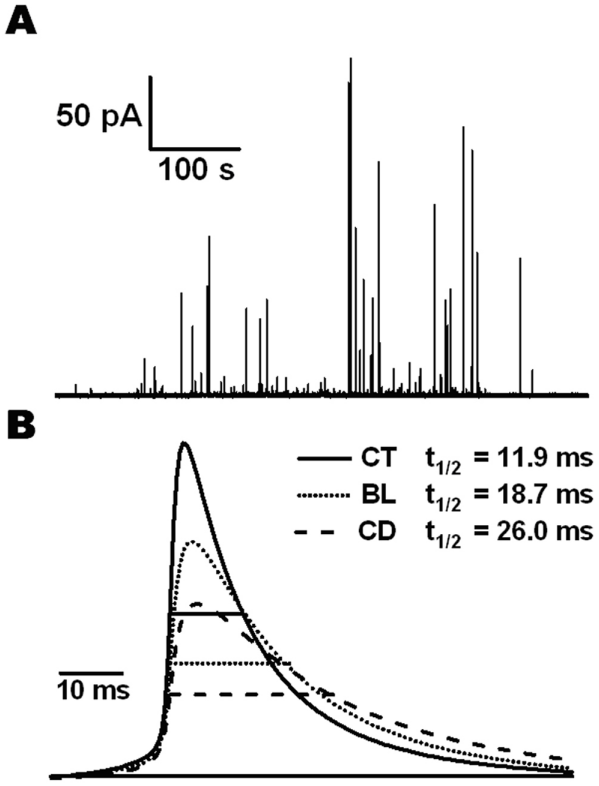

Figure 3.4: (A) A typical recording from an untreated chromaffin cell stimulated with ionomycin. (B) Spikes from each cell were normalized to their peak amplitude, aligned in time at the point of their maximum slope (occurring shortly before the spike maximum) and averaged, providing the average spike shape for this cell. The average spikes from each cell in a treatment group were again averaged in the same way to obtain the average spike shapes for control (CT, n = 19 cells, 786 spikes), blebbistatin-treated (BL, n = 18 cells, 633 spikes) and cytochalasin D-treated (CD, n = 18 cells, 1229 spikes) cells. Last, the averaged spikes were normalized to the same quantal size. The half-widths of these averaged spikes were 11.9 *ms* for control, 18.7 *ms* for blebbistatin-treated, and 26.0 *ms* for cytochalasin D-treated cells.

and foot signal duration (Fig. 3.5A) [56]. When the average spike half-width was determined for each cell and the mean for all cells in a treatment group was calculated, values of 12.7 ± 1.0 *ms* (control), 18.6 ± 1.2 *ms* (blebbistatin), and 24.7 ± 2.2 *ms* (cytochalasin D) were obtained, in excellent agreement with the values from the averaged spikes (Fig. 3.4B).

A more robust method avoiding spurious artifacts due to outliers is to determine the median value for each spike parameter for each cell and subsequently calculate the mean of these median values for each treatment group (Fig. 3.5B-G) [56]. The half-widths determined with this method after normalizing to the control values were 100 ± 7.9 % (control, n = 19 cells), 153.5 ± 8.9 % (blebbistatin, n = 18 cells), and 224.8 ± 22.8 % (cytochalasin D, n = 18 cells), confirming that the observed increase in spike half-width due to inhibition of myosin II function or due to inhibition of actin polymerization are highly significant (Fig. 3.5B). Consistent with these results, the inhibition of MLCK with the inhibitor ML-7 also increased the amperometric half-widths to a similar value as blebbistatin (145.3 ± 12.2 %, $p < 0.01$, Fig. 3.5B). The increases in amperometric spike half-width by these treatments were accompanied by decreases in amperometric spike amplitude (Fig. 3.5C) with no significant changes in quantal size (Fig. 3.5D).

To test whether the effects of cytochalasin D were specifically due to inhibition of actin polymerization, amperometric recordings were also performed in cells treated with latrunculin A, which also hinders actin polymerization. Latrunculin A treatment produced an increase of amperometric spike half-width and decrease of spike peak amplitude without affecting quantal size (Fig. 3.5B-D), indistinguishable from the effects of cytochalasin D, indicating that these changes are specific consequences of actin depolymerization.

The number of exocytotic events recorded within 10 *min* after stimulation was unchanged when myosin II was inhibited (Fig. 3.5E). In contrast, in cells treated with ML-7 the number of events was significantly reduced to 33% of control (Fig. 3.5E, $p < 0.01$). This suggests that inhibition of MLCK by ML-7

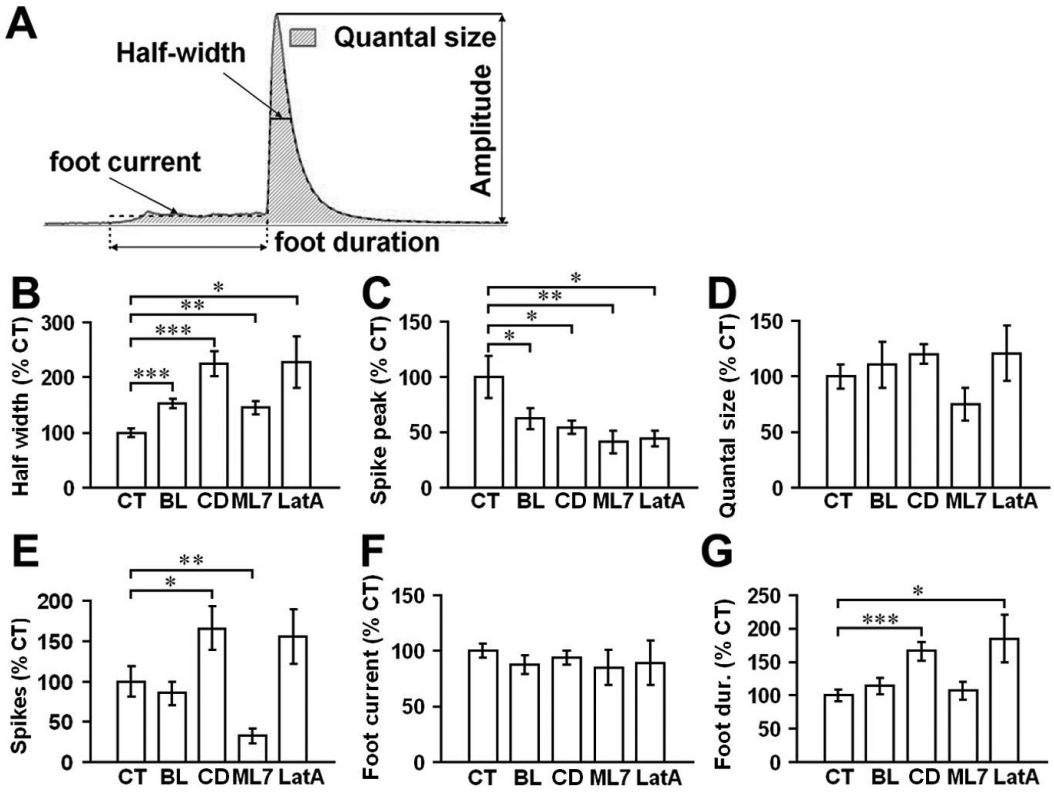

Figure 3.5: (A) A single amperometric spike along with the five parameters: quantal size Q (pC), half-width (ms), peak amplitude (pA), foot signal duration (ms), and mean foot current (pA). Averaged values for half-width (B), peak amplitude (C), quantal size (D), number of exocytotic events (E), mean foot current (F), and foot signal duration (G) for control (CT, n = 19 cells, 786 spikes), blebbistatin (BL, n = 18 cells, 633 spikes), cytochalasin D (CD, n = 18 cells, 1229 spikes), ML-7 (ML7, n = 20 cells, 388 spikes), and latrunculin A (LatA, n = 10 cells) expressed as percentage of control values (always taken to be 100%). Data is represented as MEAN ± SEM, where n is the number of cells. Differences between treatment groups were tested for statistical significance by Student's unpaired t-Test and are indicated by single ($p < 0.05$), double ($p < 0.01$) or triple ($p < 0.001$) asterisks.

may affect other non myosin II molecules, consistent with recent evidence [57], leading to the observed reduction in exocytotic events. However, in contrast to blebbistatin and ML-7, cytochalasin D or latrunculin A treatment increased the number of spikes by ~66% compared to control cells (Fig. 3.5E), in good agreement with the proposed role of actin as a barrier to exocytosis [45, 47].

3.4.5 Inhibition of actin polymerization but not myosin II affects the early fusion pore

The foot signal preceding single amperometric spikes [25] has attracted significant attention as it is directly related to the early fusion pore formed during chromaffin granule exocytosis [27, 34, 58]. Neither inhibition of myosin II by blebbistatin or ML-7 nor inhibition of actin polymerization by cytochalasin D or latrunculin A had an effect on the mean foot current amplitude (Fig. 3.5F), suggesting that neither myosin II nor actin affect the structure of the early fusion pore. In contrast, the average foot signal duration was significantly increased (Fig. 3.5G) by ~65% in cytochalasin D ($p < 0.0001$) and latrunculin A ($p < 0.05$) treated cells, but was unchanged by inhibition of myosin II with blebbistatin or ML-7 (Fig. 3.5G). Foot signal duration could be reliably determined only for foot signals with duration ≥ 5 *ms* and amplitude ≥ 1 *pA*. The percentage of amperometric spikes that had a foot signal in this range was similar for control and blebbistatin-treated cells (33% and 35% respectively), but was increased to 45% for cytochalasin D-treated cells, consistent with the overall increase in foot duration.

3.4.6 Alteration of fusion pore properties by cytochalasin D

Time-resolved cell-attached patch clamp capacitance measurements provide a direct assessment of individual fusion pore properties. The data analysis (Fig. 3.6A) reveals the capacitance C_V of the fused vesicle, the initial and average fusion pore conductance, the fusion pore lifetime and the fusion pore expansion rate [19, 21].

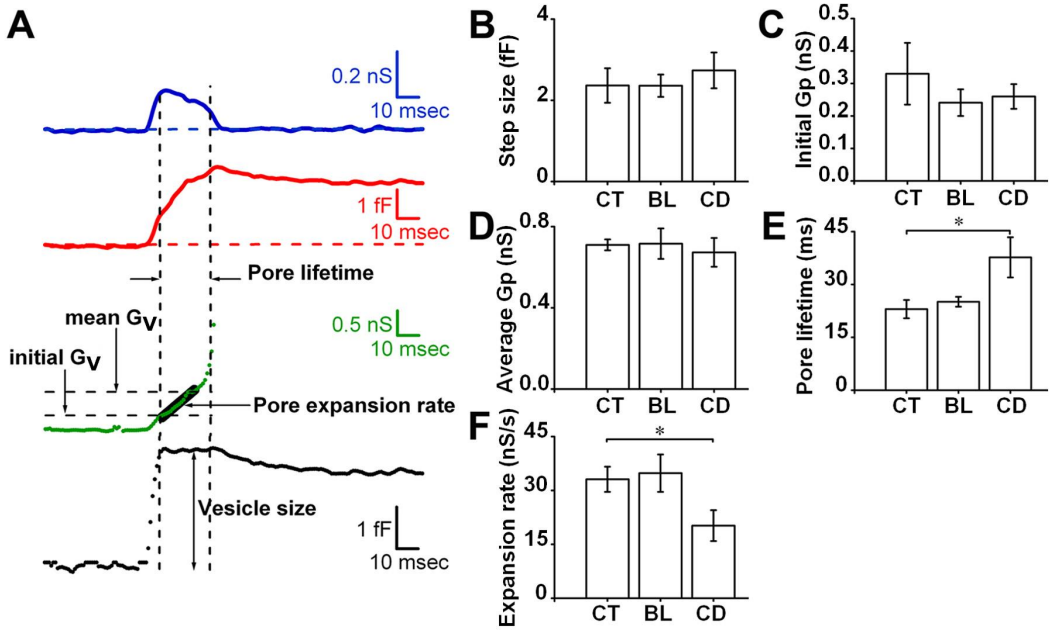

Figure 3.6: (A) The real (blue trace) and imaginary (red trace) parts of the complex admittance are converted into fusion pore conductance G_V (green dots) and vesicle capacitance C_V (black dots). The fusion pore initial and average conductance are depicted by the dashed horizontal black lines, while the fusion pore expansion rate is the slope of the linear fit to the initial 15 ms segment of the conductance trace (solid black line). The fusion pore lifetime is the time for the conductance to reach 2 nS from its initial value. (B) Vesicle step size, (C) fusion pore initial conductance, (D) fusion pore average conductance, (E) fusion pore lifetime and (F) fusion pore initial expansion rate for control (CT, n = 7 cells, 86 fusion pores), blebbistatin (BL, n = 8 cells, 82 fusion pores), and cytochalasin D-treated (CD, n = 8 cells, 78 fusion pores) cells. Data is represented as MEAN ± SEM, where n is the number of cells. Statistically significant differences ($p < 0.05$) are indicated by single asterisks.

Vesicle capacitance (Fig. 3.6B), as well as initial and average fusion pore conductance (Fig. 3.6C & D) were unchanged in cells treated with blebbistatin or cytochalasin D. Thus, inhibiting myosin II function or actin polymerization has no effect on vesicle size, vesicular catecholamine concentration or early fusion pore structure. However, inhibiting actin polymerization by cytochalasin D prolonged significantly the fusion pore lifetime (Fig. 3.6E) and reduced the fusion pore expansion rate (Fig. 3.6F), explaining the observed increase in ampero-

metric foot duration with unchanged foot current amplitude in amperometric recordings from cytochalasin D-treated cells (Fig. 3.5F & G). This data includes only detected fusion pores with lifetime ≥15 ms. The percentage of fusion pores with lifetime ≥15 ms was similar for control and blebbistatin-treated cells (21% and 30% respectively), but was increased to 51% for cytochalasin D-treated cells.

3.4.7 Distribution of foot signal durations and fusion pore lifetimes

To better characterize the fusion pore kinetics, we constructed survival curves for the detected amperometric foot signal durations (Fig. 3.7A) and fusion pore lifetimes (Fig. 3.7B) for control, blebbistatin-treated and cytochalasin D-treated cells. The survival curves for blebbistatin-treated cells are very similar to those for control cells whereas increased foot duration and fusion pore lifetime is evident for cytochalasin D-treated cells. Accordingly, single exponential fits provided similar time constants τ for foot duration and fusion pore lifetimes in control and blebbistatin-treated cells but about twice as long for cytochalasin D-treated cells (Table 3.1).

However, single exponential fits failed to reproduce the survival curves accurately, as is particularly evident in the logarithmic plots (Fig. 3.7C & D). This indicates that the kinetics is not homogeneous but reflects an inhomogeneous population with a distribution of rate constants. A distribution of activation energies leads to kinetics that is better described by a power law function [59, 60]:

$$f(t) = A\left(1 + \frac{kt}{n}\right)^{-n} \tag{3.2}$$

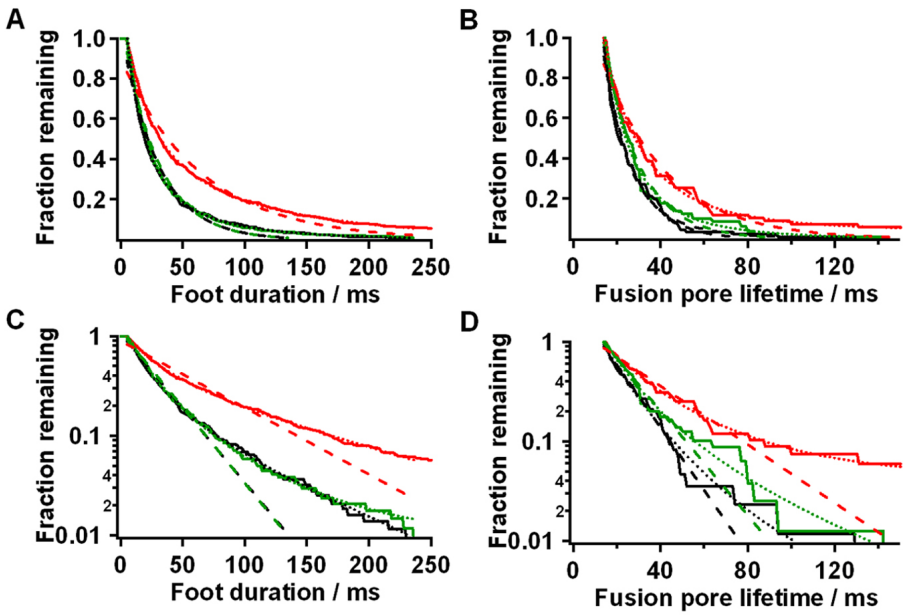

Figure 3.7: Linear plots of survival curves for (A) foot signal duration and (B) fusion pore lifetime. Logarithmic plots of survival curves for (C) foot signal duration and (D) fusion pore lifetime. A single exponential (dashed lines) and a power law function (dotted lines) were fitted to the data. Black: control (n = 7 cells, 86 fusion pores), green: blebbistatin (n = 8 cells, 82 fusion pores), red: cytochalasin D (n = 8 cells, 78 fusion pores).

where A is the distribution amplitude, t the time (or duration), k the rate constant corresponding to the peak of the distribution and n corresponds to the width of the distribution (small n indicates a broad distribution). The power law fits reproduced the data well (Fig. 3.7, dotted lines). Table 3.1 provides the parameters returned from the fitting procedure for each treatment group. Again, the parameters for blebbistatin-treated cells are very similar to those for control cells. For cytochalasin D-treated cells the main difference is a much smaller parameter n, which indicates a much broader distribution of rate constants, extending to much longer foot durations and fusion pore lifetimes when actin polymerization is inhibited.

The fraction of amperometric spikes with detectable foot signal and of fu-

Table 3.1: Fit parameters returned for the single exponential (τ) and power law ($1/k$, n) fits to the foot signal duration (amperometry) and fusion pore lifetime (capacitance) survival curves of each treatment group.

	Amperometry			Capacitance		
Parameter	τ (ms)	$1/k$ (ms)	n	τ (ms)	$1/k$ (ms)	n
Control	28.6 ± 0.4	16.4 ± 0.2	2.4 ± 0.1	13.8 ± 0.2	8.1 ± 0.7	4.7 ± 0.5
blebbistatin	28.4 ± 0.4	18.1 ± 0.2	2.8 ± 0.1	16.5 ± 0.4	7.7 ± 0.8	3.2 ± 0.3
cytochalasin D	63.8 ± 1.1	29.5 ± 0.4	1.6 ± 0.0	29.5 ± 0.7	8.8± 0.8	1.8 ± 0.1

sion pores measured by capacitance measurements with lifetime ≥15 ms was increased in cytochalasin D-treated cells compared to control and blebbistatin-treated cells (Table 3.2). This is consistent with the prolonged foot signal duration (Fig. 3.5G) and the increased fusion pore lifetime in cytochalasin D-treated cells (Fig. 3.6E), which should increase the fraction of foot signals or fusion pores longer than the detection limits of 5 ms and 15 ms, respectively. The fitted data sets included only foot signals with duration ≥5 ms, and fusion pores with lifetime ≥15 ms, since shorter durations were affected by the respective low pass filters used and could thus not be reliably quantified. Table 3.2 compares the fraction of amperometric spikes and fusion events that fulfilled these criteria with the fraction of events predicted by the power law fits. While the fractions of fusion pore lifetimes ≥15 ms are in rather good agreement with the predictions from the power law fits, the fractions of amperometric spikes with a detectable foot signal is much lower than the predictions of the power law fit. However, this is not unexpected since foot signals may escape detection not only because of short duration, but also due to small amplitude. The mean foot current amplitude calculated for all detected foot signals (not averaged per cell) was 3.5 ± 2.8 pA (mean ± s.d.) for control cells and similar for drug-treated cells. Since the detection limit was 1 pA, a significant fraction of foot signals with duration >5 ms will not be detected due to small amplitude.

Table 3.2: Comparison of percentage of detected amperometric foot signals and capacitance fusion pores with predictions from power law fits for each treatment group.

	Amperometry spikes with detectable foot	Expected fraction of foot signals ≥5 *ms* from power law fits	Fusion pores with lifetime ≥15 *ms*	Expected fraction of fusion pore lifetimes ≥15 *ms* from power law fits
Control	33%	75%	21%	23%
blebbistatin	35%	77%	30%	24%
cytochalasin D	45%	85%	51%	32%

3.5 Discussion

3.5.1 Reduced vesicular motion following inhibition of myosin II activity

Inhibition of myosin II reduced chromaffin granule mobility, consistent with previous reports [61, 48]. In contrast to cytochalasin D treatment, inhibition of myosin II did not lead to reduction of cortical actin filaments, indicating that the role of myosin II in chromaffin vesicle motion near the cell surface is not mediated by disintegration of the actin-rich cortex. Although myosin motor function is highly regulated [62], myosin activity at resting calcium concentration appears to contribute to vesicle mobility.

3.5.2 Frequency of exocytotic events

Inhibition of actin polymerization by cytochalasin D or latrunculin A led to a 66% increase in the number of exocytotic spikes consistent with the role of actin as a physical barrier to exocytosis [45]. Blebbistatin treatment of chromaffin

cells, however, did not result in a change of the number of measured exocytotic spikes, consistent with the presence of normal cortical actin filaments in these cells. In contrast, the non-specific MLCK inhibitor ML-7 reduced the number of exocytotic events, suggesting that ML-7 inhibits exocytosis via a mechanism that may not be mediated by inhibition of nonmuscle myosin II [63].

3.5.3 Inhibition of myosin II function or actin polymerization slows catecholamine release during amperometric spike phase

Inhibition of myosin II increased the average amperometric spike half-width, consistent with experiments using chromaffin cells overexpressing an unphosphorylatable mutant of the myosin II RLC [48]. Inhibition of actin polymerization by cytochalasin D broadened the amperometric spikes even more than blebbistatin. Myosin II could thus exert its role via interaction with or independent of actin. It has been suggested that tension in the vesicle membrane drives fusion pore expansion [64] and myosin II and actin may contribute to increased membrane tension helping to expand the fusion pore. It has so far not been possible to measure directly the fusion pore conductance in chromaffin cells during the amperometric spike. However, fusion pore dynamics can be resolved for the early fusion pore that gives rise to the amperometric foot signal. If F-actin and myosin II accelerate fusion pore expansion, we would expect that this should be reflected in the dynamics of the early fusion pore.

3.5.4 Modulation of early fusion pore expansion by F-actin but not myosin II activity

Indeed, inhibition of actin polymerization resulted in prolonged fusion pore lifetimes indicated by increased amperometric foot signal durations and increased narrow fusion pore lifetimes determined by cell-attached capacitance measurements. The fusion pore expansion rate was reduced while the initial and average fusion pore conductance as well as the average foot signal amplitude were unchanged. We conclude that cortical actin does not determine the structure of the early fusion pore, but facilitates the process of fusion pore expansion. Survival curves constructed for amperometric foot signal durations and fusion pore lifetimes were well fitted with power laws as expected for processes that reflect distributed kinetics based on a distribution of activation energies [59, 60, 65]. Fusion pore expansion is modulated by many factors including Ca^{2+} concentration [66, 67] and PKC [68] such that a kinetic heterogeneity is not unexpected. Inhibition of actin polymerization broadened the kinetic distribution towards longer fusion pore lifetimes providing the first direct evidence that actin contributes to fusion pore expansion in chromaffin cells.

Inhibition of myosin II activity, on the other hand, altered neither the early fusion pore structure, nor the fusion pore expansion rate or the early fusion pore lifetime, suggesting that myosin II is not mediating the role of actin during the early fusion pore. In contrast to our results, the expansion of the early fusion pore was slower in chromaffin cells overexpressing an inactive form of myosin II RLC [49]. One possible explanation for this apparent discrepancy would be that blebbistatin inhibition of myosin II may be incomplete and that the residual myosin II activity in blebbistatin-treated cells is sufficient to maintain normal

fusion pore expansion kinetics. However, alternative explanations are at least equally possible. In our experiments blebbistatin treatment was performed for 15 *min* prior to the measurements. In contrast, cells overexpressing the inactive form of myosin II RLC were used one or more days after infection. Blebbistatin inhibition thus reveals the immediate consequences of myosin II inhibition and presumably its direct function in the release event. On the other hand, overexpression experiments may in addition reveal longer term consequences. The changes in early fusion pore expansion may reflect longer term consequences of myosin II inhibition such as changes in vesicle maturation, docking or priming. The two experimental approaches are thus not directly comparable and provide complementary information.

Despite normal early fusion pore dynamics, amperometric spike half-width was significantly increased in blebbistatin-treated cells, suggesting that the increased amperometric spike half-width may not be due to slower fusion pore expansion. It was suggested that dissociation from the granular matrix is the major process determining amperometric spike half-width [69, 70]. The amperometric spike time course shows no strong correlation with quantal size [71] as would be expected for a rate limiting fusion pore. The time course of release of different granular contents from cytochalasin D-treated PC-12 cells was also not correlated with the size of the particular compound, as would be expected for fusion pore limited release [72]. These results suggest that association with and dissociation from the intragranular matrix determine the kinetics of release. Additional support for this view came from a recent study showing that release events from chromogranin A null mice exhibit reduced amperometric spike half-widths [73].

3.5.5 Possible mechanisms for F-actin and myosin II function in exocytosis

The relaxation of membrane tension exerted by actin filaments on the cell plasma membrane in cytochalasin D-treated cells may be responsible for slower fusion pore expansion. In contrast, inhibition of myosin II had no detectable effect on early fusion pore expansion suggesting that actin mediates fusion pore expansion by its interactions with other proteins.

Myosin II, however, contributes to accelerating release during the amperometric spike. How can interactions of the extra-granular actin and nonmuscle myosin II modulate catecholamine release kinetics from chromaffin granules? Our results suggest that mechanical forces (tension) on the granules may promote dissociation from the matrix and thus expel catecholamines. It has been proposed that in Xenopus eggs, cortical granules are compressed by F-actin during exocytosis, contributing to the driving force for granules to secrete their contents [74]. Nonmuscle myosin II may exert its mechanical function on chromaffin granules by its ability to bind and contract filamentous actin. Release from the matrix appears to be governed by a low effective diffusion coefficient within the matrix [75]. The change in amperometric spike width might be a consequence of a changed effective diffusion coefficient that could result from mechanical forces exerted on the matrix affecting its catecholamine binding interactions. Alternatively it could be a consequence of a changed rate at which the surface of the granule matrix is exposed to the extracellular medium [75] or the size of the exposed matrix area during the rapid release phase giving rise to the amperometric spike. However, considering that the amperometric spike time course appears to be independent of vesicle size the latter mechanism

would require that the rate at which the membrane surrounding the vesicle is unwrapped or the finally exposed area is increased for larger vesicles. In either case, the role of myosin II is likely to exert mechanical forces on the granule by matrix compression or by expelling the matrix more rapidly, thus facilitating release by exposing the whole granule core to the extracellular solution and accelerating dissociation from the granular matrix.

The interactions between the vesicles and the cortical actin cytoskeleton could be mediated by myosin V, which has been localized to chromaffin granules [47], providing a possible link between an actin-myosin II scaffold and the secretory granule. However, interactions of myosin II with chromaffin granules should not be ruled out. The interaction of the secretory granules with actin filaments appears to be mediated by localized adaptor molecules, such as N-Wasp and ARP2/3 [76] or Rab27A and MyRip [77]. One possibility is that upon stimulation the actin cortex redistributes to allow granules to collapse [78]. However, residual polymerized actin at the immediate fusion site may persist due to localized accessory molecules allowing actin-regulating proteins, such as myosin II to exert control on granule fusion. It thus appears possible that myosin II may dynamically interact with actin and secretory granules via currently unidentified adaptor proteins.

3.6 Note to Chapter 3

The author is indebted to Alexis Torres who performed in their entirety the vesicle tracking and the actin labeling experiments. The author would also like to thank Dr. Qinghua Fang for the cell-attached capacitance measurements and

Kassandra Kisler for her help with the Fura-2 measurements. The material in Chapter 3 has been published in The Journal of Neuroscience [79].

CHAPTER 4

IMPROVED ELECTROCHEMICAL DETECTOR ARRAYS FOR MONITORING EXOCYTOSIS

4.1 Abstract

Surface patterned platinum microelectrodes (PtEs) insulated with 300 *nm* thick fused silica were fabricated using contact photolithography. These electrodes exhibit low noise and were used for monitoring single vesicle exocytosis from chromaffin cells by constant potential amperometry as well as fast scan cyclic voltammetry. Amperometric spike parameters were consistent with those obtained with conventional carbon fiber electrodes (CFEs). Catecholamine voltammograms acquired with PtEs exhibited redox peaks with full width at half maximum of ~45 mV, much sharper than those of CFE recordings. The time course of voltammetrically measured release events was similar for PtEs and CFEs. The fused silica insulated PtEs could be cleaned and reused repetitively and allowed incorporation of micrometer precision surface patterned poly-D-lysine (PDL). PDL-functionalized devices were applied to stimulate mast cells and record single release events without serotonin pre-loading. Microfabricated PtEs are thus able to record single exocytotic events with high resolution and should be suitable for highly parallel electrode arrays allowing simultaneous measurements of single events from multiple cells.

4.2 Introduction

Exocytosis is a fundamental cellular mechanism by which cells extrude the contents of membrane bound vesicles into the extracellular space. Many techniques have been employed to investigate single exocytotic events including whole cell patch clamp capacitance measurements [17, 16, 19, 18], cell attached capacitance measurements [21, 22, 23, 20], carbon fiber amperometry [24, 25, 26], patch amperometry [27, 28, 29], and total internal reflection fluorescence microcopy [11, 12, 13, 14, 15].

The probably most widely used method for the study of single exocytotic events utilizes a CFE [36], which records the release of oxidizable compounds, such as catecholamine release from chromaffin cells [24, 25, 26] or even dopamine release from dopaminergic neurons [80, 81, 82, 83] at extraordinary resolution. Low noise and high temporal resolution have been achieved, due to the CFE's small size and fast response time.

There are, however, two limitations to the CFE technique: (i) To obtain statistical significance, experiments need to be performed on a large number of cells [84, 56], which is time consuming for single cell experiments under a microscope, and (ii) the simultaneous electrochemical detection of release and fluorescence imaging of the same vesicle is not readily possible. Fluorescence imaging can often provide important complementary information on vesicle motion [15] or molecular events associated with vesicle exocytosis [30].

To overcome this limitation, surface patterned electrochemical microelectrodes have recently been fabricated using platinum (Pt) [41, 42] or indium-tin-oxide (ITO) [85, 86] as the working electrode material. Here, we describe an

improved design of reusable surface-patterned, glass insulated platinum electrodes (PtEs) and characterize their properties in amperometric as well as fast-scan cyclic voltammetric modes for their use in the study of single exocytotic events.

4.3 Materials and methods

4.3.1 Cell preparation, reagents and solutions

Bovine chromaffin cells were cultured on 8 *mm* glass coverslips as described [50]. Mast cells were isolated from the peritoneum of adult Sprague-Dawley rats as described [87]. The solution used for all electrochemical recordings contained (in *mM*) 140 NaCl, 5 KCl, 5 $CaCl_2$, 1 $MgCl_2$, 10 HEPES/NaOH, 20 glucose (pH 7.3). Dopamine hydrochloride, (±)-Epinephrine hydrochloride, DL-Norepinephrine hydrochloride, and Poly-D-Lysine (PDL) were all purchased from Sigma (Milwaukee, WI) and used without further purification. Experiments were performed at room temperature, at day 1 after isolation for chromaffin cells and at the day of isolation for mast cells.

4.3.2 CFE fabrication

CFEs were fabricated as described [24]. Briefly, a single carbon fiber (5.0 μm diameter) was inserted in a borosilicate glass capillary (1.8 *mm* outer diameter, Hilgenberg GmbH, Germany). The capillary was then pulled using a pipette puller (Model P-97, Sutter instrument) producing two CFEs, which were sepa-

rated with scissors. CFE tips were dipped in melting wax (Sticky Wax, Kerr Corporation) for 2 *min* and subsequently cut using a blade (No 10, Feather Safety Razor Co, Japan). Prior to experiments, CFEs were backfilled with 3 *M* KCl solution.

4.3.3 PtE microfabrication

Single, triple, or quadruple PtEs were surface patterned on 4″ diameter borosilicate glass wafers of thickness 160-190 μm (ThermoFisher Scientific, Portsmouth, NH) using contact photolithography techniques and metal lift-off using the following protocol:

1. Clean the wafer by rinsing with acetone while the wafer is spinning.
2. Bake the wafer on a hotplate for ~3 *min* at 115^oC. This step enhances the effectiveness of the vapor priming (next step).
3. Vapor prime the wafer surface with hexamethyldisilazane (HMDS) in a YES LP-III (Yield Engineering Systems, Inc., Livermore, CA) oven.
4. Spin coat the wafer with Shipley S1813 photoresist. Spin the wafer at 4,000 rpm for 30 s (ramp up at 10,000 rpm/s, ramp down at 2,000 rpm/s for 2 s).
5. Soft bake the wafer on a hotplate at 115^oC for 1 *min*.
6. Place the wafer in a contact aligner (i.e. EV620, EV Group, Schärding, Austria). Use the metal layer mask to selectively expose the photoresist to UV light.
7. Bake the wafer on a hotplate for 2.5 *min* at 115^oC (post-exposure bake).
8. Bake the wafer with NH_3 in a YES oven (image reversal).

9. Expose the entire wafer to UV light for 60 *s* using a contact aligner.

10. Develop the photoresist in AZ©300MIF for 1 *min*. 300 MIF is a positive-photoresist developer, which contains 2.38% by weight tetramethyl ammonium hydroxide (TMAH).

11. Descum the photoresist using O_2 plasma clean for 30 *s* with PT 72 (Plasma Therm Inc., Kresson, NJ).

12. Place the wafer in an evaporator, deposit 5 *nm* of the desired adhesion layer metal (either Cr or Ti) at a ~1 Å/*s* deposition rate. After depositing the adhesion layer, evaporate 150 *nm* of Pt at a ~5 Å/*s* deposition rate.

13. Place the wafer upside down in a beaker containing the Microposit remover 1165 (Shipley Co Inc, Austin, TX) and set aside for a few hours for the photoresist to come off (metal lift-off). Rinse the wafer thoroughly with isopropanol while removing from the beaker, to avoid metal sheets from sticking on the electrodes.

14. Remove the wafer from the beaker and rinse with methanol.

15. Deposit 300 *nm* of SiO_2 using a plasma-enhanced chemical vapor deposition (PECVD) system (IPE 1000). Use silane (SiH_4) and nitrous oxide (N_2O), keeping chamber temperature to 240^oC. These conditions should result in a SiO_2 deposition rate of ~40 *nm*/*min*.

16. Vapor prime the wafer surface with HMDS as above.

17. Spin coat the wafer with S1813 photoresist as above.

18. Soft bake the wafer on a hotplate at 115^oC for 1 *min*.

19. Place the wafer in a contact aligner (i.e. EV620 as above), and expose to UV light after aligning the insulation layer mask with the metal that has already been deposited onto the wafer.

20. Bake the wafer on a hotplate for 2.5 *min* at 115^oC (post exposure bake).
21. Develop the photoresist using 300 MIF as above.
22. Descum the photoresist as above.
23. Hard bake the wafer on a hotplate for 5 *min* at 115^oC in order to harden the photoresist, such that it will not easily etch during the next step.
24. Etch the SiO_2 using trifluoromethane (CHF_3) and oxygen (O_2) at a ratio of 50 *sccm*/2 *sccm*. The Oxford 80 (PlasmaLab 80+, Oxford Instruments, Oxfordshire, UK) can be used for this step. The etching should be performed for ~ 12 *min* (consult updated etching rates for the instrument).
25. To remove the remaining photoresist, place the wafer in a beaker containing nanostrip: sulfuric acid (H_2SO_4) and hydrogen peroxide (H_2O_2). In some cases it will be necessary to use q-tips to gently remove the photoresist from the wafer.
26. Cut wafer into 2.5x2.5 cm^2 pieces using a wafer saw.

A photograph of a coverslip containing PtEs is shown in Fig. 4.1.

4.3.4 Chemical functionalization

For mast cell recordings, coverslips with microfabricated PtE arrays were coated with ~1 μm thick Parylene-C using a Model PDS 2010 Labcoter (Specialty Coating Systems, Indianapolis, IN), followed by spin coating of ~1.3 μm thick S1813 photoresist. A 5 μm diameter circular region of the photoresist at the center of the PtE array or next to a single PtE was removed using standard photolithography techniques, and the exposed Parylene was etched with a reactive ion etcher

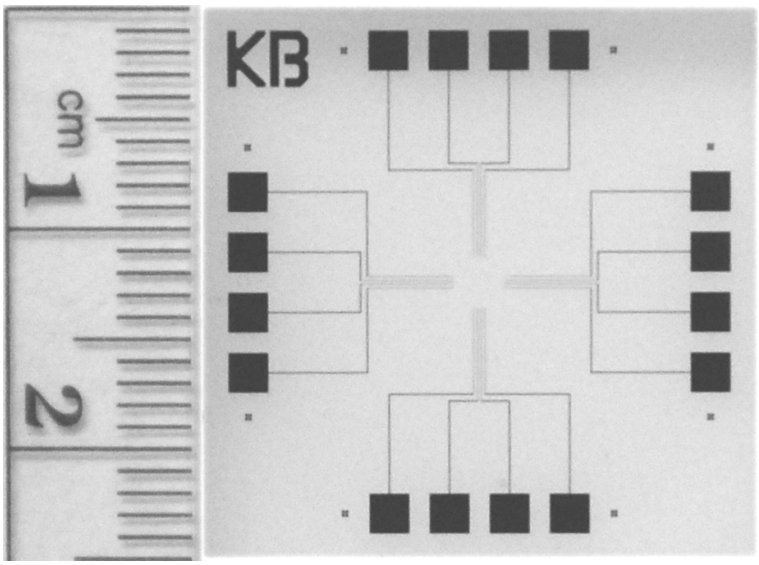

Figure 4.1: A photograph of a coverslip containing four PtE arrays, each containing four electrodes. Photo: courtesy of O.D. Escanilla.

(PlasmaTherm 72). 10 μL of 0.1% PDL in distilled water was applied to the surface (Fig. 4.2A), after allowing 1 h for surface coating the unbound PDL was washed off with distilled water. The coverslips were dried at room temperature for 15 *min* and stored overnight at 4^{o}C after which the Parylene was carefully removed using tweezers. Thus, the PtE array center was selectively coated with PDL (Fig. 4.2B). Prior to the electrochemical recordings, ~100 μL of freshly isolated mast cell suspension was added via a pipette onto the coverslips.

4.3.5 Amperometry

Coverslips containing the electrochemical detectors were mounted on a custom built stage for a Zeiss 135TV microscope. Platinum electrodes were connected to the amplifiers via spring loaded gold contact pins and individual cells were placed on the electrodes as described [41, 42]. Amperometry was performed

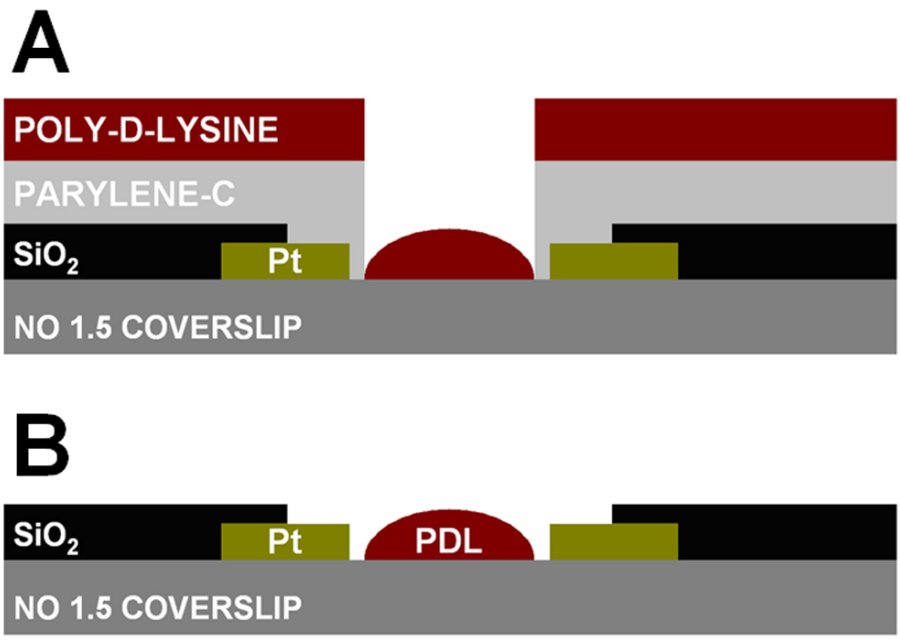

Figure 4.2: Schematic of the surface patterning of PDL on the PtE arrays before (A) and after (B) dry lift-off.

with a four-channel amplifier (VA-10, NPI Electronic, Tamm, Germany). The measured current was low pass filtered at 100 Hz using the built-in analog low pass filter of the VA-10 amplifier. The electrodes were held at +700 mV versus an Ag|AgCl wire immersed into the bath solution. Amperometric data was digitized at 2 kHz sampling rate using a 16-bit resolution analog-to-digital (A/D) converter (BNC-2090, NIDAQ, National Instruments, Austin, TX). If necessary, line frequency noise was removed by fitting a sine wave (baseline, amplitude, frequency and phase) to portions of the recordings without any amperometric spikes and subsequently subtracting the resulting sine wave from the data [41]. Amperometric spike parameters were extracted as described [56] using procedures written in Igor Pro. The criteria used for identifying amperometric spikes were 10 pA minimum amplitude and 100 ms maximum half-width. The thresholds used for identifying foot signals were 1 pA amplitude and 5 ms duration.

4.3.6 Fast-scan cyclic voltammetry

Fast-scan cyclic voltammetry was performed with an EPC-8 patch-clamp amplifier (HEKA-Elektronik, Lambrecht, Germany). The amplifier's built-in analog low pass filter was set to 5 kHz. The standard voltage waveform applied to the working PtE versus the reference Ag|AgCl wire consisted of a 10 ms triangular segment, during which the electrode voltage was scanned from -500 mV to +1,000 mV and back to -500 mV at a rate of ±300 V/s. The triangular segment was followed by a 90 ms resting period during which the electrode potential was held constant at -500 mV. For experiments at increased time resolution (see Results) the duration of the resting period was reduced to 15 ms and the ramp speed was doubled to ±600 V/s, while the resting and peak potentials remained unaltered. Voltammetric currents were digitized at a rate of 25 kHz using a 16-bit A/D converter (ITC-18, Instrutech Corp, Bellmore, NY), and analyzed using procedures written in Igor Pro [88].

4.4 Results

4.4.1 Chromaffin cell amperometry

Fig. 4.3A shows an electron microscope (Zeiss Supra 55VP) image of a 3-electrode PtE array insulated with SiO_2. The oxide layer is highly uniform and homogenous. Bovine chromaffin cells were placed on top of PtE arrays using a patch pipette as described [41, 42]. The placement procedure stimulated exocytotic catecholamine release which was recorded by the PtE array.

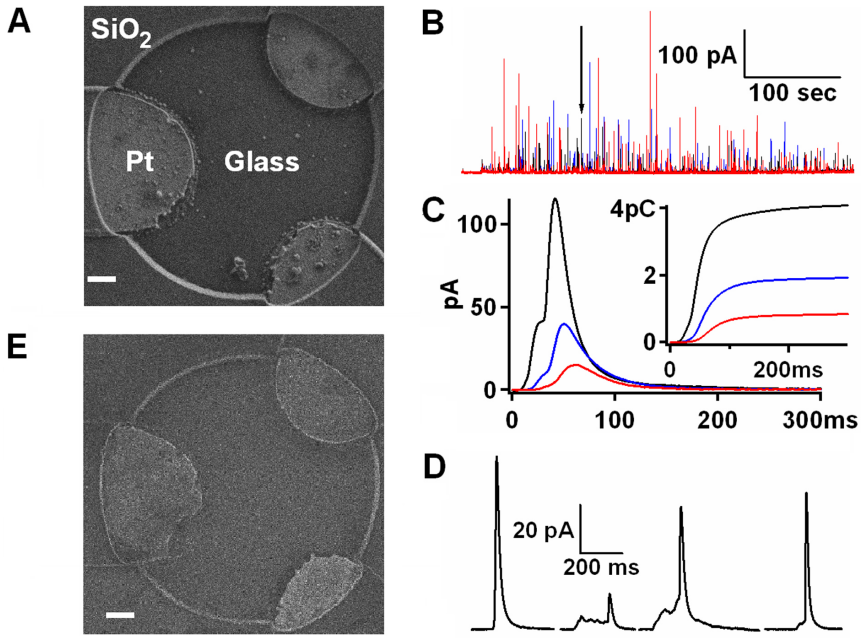

Figure 4.3: (A) Electron microscope image of a PtE array immediately after fabrication. Scale bar: 1 μm. (B) A characteristic amperometric recording from the 3-electrode Pt array of (A). Different colors represent signals measured by different electrodes in the array. (C) The exocytotic event indicated by the arrow in (B) is shown on an expanded time scale. The inset shows the integrated traces which correspond to the charges measured by each electrode. (D) Four different exocytotic events from the recording in (B). (E) Electron microscope image of the same PtE array as in (A) after multiple single cell experiments and alcohol cleanings. Scale bar: 1 μm.

Fig. 4.3B shows an amperometric recording with this 3-electrode array from a chromaffin cell that produced more than 100 exocytotic events, many of which were detected by multiple electrodes. From the total of 138 identified events of this recording, 102 were detected by at least two electrodes and 55 by all three electrodes. Employing multiple electrodes allows for spatial localization of the individual exocytotic events provided that amperometric signals are detected by at least three electrodes [42].

Fig. 4.3C shows on an expanded time scale the single amperometric event indicated by the arrow in Fig. 4.3B. The inset of Fig. 4.3C shows the running in-

tegrals of the current traces, which indicate the time course of measured charge by each electrode. The sum of the final values of the three integrated traces corresponds to the vesicle quantal size, which for this particular event is 6.9 pC or ~21.6 million molecules.

Four distinct events from the recording of Fig. 4.3B are shown on an expanded time scale in Fig. 4.3D. These events have short half-widths and significantly different foot signal time courses, demonstrating that PtEs can closely follow the time course of catecholamine release from individual chromaffin granules. To quantify the performance of microfabricated PtEs, the amperometric spikes were analyzed as described [56] for quantal size, half-width, foot signal duration and foot signal mean amplitude. Quantal size was measured as the sum of charges detected by all electrodes. The three other parameters were derived from the amperometric spike measured by the electrode located closest to the release site (shortest half-width).

The averaged quantal size was 1.82 ± 0.15 pC and the averaged half-width 13.8 ± 0.6 ms (mean ± sem, n = 138 events). Out of the total of 138 individual spikes, 90 had detectable foot signals (65%), with average foot signal duration 11.1 ± 3.7 ms and foot signal mean amplitude of 4.0 ± 0.4 pA (mean ± sem, n = 90 events). The averaged values of the four parameters are similar to those reported for CFEs [25, 89].

To determine the PtE noise, the stored current traces were examined at 1 s segments which did not contain any amperometric spikes. The measured standard deviation of the noise was 75 ± 15 fA (mean ± sd, n = 3 electrodes, Δf = 100 Hz), indistinguishable from the amplifier's feedback resistor (500 $M\Omega$) Johnson noise, which was measured to be 65 fA with the head stage in the open circuit

configuration. The measured noise did not differ significantly from the theoretically expected noise level σ_I, which can be calculated as $\sigma_I = \sqrt{\frac{4kT\Delta f}{R}}$ [37], where k is the Boltzmann constant, T the temperature in degrees K, Δf the low-pass filter's cutoff frequency, and R the feedback resistor's resistance value.

In addition to low current noise, the SiO_2-insulated PtEs were mechanically and chemically robust, since multiple single cell experiments followed by ethanol cleaning of the PtE coverslips did not damage the electrodes (compare Fig. 4.3A & E).

4.4.2 Mast cell amperometry

In contrast to excitable cells, exocytosis of mast cells is not mediated by ion channel activation, but by chemical signaling [90]. To determine if PtEs can be utilized to record exocytosis from rat peritoneal mast (RPM) cells, PtEs were functionalized with PDL, an established activator of RPM cell exocytosis [91].

A 5 μm diameter circular region at the center of the PtE array was selectively coated with PDL using the dry lift-off technique [92] (see Materials and Methods). A single RPM cell (Fig. 4.4A) was lifted with a glass micropipette and manipulated on top of a single PtE (Fig. 4.4B), the area in front of which was previously coated with PDL (Fig. 4.4C). Shortly after placement on top of the electrode, the cell degranulated and a series of amperometric events was recorded by the PtE (Fig. 4.4D). Amperometric events with quantal size as low as 9.5 fC were resolved, corresponding to the measurement of ~14,800 serotonin molecules, since electrochemical oxidation of serotonin results in the donation of four electrons per molecule [93]. PtEs can thus measure very small

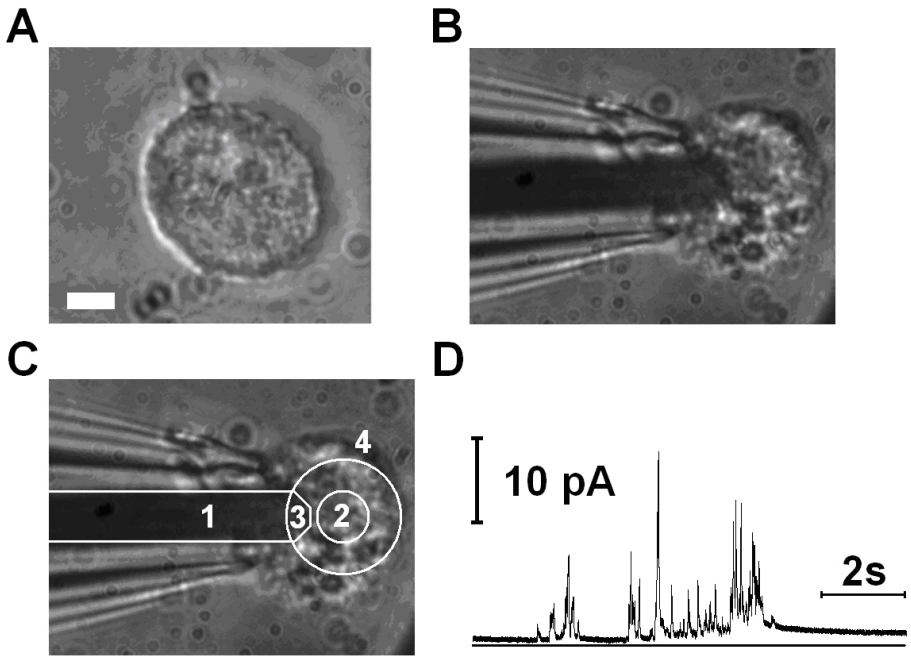

Figure 4.4: (A) A peritoneal mast cell. Scale bar: 5 μm. (B) The mast cell of (A) on top of a single PtE. (C) Different regions indicated by numbers. 1: SiO_2 insulated part of Pt conductor, 2: PDL coated area, 3: exposed area forming the active PtE, 4: All the area outside the large circle including area 1 is covered with the SiO_2 insulation layer. (D) The corresponding amperometric recording from the cell shown in (B).

amounts of electroactive compounds.

From twelve mast cells placed on top of two different PtE arrays that were not functionalized with PDL, only two amperometric spikes were recorded. The functionality of the PtE arrays was subsequently verified using catecholamine solutions. This indicated that unlike chromaffin cells, mast cells were not stimulated by the mechanical placement procedure.

4.4.3 Fast-scan cyclic voltammetry

While constant potential amperometry can measure single vesicle release with high resolution, it does not allow identification of the detected compound. Such identification is, however, possible using fast scan cyclic voltammetry (FSCV), as demonstrated for CFE detection of catecholamines [94, 24, 95].

To determine if microfabricated PtEs can also be utilized as the working electrodes for FSCV, the potential waveform shown in the inset of Fig. 4.5 was applied to the PtEs. In physiological saline the resulting current during the voltage ramps is largely due to charging of the double layer capacitance, and is known as the background current. In the presence of electrochemically active compounds in the buffer solution, the resulting current consists of the background current plus a faradaic current due to the redox reactions at the electrode surface [38]. Subtraction of the background current results in the difference current, which when plotted versus the applied potential gives the background-subtracted voltammogram. The background-subtracted voltammograms for the catecholamines DA, norepinephrine (NE) and epinephrine (EPI) contain two peaks, one at positive potential due to oxidation of the catecholamine to its quinone form, and a second at negative potential due to reduction of the quinone back to the original catecholamine [96].

For the background-subtracted voltammogram it is essential that the background current is stable between successive measurements. For three electrodes of $10\,\mu m^2$ active area the current at +160 mV applied potential of the anodic ramp was monitored for 10 s segments and the measured standard deviation was 8 ± 2 pA (mean ± sd, n = 3 electrodes, $\Delta f = 5\ kHz$), which does not exceed the Johnson noise of the amplifier's feedback resistor and the A/D converter quan-

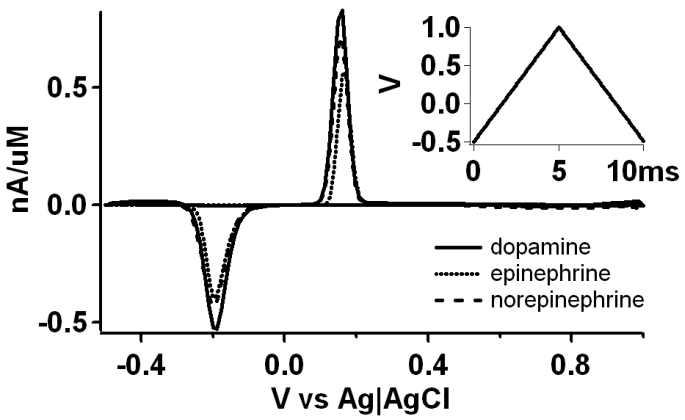

Figure 4.5: *In vitro* background subtracted voltammograms obtained from PtEs after addition of 1 μM DA, NE or EPI respectively. Inset: potential waveform applied to the PtEs.

tization error (~6 pA). The background current of SiO_2-insulated PtEs was thus very stable between successive voltammetric measurements.

In vitro calibrations of PtEs using 1 μM concentrations of the catecholamines DA, NE and EPI resulted in similar background-subtracted voltammograms for all three compounds (Fig. 4.5). The voltage waveform of Fig. 4.5 (inset) was chosen because the negative resting potential promoted adsorption of catecholamines onto the Pt surface, in a fashion similar to that for CFEs [97].

In several cases it was not possible to remove the catecholamines from the PtE surfaces such that catecholamine voltammograms remained detectable in plain buffer even after washing the PtEs with alcohol, distilled water, or oxygen plasma clean. This is presumably due to adsorption of catecholamines on the PtEs [98]. The adsorbed catecholamines were only removed from the electrode surfaces when 0.18 M H_2SO_4 was added onto the PtEs and the electrode potential was scanned at a rate of 100 mV/s between -500 mV and +975 mV. In some cases it was necessary to perform this electrochemical cleaning for up to 1 h,

until the cyclic voltammogram of a pure Pt surface was detected [38].

In addition to the difficulty of removing the catecholamines from the PtE surfaces, some PtEs did not produce a catecholamine voltammogram as shown in Fig. 4.5, although their functionality was verified via amperometric detection of catecholamines. The reasons for this malfunction remain elusive.

4.4.4 Chromaffin cell voltammetry

To test if PtEs could detect cellular release events in FSCV mode, individual chromaffin cells were placed on top of single PtEs (Fig. 4.6) while the voltage waveform of Fig. 4.7A (inset) was applied to the PtE. As in amperometry, the placement procedure stimulated the cells and voltammetric spikes indicating chromaffin vesicle exocytosis [24] were observed. The time course of the current sampled at the +230 mV applied potential of the anodic ramp is shown in Fig. 4.7A for successive sweeps.

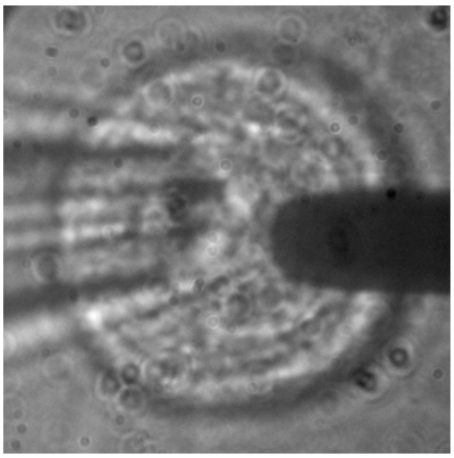

Figure 4.6: A single chromaffin cell (middle) placed via a pulled glass pipette (left) on top of a PtE (right).

Fig. 4.7B shows the background current (dashed black trace, corresponding in time to the arrow marked **a** in Fig. 4.7A), the background plus faradaic current (solid red trace, corresponding in time to the arrow marked **b** in Fig. 4.7A), as well as their difference (solid blue trace). The difference current was plotted versus the applied potential and revealed the signature voltammogram of catecholamine molecules (Fig. 4.7C), with two peaks, the first at +230 *mV* of the anodic ramp and the second at -260 *mV* of the cathodic ramp. As is the case with CFEs [88], the redox peaks of Pt difference voltammograms consistently occurred at slightly different potentials in single cell experiments (Fig. 4.7C) compared to *in vitro* calibrations (Fig. 4.5).

The background current of the PtE was very stable, such that no sweep averaging was necessary to obtain the voltammograms. We conclude that SiO_2-insulated PtEs are suitable for low-noise FSCV applications to measure exocytotic release of oxidizable transmitter molecules.

4.4.5 PtE versus CFE voltammetry

Fig. 4.8A compares catecholamine voltammograms measured during release from single chromaffin cells with a PtE (black) and a CFE (red) after normalizing to their respective peak oxidation currents. The voltammograms obtained with CFEs are in good agreement with those previously reported [99, 88], with oxidation/reduction peaks at +435 *mV* and -350 *mV* respectively.

In contrast, the peaks for the Pt voltammogram are shifted to approximately +230 *mV* and -260 *mV* for oxidation and reduction respectively. Interestingly, the full width at half maximum (FWHM) of the oxidation peaks of voltammograms

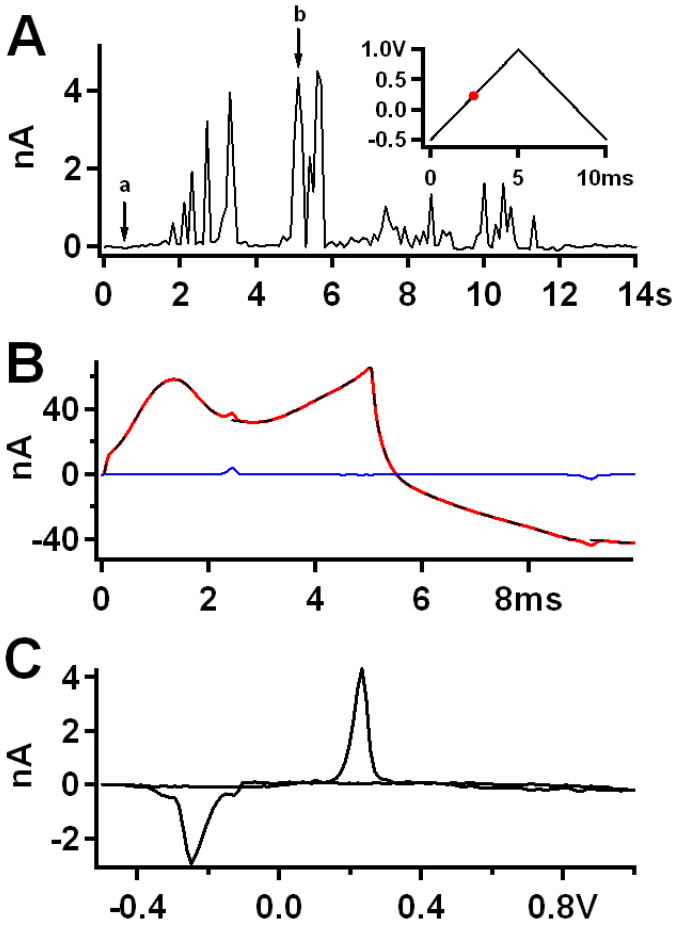

Figure 4.7: (A) Catecholamine release indicated as current spikes recorded by a PtE. The current was sampled at the +230 mV applied potential of the anodic ramp. The average value of the first 10 cycles was subtracted from the current trace. The inset shows the applied potential waveform. The red dot indicates the voltage at which the current was sampled (+230 *mV* of the anodic ramp). (B) Background (dashed black trace, corresponding to the vertical arrow marked **a** in panel (A)), background plus faradaic (solid red trace, corresponding to the vertical arrow marked **b** in panel (A)), and their difference (blue trace). (C) The difference current plotted versus the applied potential reveals the voltammogram for catecholamine molecules with an oxidation peak at +230 *mV* and a reduction peak at -260 *mV*.

obtained with PtEs was ~45 *mV*, which corresponds to the Nernstian limit for a 2-electron transfer reaction [38], indicating very rapid catecholamine oxidation. The FWHM for the CFE oxidation peak was ~310 *mV*, ~7-fold larger than the

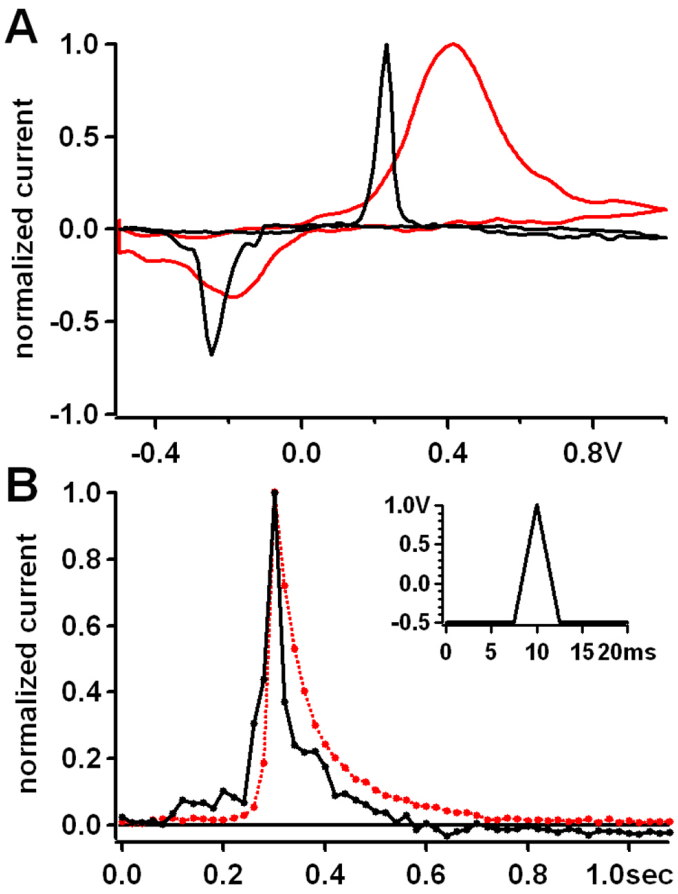

Figure 4.8: (A) Typical cyclic voltammograms normalized to their peak oxidation values, obtained from chromaffin cells using either Pt microelectrodes (black) or CFEs (red). (B) Time course of voltammetric spikes for Pt (black) and CFE (red). Curves are the average of 20 individual spikes measured with 20 *ms* time resolution using the voltage waveform shown in the inset.

corresponding value for Pt, which can be accounted for by the greater density of states of Pt compared to carbon [100].

Another interesting characteristic of catecholamine voltammograms is that the reduction peak is usually significantly smaller than the oxidation peak, presumably due to diffusion of the oxidized quinone away from the electrode surface. For the voltammograms of Fig. 4.8A, the reduction peak measured with PtEs was ~73% of the oxidation peak, while the reduction peak was decreased

to ~55% of the oxidation peak for the CFE.

The higher reduction to oxidation ratio suggests stronger adsorption of catecholamines onto PtEs [98] compared to CFEs. To determine if this affects the time course of voltammetric spikes we compared single events measured with CFEs and PtEs. For increased time resolution the resting period of the applied potential waveform was reduced to 15 ms and the ramp speed was increased to ±600 V/s resulting in a voltage waveform of 20 ms total duration and thus a higher temporal resolution for the FSCV measurements (Fig. 4.8B inset).

Using this waveform, single exocytotic events were recorded using PtEs and CFEs. The half-widths of voltammetrically measured spikes are determined not only by the granule secretion time course, but also by the diffusion of the catecholamine molecules away from the electrode surface and the low temporal resolution of the measurements (20 ms). Fig. 4.8B shows the average time course of the 20 largest voltammetric spikes recorded with PtEs or CFEs. For this purpose, spikes were normalized to their peak amplitude, aligned in time at the point of their maximum value and averaged. The average time course appears to be slightly faster for PtEs. However, the measured mean half-width of voltammetric spikes from chromaffin cells was 56 ± 5 ms (mean ± sem, n = 59 spikes) for PtEs and 71 ±11 ms (mean ± sem, n = 31 spikes) for CFEs was not significantly different (p = 0.17). The value obtained with CFEs is in excellent agreement with data reported in the literature [39].

4.5 Discussion

The electrode of choice for electrochemical recordings from biological cells has traditionally been the carbon fiber electrode [101]. Recently, however, Au was utilized as the working electrode in catecholamine measurements *in vitro* [102], while recordings of transmitter release from single chromaffin vesicles were performed using Pt working electrodes [41, 42].

Microfabricated PtE arrays [41] can correlate amperometric and fluorescence measurements corresponding to the same single exocytotic event [42]. Here, we described an improved design of the PtE arrays and its application in FSCV recordings and stimulus-secretion coupling.

Insulating the PtE arrays with fused silica (SiO_2) increases the robustness of the devices (compare Fig. 4.2A & E) allowing cleaning and multiple use, thus reducing electrode fabrication time and cost. Contrary to photoresist, SiO_2 insulation does not exhibit autofluorescence, which improves sensitive fluorescence measurements. Furthermore, our sensor's low electrical noise, as demonstrated in the present study, makes it suitable for electrochemical monitoring of exocytosis in cell systems that release small number of electroactive molecules per vesicle, such as mast cells or dopaminergic neurons.

The SiO_2 insulation makes it furthermore possible to incorporate surface patterned stimuli for the study of stimulus-secretion coupling. RPM cells can be stimulated by a chemical cue patterned with micrometer spatial resolution [103]. Here, we show that this can be combined with secretion measurements using SiO_2 insulated PtEs.

PtE arrays may also be used for parallel recording by multiple cells at the single cell level, particularly utilizing newly developed low-noise amplifiers [104] which can be integrated with the PtE arrays. The FSCV experiments indicate that SiO_2-insulated Pt microelectrodes exhibit stable background currents and the catecholamine cyclic voltammograms are much sharper than those measured with CFEs. They are thus suitable for analytical electrochemistry in cell cultures and possibly in vivo [8], after fabrication of appropriately shaped Pt microelectrodes [105].

CHAPTER 5

RANDOM WALK SIMULATIONS FOR THE STUDY OF CATECHOLAMINE RELEASE AND DIFFUSION

5.1 Abstract

Electrochemical detector arrays were utilized in amperometric measurements of exocytotic catecholamine release from individual chromaffin vesicles. The signals measured by individual electrodes were compared with random walk simulations to obtain information about the spatiotemporal dynamics of single vesicle release. For an individual release event, different electrodes in the array detected different amperometric spike shapes corresponding to the same secretory event due to the different release site-electrode distances. A comparison between the measured and the simulated charges for the different electrodes revealed the positions of the release events. The time courses of catecholamine release from the vesicles and diffusion from the release site to the measuring electrodes were determined by simultaneously fitting the simulated time courses to the amperometric spikes measured by the individual electrodes. The results indicate that the time courses of catecholamine diffusion towards the electrodes were significantly slower than what would be expected for free catecholamine diffusion in an aqueous buffer. The slow diffusion rates were presumably due to reversible binding of catecholamines on the cell membrane, as indicated by random walk simulations incorporating such interactions with the cell surface.

5.2 Introduction

Neurotransmitter release by secretory vesicles, also known as exocytosis [2], is a fundamental biological process found in many cell types. Chromaffin cells of the adrenal gland constitute a widely used model system to study neuronal exocytosis. Chromaffin granules secrete high amounts of catecholamines, which can be electrochemically monitored with a carbon fiber electrode (CFE) [106, 24] using either amperometry or fast-scan cyclic voltammetry (FSCV) [94, 95].

Amperometric detection of individual exocytotic events using a CFE results in current spikes, which reflect the convolution of the time course of catecholamine release $R(t)$ with the time course of diffusion $D(t)$ from the release site to the CFE [75, 107, 25, 69, 24]. For a single CFE placed closely to the cell membrane and assuming instantaneous vesicular release, the catecholamine diffusion has been modeled as a one-dimensional random walk to produce an analytical solution for the time course of the measured amperometric spike [25]. However, measurements with variable cell-electrode distances indicated that release is not instantaneous [89], which may be due to slow dissociation of catecholamines from the granular matrix [69, 73], limited exposure of the granule matrix to the extracellular medium [75] or both. In measurements with a single CFE it is not possible to distinguish clearly the time course of release from the time course of diffusion because the distance between the release site and the recording electrode cannot be determined for individual events.

Microfabricated electrochemical detector (ECD) arrays overcome this limitation by simultaneous measurements with multiple electrodes that are located at different distances from the release site [41, 42]. Depending on their position

relative to the release site, the individual electrodes detect different fractions of the released molecules and the molecules reach the different electrodes with different diffusion time courses. Using a time-domain deconvolution of ECD array amperometric data, the true time course of catecholamine release from individual granules $R(t)$ and the time course of catecholamine diffusion $D(t)$ from the release site to the individual electrodes can be distinguished.

5.3 Materials and methods

5.3.1 Cell preparation and solutions

Bovine chromaffin cells were prepared as previously described [50]. The buffered solution used for all the amperometric and voltammetric measurements contained (in mM) 140 NaCl, 5 KCl, 5 $CaCl_2$, 1 $MgCl_2$, 10 HEPES/NaOH, 20 glucose (pH 7.3). Cells were stimulated using a glass micropipette containing (in mM): 45 NaCl, 100 KCl, 5 $CaCl_2$, 1 $MgCl_2$, 10 HEPES/NaOH, 20 glucose (pH 7.3).

5.3.2 ECD array microfabrication

The microfabrication process for the ECD arrays was as described [41]. Briefly, contact photolithography techniques were utilized to pattern platinum electrode arrays on glass coverslips, and insulate them with a thin ($\sim 500\ nm$) layer of photoresist. Four electrodes converged in a $\sim 10\ \mu m^2$ area, where the insulation free electrode tips were exposed forming the active detectors.

5.3.3 Carbon fiber electrode fabrication

Carbon fiber electrodes were fabricated as described [24]. Briefly, a single carbon fiber (~5 μm diameter) was inserted in a borosilicate glass capillary (1.8 mm outer diameter, Hilgenberg GmbH, Germany). The capillary was then pulled using a pipette puller (Model P-97, Sutter instrument) producing two electrodes, which were separated with scissors. CFE tips were dipped in melting wax (StickyWax, Kerr Corporation) for 2 min and subsequently cut using a blade (No 10, Feather Safety 55 Razor Co, Japan). Immediately prior to experiments, electrodes were backfilled with 3 M KCl solution and a chlorinated silver wire (Ag|AgCl) was inserted in the glass pipette to make a connection with the amplifier.

5.3.4 ECD array amperometry

Coverslips containing the ECD arrays were mounted on a custom built stage for a Zeiss 135TV microscope. Platinum electrodes were connected to the amplifiers via spring loaded gold contact pins and individual cells placed on the electrodes as described [41, 42]. Amperometry was performed with a four-channel amplifier (VA-10, NPI Electronic, Tamm, Germany). The measured current was low pass filtered at 500 Hz using the built-in analog low pass filter of the VA-10 amplifier. The electrodes were held at +700 mV versus a Ag|AgCl wire immersed into the bath solution. Amperometric data were digitized at 2 kHz sampling rate using a 16-bit resolution analog-to-digital (A/D) converter (BNC-2090, NIDAQ, National Instruments, Austin, TX, USA). Experiments were performed at room temperature the first day following chromaffin cell isolation.

5.3.5 CFE fast-scan cyclic voltammetry

Fast-scan cyclic voltammetry was performed using a CFE connected to an EPC-8 patch-clamp amplifier (HEKA-Elektronik, Germany). The corner frequency of the amplifier's built-in analog low pass filter was set to 5 kHz. The voltage waveform applied to the working CFE versus the reference Ag|AgCl wire consisted of a 5 ms triangular segment, during which the electrode voltage was scanned from -500 mV to +1,000 mV and back to -500 mV at a rate of ±600 V/s respectively. The triangular segment was followed by a 15 ms resting period during which the electrode potential was constant at -500 mV. Voltammetric currents were digitized at a rate of 50 kHz using a 16-bit A/D converter (ITC-18, Instrutech Corp, Bellmore, NY, USA). Experiments were performed at room temperature at day 1 following cell isolation.

5.3.6 Random walk simulations and data analysis

Random walk simulations were performed with custom written software in the Java programming language, using FORTE CE 3.0 for Java (Sun Microsystems, Santa Clara, CA). The fitting algorithms and the data analysis software were developed using Igor Pro (WaveMetrics Inc., Lake Oswego, OR, USA).

5.4 Results

5.4.1 Random walk simulations of ECD array amperometry

The ECD arrays utilized here consist of four surface-patterned Pt electrodes on a glass coverslip [41, 42]. For amperometric recordings, a single chromaffin cell is placed on top of the ECD array with a glass micropipette [41]. The placement procedure stimulates exocytotic activity in the cells presumably by inducing Ca^{2+} entry into the cells. Catecholamine molecules released from single vesicles diffuse in the narrow space between the cell surface and the ECD array, bouncing off the cell membrane and the glass coverslip. For this irregular geometry, there is no analytical solution for the diffusion equation, therefore the catecholamine diffusion was modeled as a random walk [43, 108].

For the random walk simulation (RWS) of diffusion from a specific site on the cell surface, the cell is modeled as a semi-infinite impermeable cylinder located Z_{CD} distance away from the ECD array plane, and its center $C(0,0,0)$ is taken as the origin of the coordinate system (Fig. 5.1A). The release location $(x_0, y_0, 0)$ on the cell surface, the number N of released catecholamines, the cell-detector vertical distance Z_{CD}, and the diffusion constant D are all user-defined parameters.

In the simulations, diffusion of each released molecule is tracked until one of the three following conditions is met: (i) the molecule touches an electrode surface, (ii) a user-defined time is elapsed from the beginning of the simulation, or (iii) the molecule has diffused more than 10 μm away from the cell center C. In case (i) the molecule is oxidized, while in cases (ii) and (iii) the molecule is

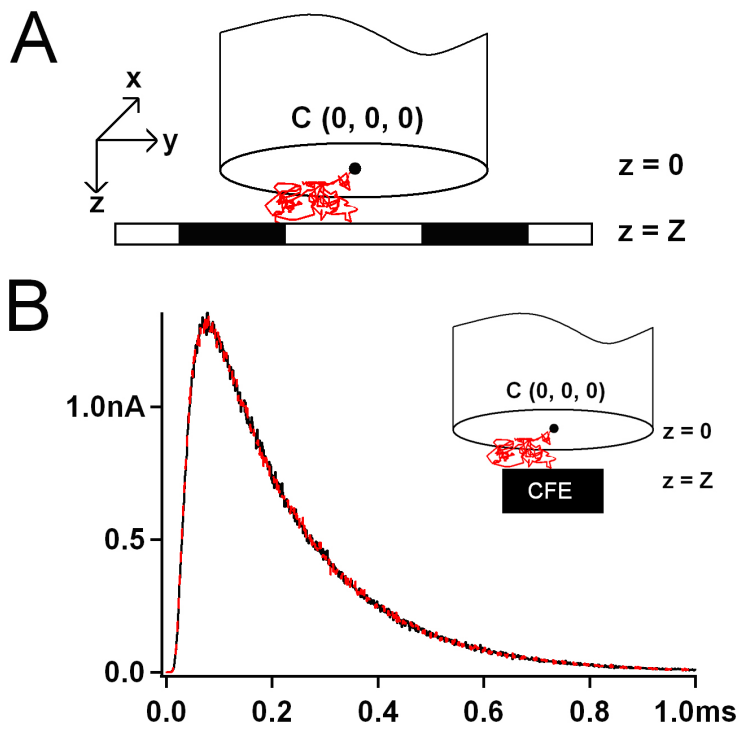

Figure 5.1: (A) Schematic of the geometry used for the RWS. The cell is modeled as an impermeable cylinder sitting on top of the ECD array coverslip (white) which contains the active electrodes (black). (B) RWS for $N = 1,000,000$ molecules released from the cell center located directly in front of a single 5x5 μm^2 electrode (shown in inset), with $D = 600\ \mu m^2/s$ and $Z_{CD} = 0.5\ \mu m$. Superimposed are the curves corresponding to the two methods described in the text: constant L (black curve), and variable L (red curve).

considered lost. When it encounters the glass coverslip a molecule is bounced off. The molecule is also bounced off the cell membrane. The red trace of Fig. 1A shows the random walk of a representative molecule released from the cell center, which bounces off from the coverslip (white) and gets oxidized at an electrode's surface (black).

The simulation time step Δt is a critical parameter for the RWS. Too large values of Δt produce inaccurate diffusion time courses, whereas too small values of Δt result in extremely long computation times. We have chosen to set the

simulation time step Δt equal to the largest power of 10 for which:

$$\Delta t \leq \frac{(sZ_{CD})^2}{6D} \tag{5.1}$$

where the scaling factor s was set equal to 0.3 for all the simulations, because smaller values did not improve the simulation results. The simulation time step Δt obtained from equation (5.1) satisfies the requirement to be small compared to the time necessary for molecules to diffuse across the cell-detector vertical distance Z_{CD}.

The average diffusion distance ΔL per time step Δt is given by the three-dimensional Einstein-Smolochowski equation:

$$\Delta L = \sqrt{6D\Delta t} \tag{5.2}$$

After each time step, a molecule located at (x, y, z) is assigned a new position $(x + \Delta x, y + \Delta y, z + \Delta z)$. Critical to the RWS are the diffusion steps $(\Delta x, \Delta y, \Delta z)$. These steps have a normal distribution [108]. To obtain three normally distributed random numbers with zero mean and variance $\sigma^2 = 2D\Delta t$, such that $\Delta L = \sqrt{\Delta x^2 + \Delta y^2 + \Delta z^2}$ satisfies equation (5.2) the polar form of the Box-Muller transform [109] was utilized. The resulting time course is shown in Fig. 5.1B (red trace). However, obtaining three normally distributed random numbers per time step and for each molecule requires a large amount of computational time.

An alternative approach that is computationally much faster is to choose a fixed value for ΔL given by equation (5.2) for each time step Δt and apply only a random direction to this step. A random number q uniformly distributed in the range $[-\Delta L, +\Delta L]$ determines the vertical distance Δz and thus the lateral distance: $\Delta x^2 + \Delta y^2 = \Delta L^2 - q^2$. A second random number ϕ uniformly distributed

in the range $[0, 2\pi]$ determines the azimuthal angle and thus the diffusion steps: Δx and Δy according to:

$$\Delta x = \sqrt{\Delta L^2 - \Delta z^2} cos\phi \tag{5.3}$$

$$\Delta y = \sqrt{\Delta L^2 - \Delta z^2} sin\phi \tag{5.4}$$

Thus, while the distance of movement per time step is fixed, the direction of movement is randomly distributed. This second approach is computationally fast, since for each molecule and at each time step, only two uniformly distributed random numbers are required. The resulting time course is shown in Fig. 5.1B (black curve), and is indistinguishable from the time course produced by the simulation method using normally distributed steps (red trace in Fig. 5.1B). Therefore, all subsequent simulations were performed assuming a constant ΔL per time step, since it is much faster than the method that requires a variable ΔL per time step.

5.4.2 Determination of release sites

Molecules released from a chromaffin granule diffuse isotropically in the extracellular space as indicated by fluorescence imaging [13]. When multiple electrodes are utilized to detect an individual release event, the charge measured by each electrode depends on the distance of the particular electrode from the release location. Fig. 5.2A shows the geometry of a four electrode array obtained from an atomic force microscope image. The superimposed light-gray dots form a two-dimensional 500 *nm* lattice of positions from which a large number of molecules were assumed to be instantaneously released by vesicles at the cell surface. Assuming instantaneous release, and for given values of the diffusion coefficient D and the cell-detector vertical distance Z_{CD}, the RWS for the different

release sites provide a unique oxidation current time course for each electrode (Fig. 5.2B), which depends on the lateral electrode-release site distance.

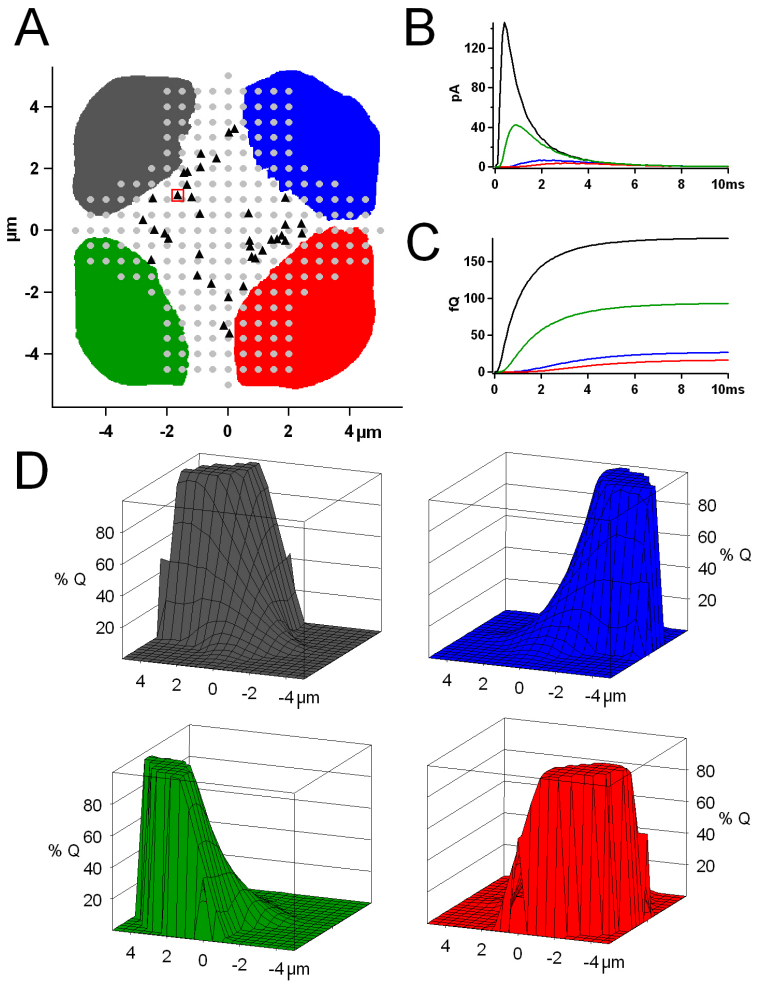

Figure 5.2: (A) AFM image of a four electrode array (electrodes are indicated by different colors). Superimposed is a 500 *nm* lattice of simulated release locations (gray dots) and the positions of measured exocytotic events interpolated from the RWS (black triangles). (B) RWS results from the location in the red square of panel (A) for $N = 1,000,000$ molecules, $z = 0.1\ \mu m$ and $D = 600\ \mu m^2/s$. Color coding as in panel (A). (C) Time courses of the integrated currents of panel (B). (D) Fractional charges measured by the four electrodes in (A) for RWS performed from each secretion site (gray dots in (A)). The largest fraction of molecules is detected by the electrode located nearest to the secretory event. When secretion occurs directly on top of one electrode, most molecules are detected by that electrode, while events occurring at the ECD center are equally detected by all the electrodes.

The integrated current time courses (charges) shown in Fig. 5.2C correspond to the number of molecules detected by each electrode. The fractional charges, which are the fractions of the total detected charge that are measured by the individual electrodes, depend primarily on the electrode-release site distances (Fig. 5.2D). Therefore the spatial location of exocytotic events can be determined from a comparison between the measured and simulated fractional charges, provided that amperometric currents are recorded by at least three electrodes.

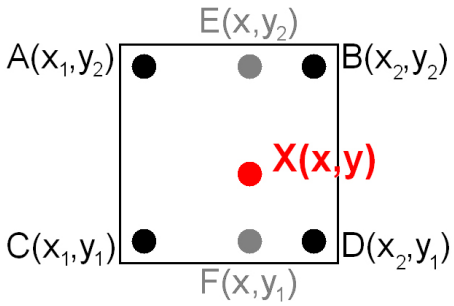

Figure 5.3: The four points (A, B, C, D) on the simulation lattice that form a square within which release occurred $X(x, y)$. Assuming the fractional charges depend linearly on the spatial distances the charge Q measured at the release location $X(x, y)$ is calculated taking into account the contribution to the fractional charges from both the horizontal and vertical distances.

One point on the simulation lattice will best satisfy the equation:

$$\sum_{k=1}^{n} (Q_{EXP,k} - Q_{SIM,k})^2 = min \tag{5.5}$$

where $Q_{EXP,k}$ and $Q_{SIM,k}$ are the experimental and simulated fractional charges measured by electrode k respectively, and n is the total number of electrodes in the ECD array. A release location $X(x, y)$ does not usually fall exactly on a point of the 500 nm lattice but somewhere in between four lattice points $A(x_1, y_2), B(x_2, y_2), C(x_1, y_1), D(x_2, y_1)$ (Fig. 5.3). Therefore the simulated fractional charges for arbitrary release locations were estimated by the following linear

interpolation (Fig. 5.3):

$$Q_{E,k}(x, y_2) = Q_{A,k} + \frac{x - x_1}{x_2 - x_1}(Q_{B,k} - Q_{A,k}) \tag{5.6}$$

$$Q_{F,k}(x, y_1) = Q_{C,k} + \frac{x - x_1}{x_2 - x_1}(Q_{D,k} - Q_{C,k}) \tag{5.7}$$

$$Q_{X,k}(x, y) = Q_{F,k} + \frac{y - y_1}{y_2 - y_1}(Q_{E,k} - Q_{F,k}) \tag{5.8}$$

where $(Q_{A,k}, Q_{B,k}, Q_{C,k}, Q_{D,k})$ are the fractional charges of electrode k returned by the RWS for the four locations (A, B, C, D) surrounding the actual release site (Fig. 5.3). The coordinates x, y are fitted such that the interpolated fractional charges $Q_{X,k}(x, y)$ satisfy equation (5.5). The grid point that satisfies equation (5.5) the best is used as the initial guess for the interpolation-based position fit. Fig. 5.2A shows the localization of 38 experimentally measured exocytotic events detected by at least three electrodes of the ECD array for one cell (black triangles).

5.4.3 Time course of amperometric currents

The RWS provides not only the fractional charges but also the time course of amperometric currents measured by the individual electrodes. To calculate numerically a low-noise time course of the diffusion $D_k(t)$ towards the individual electrodes $k = 1, .., 4$, a RWS was performed for 1,000,000 molecules for the actual release location. The simulated currents (Fig. 5.2B) assuming instantaneous release and a catecholamine diffusion coefficient $D = 600\ \mu m^2/s$ [110] show an amperometric spike half width of $t_{1/2} \sim 1\ ms$ for the closest electrode and increasing half width for the more distant electrodes as expected for the different diffusion times. However, the measured amperometric spikes for this location (Fig. 5.4, inset) are considerably slower with half widths of 11 to 30 ms for the

different electrodes. This is also evident from the time course of the running integrals of the amperometric spikes (compare Fig. 5.4 and Fig. 5.2C). This discrepancy is not unexpected because previous experiments suggested that the time course of amperometric spikes measured by a CFE at 1 μm distance from the cell membrane was inconsistent with free diffusion following instantaneous release [69] and several attempts have been made to deconvolve amperometric spikes and reveal the granule secretion kinetics [89, 71, 75, 107].

5.4.4 Vesicular release time course

In ECD array experiments the amperometric current $I_k(t)$ measured by electrode k is the convolution of the time course of catecholamine release $R(t)$ with the time course of diffusion $D_k(t)$ from the release site to electrode k:

$$I_k(t) = \int_0^t R(\tau) D_k(t-\tau) d\tau \tag{5.9}$$

Assuming the amperometric current is sampled once every Δt, the release time course $R(t)$ can be approximated by a series of instantaneous release events of n_i molecules, each occurring during the time interval $[t_i, t_i + \Delta t]$, where $i = [0, m-1]$ and m the total number of time points in each amperometric spike. Therefore, at each time point the flux of molecules out of the vesicle is $j_i = \frac{n_i}{\Delta t}$. Based on this approximation, the release time course becomes:

$$R(t) = \sum_{i=0}^{m-1} j_i \delta(t - t_i) \tag{5.10}$$

where $\delta(t)$ is Kronecker's delta function. Using equation (5.10) and approximating the convolution integral by a digital summation, equation (5.9) becomes:

$$I_k(t) = \sum_{i=0}^{m-1} 2 e_0 j_i D_k(t - t_i) \tag{5.11}$$

where the factor $2e_0$ accounts for the two electrons transferred per catecholamine molecule in amperometric detection. Thus, assuming a value for the diffusion constant D, the released amplitudes j_i representing the time course of release, can be determined as free fit parameters of a deconvolution spanning over all electrodes and time points. Equation (5.11) can also be used to fit the time course of the fractional charges detected by the individual electrodes (integrated currents normalized such that the total detected charge is 1) $Q_k(t)$ according to the equation:

$$Q_k(t) = \sum_{i=0}^{m-1} 2e_0 j_i S_k(t - t_i) \tag{5.12}$$

where $S_k(t)$ are the integrated diffusion time courses $D_k(t)$.

Fig. 5.4 shows the results of fitting equation (5.11) and (5.12) to the currents (inset) and normalized charges of an exocytotic event measured by the ECD array of Fig. 5.2. The diffusion time courses $D_k(t)$ were obtained from the RWS using $D = 600\ \mu m^2/s$ and numerically integrated to provide $S_k(t)$. The fitted traces (dashed) are in good agreement with the measured data (solid) for the two nearby electrodes (black, green traces). The fitted time course for the two distant electrodes, however, is much faster than the measured signals (blue, red traces) suggesting that diffusion along the cell surface is significantly slower than assumed in the simulation.

In order to improve the fits, the diffusion coefficient D was allowed to vary as a free fit parameter in equation (5.11). Fig. 5.5A shows RWS results for $D = 600\ \mu m^2/s$ (red) and $D = 60\ \mu m^2/s$ (black), with $N = 100,000$ molecules for a single 5x5 μm^2 electrode at $1\mu m$ distance from the cell surface. When the curves are scaled according to the diffusion coefficient ratio (Fig. 5.5B), the shapes of the two curves are indistinguishable. Therefore, knowledge of the diffusion time

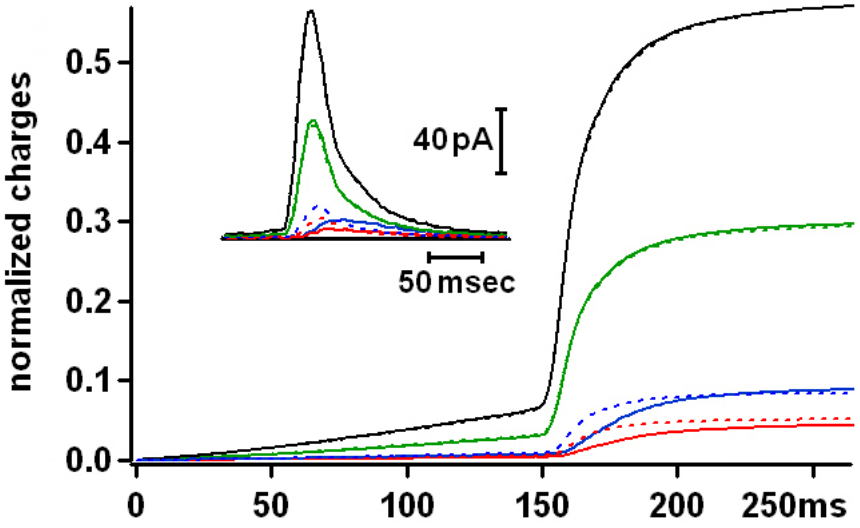

Figure 5.4: Experimental (solid lines) and fitted (dashed lines) amperometric currents (inset) and their integrals (normalized such that total charge is 1 arbitrary unit). The fits were performed using the RWS results for $D = 600\ \mu m^2/s$, $z = 0.1\ \mu m$ and $N = 1,000,000$ molecules.

course $D_k(t)$ for one value of D provides the diffusion time course $D_k(t)$ for any other value of D (Fig. 5.5B) by corresponding scaling, facilitating treatment of the diffusion coefficient as a free fit parameter along with the time course of release in equations (5.11) or (5.12).

Fig. 5.6A shows the results of fitting equation (5.11) and (5.12) to the same data as in Fig. 5.4, but with the diffusion coefficient a free fit parameter. The fits of Fig. 5.6A are markedly improved over those of Fig. 5.4 (for $D = 600\ \mu m^2/s$). The deconvolution method returned $D = 110\ \mu m^2/s$, which is ~18% of the value in free solution. For seven events from two different cells the best fits were obtained with diffusion coefficients in the range 80 - 130 $\mu m^2/s$. Thus, the apparent diffusion coefficient near the cell surface is ~6 times slower than that for free diffusion. The simultaneous measurement with multiple electrodes at different distances separates for an individual event the time course of diffusion

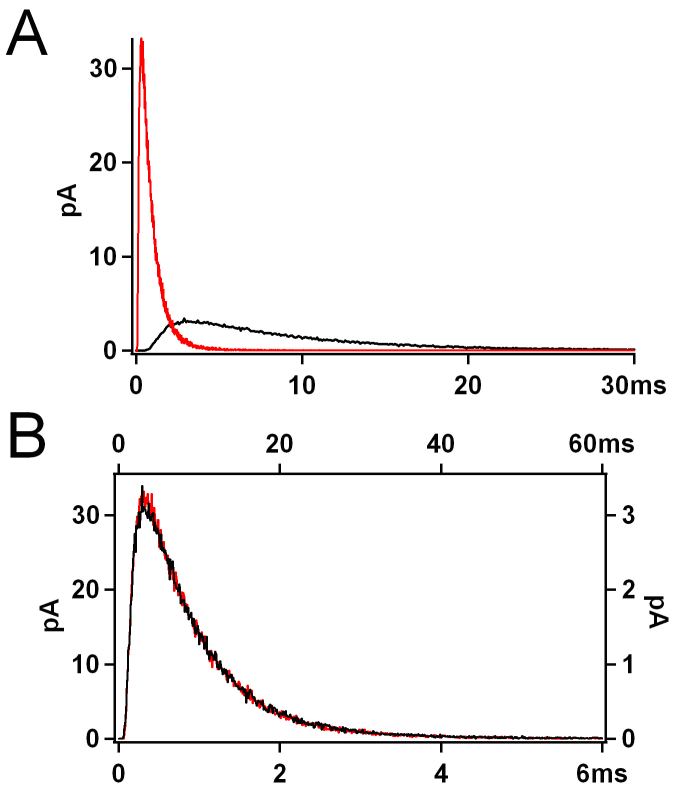

Figure 5.5: (A) RWS for release occurring from the cell center directly in front of a single 5x5 μm^2 electrode using two different values for the diffusion constant: $D = 600\ \mu m^2/s$ (red) and $D = 60\ \mu m^2/s$ (black). For both cases $N = 1,000,000$ molecules and $z = 1\mu m$. (B) The two RWS time courses of (A) are plotted on different scales based on the diffusion constant ratio (left and bottom: $D = 600\ \mu m^2/s$, right and top: $D = 60\ \mu m^2/s$). Color coding is the same for both panels.

from the time course of release. The time course of release for this event of Fig. 5.6A is shown in Fig. 5.6B with a half width $t_{1/2}$ ~11 ms.

The lower diffusion coefficient may be due to reversible binding of catecholamines onto the cell surface. To simulate such interactions with the cell surface, the RWS was modified such that upon contact with the cell surface, catecholamine molecules were not bounced away, but were kept bound to the cell surface for a constant time b_T and then released (transient binding). Fig. 5.7 shows the results of the RWS (not the fits to the data) using $D = 110 \mu m^2/s$ with

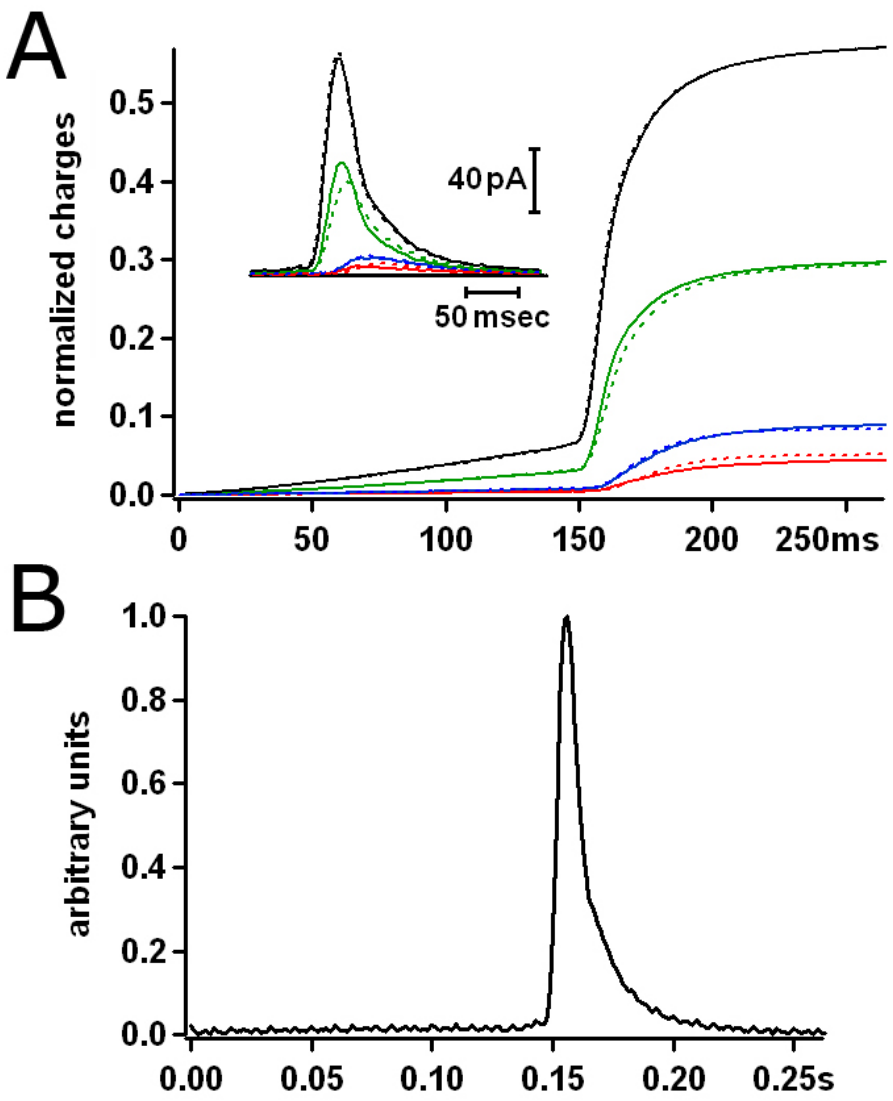

Figure 5.6: (A) Experimental (solid lines) and fitted (dashed lines) amperometric currents (inset) and their integrals (normalized such that total charge is 1 arbitrary unit). The fits were performed using the RWS results for $z = 0.1\ \mu m$ and $N = 1,000,000$ molecules. The diffusion coefficient was one of the free fit parameters. The best fit was obtained for $D = 110\ \mu m^2/s$. (B) Time course of catecholamine release from a chromaffin granule revealed by the time-domain deconvolution method for $D = 600\ \mu m^2/s$. The half-width of the release time course was ~11 ms.

$b_T = 0\,\mu s$ (solid lines) and $D = 600\,\mu m^2/s$ with $b_T = 5.0\,\mu s$ (dashed lines), demonstrating that reversible binding is consistent with the apparent slow diffusion. It should be noted that the numerical value of b_T depends on the time step used

in the RWS and on the cell-ECD distance assumed in the RWS. When the RWS included binding, the diffusing catecholamine molecules were bound to the cell membrane on average 70% of their total simulation time. Thus the average ratio of the concentration of free catecholamine molecules $[F]$ over the concentration of bound molecules $[B]$ during the simulation time course is $[F]/[B] = 0.43$.

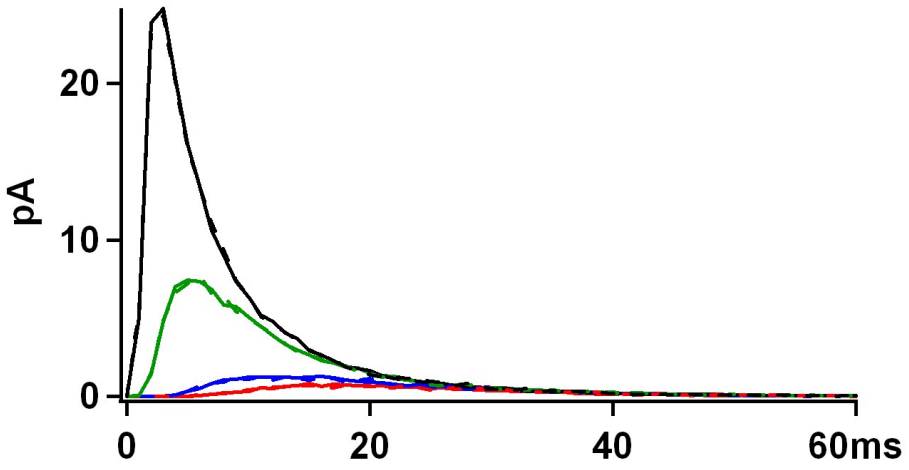

Figure 5.7: A comparison of the RWS results for $D = 110\ \mu m^2/s$ with $b_T = 0\ \mu s$ (solid lines) and $D = 600\ \mu m^2/s$ with $b_T = 5.0\ \mu s$ (dashed lines). For both RWS $z = 0.1\ \mu m$ and $N = 1,000,000$ molecules. Color coding same as in Fig. 5.6.

To test whether amperometric spikes recorded by CFEs are also affected by a slow diffusion time course, RWS was performed for a single 5x5 μm^2 electrode located at 100 nm distance from the cell surface assuming an instantaneous release event. Two simulations were performed, one for $D = 110\ \mu m^2/s$ without binding and one for $D = 600\ \mu m^2/s$ with $b_T = 5.0\ \mu s$. The $t_{1/2}$ of the resulting time courses for both conditions are shorter than 100 μs (Fig. 5.8), indicating that an apparent diffusion ~6-fold slower than that in free aqueous buffer would not affect CFE amperometric spikes, which have an average $t_{1/2} \sim 10ms$ [24].

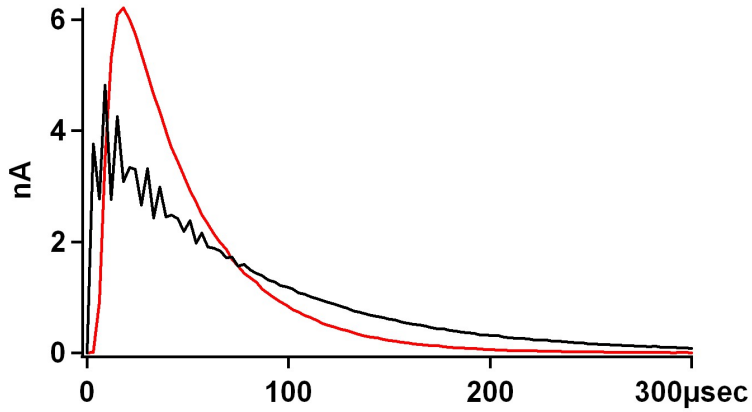

Figure 5.8: RWS for release occurring from the cell center directly in front of a single 5x5 μm^2 electrode. $D = 110\ \mu m^2/s$ with $b_T = 0\ \mu s$ (red trace) and $D = 600\ \mu m^2/s$ with $b_T = 5.0\ \mu s$ (black trace). For both cases $z = 0.1\ \mu m$ and $N = 1,000,000$ molecules.

5.4.5 RWS for FSCV measurements

When a CFE is operating in FSCV mode, the molecules in contact with the electrode surface are oxidized and subsequently reduced such that they are not consumed. The FSCV signal that results form release of a particular vesicle thus decays only due to the diffusion of the molecules out of the space between the cell surface and the CFE. In the case of FSCV simulations, the CFE surface was thus modeled as a reflecting plane, such that upon contact with it catecholamine molecules were bounced back. In FSCV experiments the CFE is usually gently pressed against the cell membrane such that a very small gap is created between the cell and the electrode surfaces, therefore the cell-CFE distance was assumed to be $z = 0.1 \mu m$.

While the exact spatial location of individual exocytotic events is unknown, it is safe to assume that exocytotic events occurring outside the membrane area facing the CFE are unlikely to be detected since most of the catecholamine

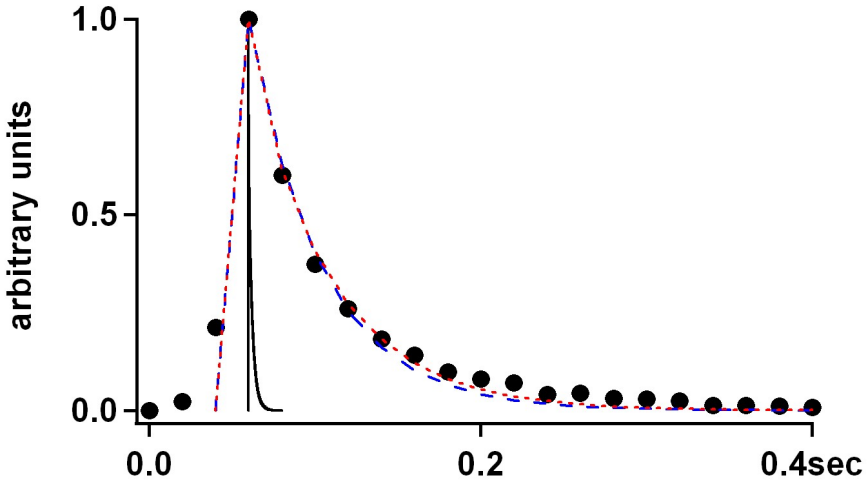

Figure 5.9: Averaged FSCV spike from 7 chromaffin cells. Data (dots) are presented as mean of n=104 spikes. Superimposed are the averaged RWS spikes for $D = 600\ \mu m^2/s$ with $b_T = 0\ \mu s$ (solid black trace), $D = 30\ \mu m^2/s$ with $b_T = 0\ \mu s$ (dashed blue trace), and $D = 600\ \mu m^2/s$ with $b_T = 20\ \mu s$ (dashed red trace). $N = 100,000$ molecules and $z = 0.1\ \mu m$ for all the RWS.

molecules will not be able to diffuse into the narrow gap. Secretory events within the 2.5 μm radius area of the cell surface facing the CFE are likely to be uniformly distributed. To obtain representative simulations for various locations within this area, RWS was performed for five secretion sites located at the CFE center and at a distance r of 0.5 μm, 1 μm, 1.5 μm, and 2.0 μm from the center. These five simulated time courses were averaged with a weight equal to their squared radii (measured from the cell center) to account for the relative cell surface area with that radius. The resulting averaged curve provides the average time course of FSCV signals in the recording. Fig. 5.9 shows the average time course of measured FSCV spikes from 7 chromaffin cells (filled symbols) with $t_{1/2} \sim 45ms$. The RWS time course for a CFE in FSCV mode for the standard diffusion constant $D = 600\mu m^2/s$ (solid black trace) gives a half-width of $t_{1/2} \sim 2ms$, inconsistent with the measurement. However, good agreement between the ex-

perimental data and the simulation is obtained for RWS assuming $D = 30\mu m^2/s$ with $b_T = 0\ \mu s$ (dashed blue trace) or assuming $D = 600\mu m^2/s$ with $b_T = 20\ \mu s$ (dashed red trace), consistent with a reduced apparent diffusion coefficient due to diffusion with binding. For $z = 0.1\ \mu m$, the binding time $b_T = 20\ \mu s$ resulted in a $[F]/[B] = 0.1$ averaged for all the molecules, indicating that on average catecholamine molecules were bound to the cell membrane 90% of the simulation time.

5.5 Discussion

The novel techniques presented in this work allowed the continuous monitoring of the spatiotemporal dynamics of chromaffin vesicle release. For this purpose, ECD arrays were utilized in amperometric measurements of catecholamine release from chromaffin cell vesicles. The experimental data were compared with RWS modeling catecholamine diffusion in the narrow gap formed between the cell membrane and the ECD array coverslip.

The location of transmitter release events was identified with high spatial precision by comparing the fractional charges measured by the individual electrodes of the ECD array with the number of molecules detected by each electrode in the RWS. For the identified release sites, RWS was performed to obtain temporal information about the time course of catecholamine release from single chromaffin vesicles and the time course of catecholamine diffusion from the release site to the individual electrodes of ECD arrays. Good agreement between the RWS and the measured amperometric data was obtained for values of the diffusion constant in the range 80-130 $\mu m^2/s$, which is ~6-fold lower

than what would be expected for catecholamines diffusing freely in an aqueous buffer. The corresponding time course of catecholamine release from the vesicles was in the range 5-8 *ms*, which is an overestimate due to the low pass filtering of the amperometric currents.

The lower values of the diffusion constant determined from the deconvolutions indicate hindered catecholamine motion, which may be due to cell surface tortuosity [111] which would increase the effective length that catecholamines have to diffuse to reach the electrodes. Alternatively, proteins and peptides extruded into the extracellular space along with the catecholamines may increase the viscosity of the solution near the release location and thus reduce the motion of the diffusing catecholamines.

Yet another possibility is that the slow diffusion time courses are determined by reversible binding of catecholamine molecules onto the cell membrane. Such surface interactions were taken into account in the RWS and the resulting diffusion time courses were consistent with the time courses of the measured amperometric currents, indicating that reversible binding of catecholamines onto the cell surface affects the time course of amperometric spikes measured by ECD arrays. To test if reversible binding also affects the amperometric spikes measured by CFEs, RWS was performed for release occurring directly in front of a single electrode. The ~6-fold lower apparent diffusion coefficient was used in the RWS and the resulting diffusion time course had a very short half-width compared to the typical CFE amperometric spike half-width. Therefore the time course of CFE amperometric spikes is determined by the time course of granular release and not the diffusion from the release site towards the CFE.

Unlike in amperometry where catecholamines are immediately oxidized at

the electrode surface, in FSCV catecholamine molecules are reversibly oxidized to their quinone form, which is then reduced back to the original catecholamine. Therefore, the falling phase of a FSCV spike indicates the time course of diffusion of catecholamines away from the detector surface. To investigate the time course of FSCV spikes, RWS was also performed for a CFE operating in FSCV mode. The simulations were compared with CFE FSCV data from chromaffin cells. The falling phase of the RWS was much faster than the measured data when the standard value of the diffusion constant was used. The RWS time course was consistent with the FSCV data when a low value of the diffusion constant was used or when reversible binding of catecholamines was taken into account in the RWS.

The apparent diffusion constant which reproduced the FSCV data is ~4x lower than that which reproduced the ECD amperometric spikes. Similarly, the binding time which reproduced the FSCV data is 4x longer than that which reproduced the ECD amperometric data. These differences are presumably due to catecholamine adsorption onto the CFE surface, which would only be detected in the FSCV experiments [112, 113] and would lower the apparent diffusion constant of catecholamines even more than reversible binding alone. The difference could also be due to smaller cell-detector distance in CFE compared to ECD array measurements that would result in more frequent binding events at the cell surface. In either case, reversible binding of catecholamines to binding sites on the cell surface may have a physiological role, which has yet to be illuminated.

The RWS and the time-domain deconvolutions presented in the current study could easily be adapted for arbitrary electrode geometries and thus find

use in modeling transmitter release under various conditions. The dynamics of single vesicle release can thus be investigated with unprecedented spatiotemporal resolution.

CHAPTER 6

IN VIVO MEASUREMENTS OF TRANSMITTER RELEASE

6.1 Abstract

Dopamine release in the brain of freely moving research animals was monitored with fast-scan cyclic voltammetry using carbon fiber electrodes implanted in the striatum of the animals. Exocytotic release was elicited by a stimulating current pulse train, using a pair of electrodes stereotaxically implanted in the medial forebrain bundle of the animals. The animals showed complete recovery from the stereotaxic surgery and the electrochemical measurements. To enhance animal mobility during the experiments an electronic device with the potential of wirelessly transmitting *in vivo* electrochemical data is being developed.

6.2 Introduction

Studies of exocytosis in single cells aim at understanding cellular function and have revealed many key properties of biological cells. Despite the great wealth of information obtained from measurements of exocytotic release in single cell, the behavioral properties of living organisms are defined by the function of a large number of cells, typically located within the same organ. Hence, investigating transmitter release in an intact organ in a behaving animal would ultimately correlate exocytosis with behavior.

The first attempts to electrochemically measure transmitter release *in vivo* were made in 1978 by Wightman and coworkers [114] and soon after in 1981 by

Gonon and coworkers [101]. However both these attempts were performed in anesthetized animals. Therefore it was not possible to correlate neurotransmitter action with animal behavior. Measurement of neurotransmitter secretion in the brain of freely moving research animals was first achieved in 1997 by Garris and Wightman [8]. These measurements revealed the role of the neurotransmitter dopamine (DA) in various behavioral tasks, such as drug seeking [115] and sexual behavior [116].

Stereotaxic surgery was performed for the implantation of electrodes in the brain of rats, as well as an electronic setup for the measurement of *in vivo* release of DA. The surgical procedure and the setup share many similarities with those developed in the lab of Prof. R.M. Wightman, where the author has been trained. There are, however, some modifications (see below). At the end of this chapter we introduce a novel electronic device, which has the capability of transmitting electrochemical data in a wireless fashion.

6.3 Materials and methods

6.3.1 Reagents and solutions

The buffered solution used for all the *in vitro* voltammetric measurements contained (in *mM*) 140 NaCl, 5 KCl, 5 $CaCl_2$, 1 $MgCl_2$, 10 HEPES/NaOH, 20 glucose (pH 7.3). Dopamine hydrochloride was purchased from Sigma (Milwaukee, WI) and used without further purification.

6.3.2 Stereotaxic surgery

Prior to the surgery all surgical instruments were sterilized by steam sterilization. Adult Sprague-Dawley rats were housed and cared for in accordance to the guide for care and use of laboratory animals (NIH Publication 86-23). The surgical procedure was approved by the Institutional Animal Care and Use Committee of Cornell University (protocol number: 2005-0164).

On the day of the surgery, a rat was transferred to the procedure room and immediately anesthetized with an intramuscular dosage of 87.5 mg/kg Ketamine and 12.5 mg/kg Xylazine. Throughout the surgical procedure, the depth of anesthesia was monitored by palpebral reflex (response to foot pinch) every 5-10 min, and additional doses of anesthetic (half the induction volume) were administered intraperitoneally as necessary to maintain a sufficient level of anesthesia without overdose.

The fur from the dorsal skull was shaved with an electric clipper, and the animal immobilized in a Model 963 Ultra-precise small-animal stereotaxic frame (David Kopf Instruments, Tujunga, CA). The scalp was prepped with 70% alcohol rinse and iodine scrub. Following induction of local anesthesia at the periosteum with 2 mg/kg bupivicain, an incision was made to the level of the skull using scissors and the scalp was retracted with tweezers. The incision area was cleaned with hydrogen peroxide.

Lambda and bregma were adjusted, such that they were completely flat, as measured by the stereotaxic instrument. Target coordinates were determined based upon distance from Bregma as measured using the stereotaxic instrument and an operating microscope (Omano, Wirtz, VA). Coordinates were derived

from the Paxinos and Watson rat brain atlas [117] and are presented in units of millimeters (*mm*).

Three burr hole sites were marked, one for the working electrode at anterior-posterior (AP): +1.20 and medio-lateral (ML): +2.00, and two for the stimulating electrodes at AP: -4.56, ML: +1.40, and AP: -4.56, ML: +2.40. Five additional burr hole sites were marked, four for the surgical screws to mount the cement on the animal's head, and one for the reference electrode (on the side contralateral to the stimulating and working electrodes).

Burr holes were made through the skull with a high speed drill (Model 395 MultiPro, Dremel, Racine, WI), with care taken not to violate the dura. At the sites of the stimulating electrodes, dural incisions were made by nicking the dura with the sharp edge of a 30G needle. Any dural bleeding was controlled by filling the burr hole with hypertonic saline (7.5% NaCl in distilled water) and observing for a brief period. Typically dural bleedings stopped after a short period, with insignificant blood loss.

Four stainless steel surgical mounting screws (part number: 0-80 X 1/8, Plastics One, Roanoke, VA) were half way tightened in the burr holes using a screwdriver. A guide cannula (part number: MD-2251, Bioanalytical Systems, West Lafayette, IN) was mounted on the stereotaxic frame holder (rod part number: MD-1521, clamp part number: MD-1520, Bioanalytical Systems, West Lafayette, IN) and inserted in the burr hole located at AP: +1.20, ML: +2.00. A bare silver wire of length ~1.5 *cm* and thickness 200 μm (part number: 782000, A-M Systems, Sequim, WA) was chlorinated (Ag|AgCl), soldered to a gold pin (part number: 82K7797, Newark, Chicago, IL) and inserted at the site of the reference electrode. The four surgical screws, the cannula and the reference electrode

were mounted on the animal's head using dental cement (part number: 675570, DentSply Caulk, Milford, DE). After the cement had solidified (typically within 5-10 *min*) the guide cannula was detached from the stereotaxic frame holder, and the holder was retracted.

The dual stimulating electrodes (250 μm diameter stainless steel wires, insulated with polyimide except their tips, part number: MS303/1, Plastics One) were mounted on the stereotaxic frame and inserted 8 *mm* in the brain. The depth was measured using the stereotaxic frame and the operating microscope. The stimulating electrodes were connected to an optically isolated current stimulator (Model 2200, A-M Systems) and a bipolar current pulse train (24 pulses, 4 ms duration per pulse, 100 μA amplitude, 60 Hz frequency) was applied to the electrodes. The stimulating electrodes were further lowered in the brain at 0.2 *mm* increments, until the animal's response to the stimulating current pulse train was minimized. Typically, this occurred at 8.5-9.0 *mm* dorso-ventral (DV) depth. Dental cement was added onto the electrodes and when the cement had solidified, the stereotaxic frame's arm was retracted. Fig. 6.1 shows a pair of stimulating electrodes in the AP section of the brain where the electrodes were implanted.

The animal was removed from the stereotaxic frame, 1mL lactated ringer solution and 2 mg/kg Yohimbine were administered intraperitoneally, and the animal was transferred to its cage and allowed to recover. Body temperature was maintained at appropriate levels using a lamp. After waking up, the animal was returned to the housing facility, singly housed to avoid destruction of the surgical site by other animals, and allowed to recover for at least 3 days. Food and water were available *ad libitum*. For days 1 and 2 following surgery, the

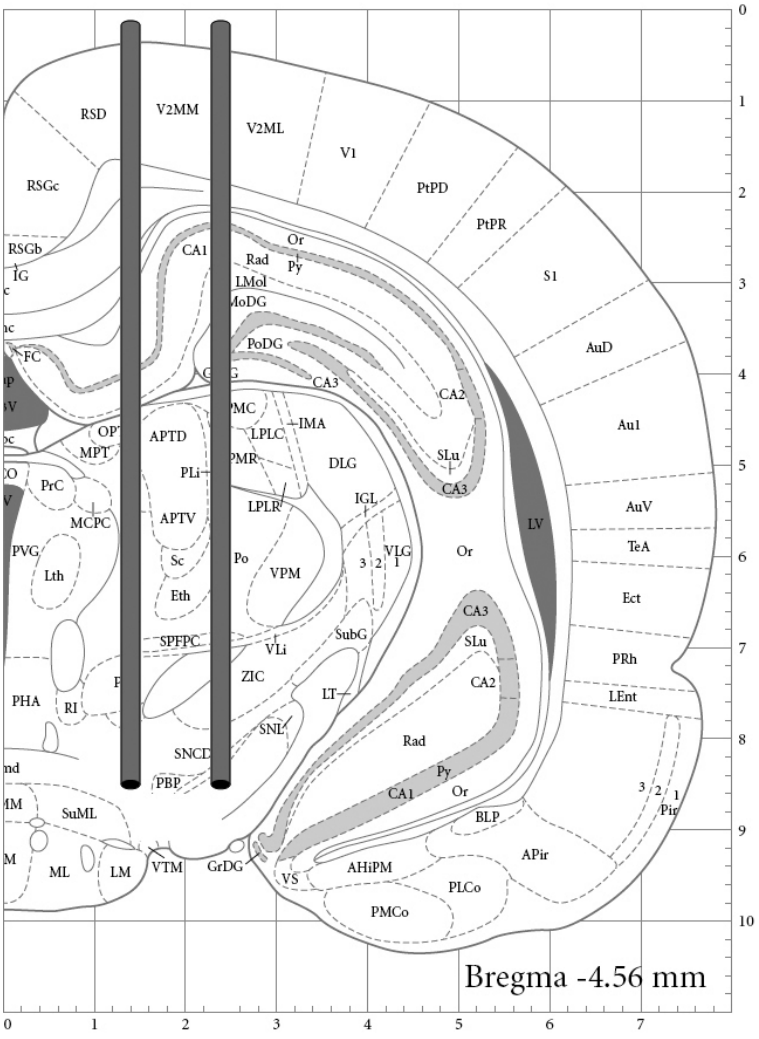

Figure 6.1: A pair of stimulating electrodes in the medial forebrain bundle. Gray: polyimide insulation, black: exposed stainless steel electrodes. Only the right cerebral hemisphere is shown. Schematic not drawn to scale. Figure modified from [117].

animal was administered 2 mg/kg Ketoprofen. If the animal had not regained its pre-surgery weight, 1 mL lactated Ringer solution was also administered daily. Both Ketoprofen and the Ringer solution were administered intraperitoneally.

6.3.3 Carbon fiber electrode fabrication

Carbon fiber electrodes (CFEs) were fabricated by inserting a single carbon fiber (5.0 μm diameter) in a borosilicate glass capillary (0.6 mm outer diameter, part number: 624503, A-M Systems). The capillary was then pulled using a pipette puller (Model P-97, Sutter instrument) producing two electrodes, which were separated with scissors. CFE tips were cut using a blade (No 10, Feather Safety 55 Razor Co, Japan) such that the protruding cylindrical electrodes were ~75-100 μm long. Immediately prior to experiments, a silver wire coated with silver paint was inserted in the glass capillary to connect the CFE to the amplifier.

6.3.4 Manipulator for inserting the CFE in the brain

During recordings a glass-encased CFE was lowered through the guide cannula into the animal's brain. For this purpose, a custom built (machine shop, School of Applied and Engineering Physics, Cornell University, Ithaca, NY) manipulator (Fig. 6.2) was utilized.

To avoid breaking its tip, the top part of the CFE was inserted in the manipulator from the part where the male-end connector to the guide cannula is located (see bottom of Fig. 6.2). The manipulator was then mounted onto the guide cannula implanted in the animal's head. The precision screw of the manipulator allows the precise control of the DV position of the CFE. A black foam (shown at the top of Fig. 6.2) prevents the CFE from sliding in the manipulator chamber. The lock secures the precision screw such that the DV position of the CFE is fixed. A schematic of a CFE in the striatum is shown in Fig. 6.3. The original design and fabrication of this manipulator was developed at the lab

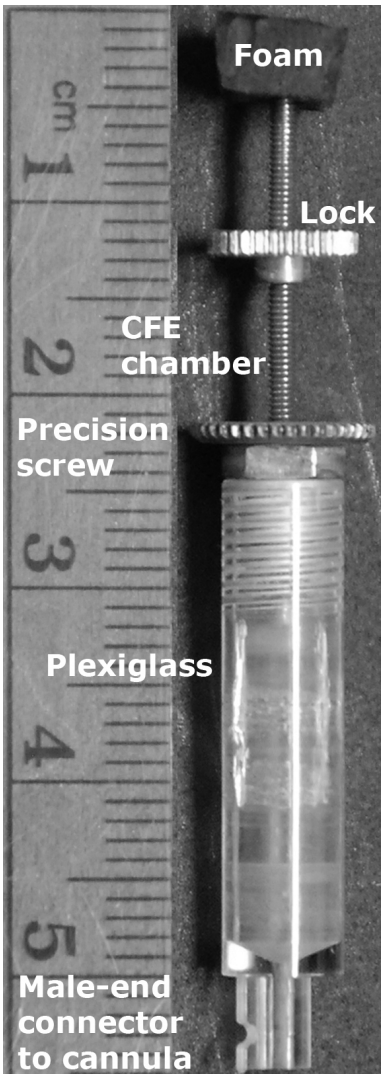

Figure 6.2: Manipulator for inserting the CFE in the animal's brain. The manipulator can be mounted and locked on the guide cannula. A precision screw (82 threads per inch, resulting in a vertical movement of ~310 μm per full turn) adjusts the CFE dorso-ventral position. Photo: courtesy of O.D. Escanilla.

of Prof. R.M. Wightman in the Department of Chemistry at the University of North Carolina at Chapel Hill.

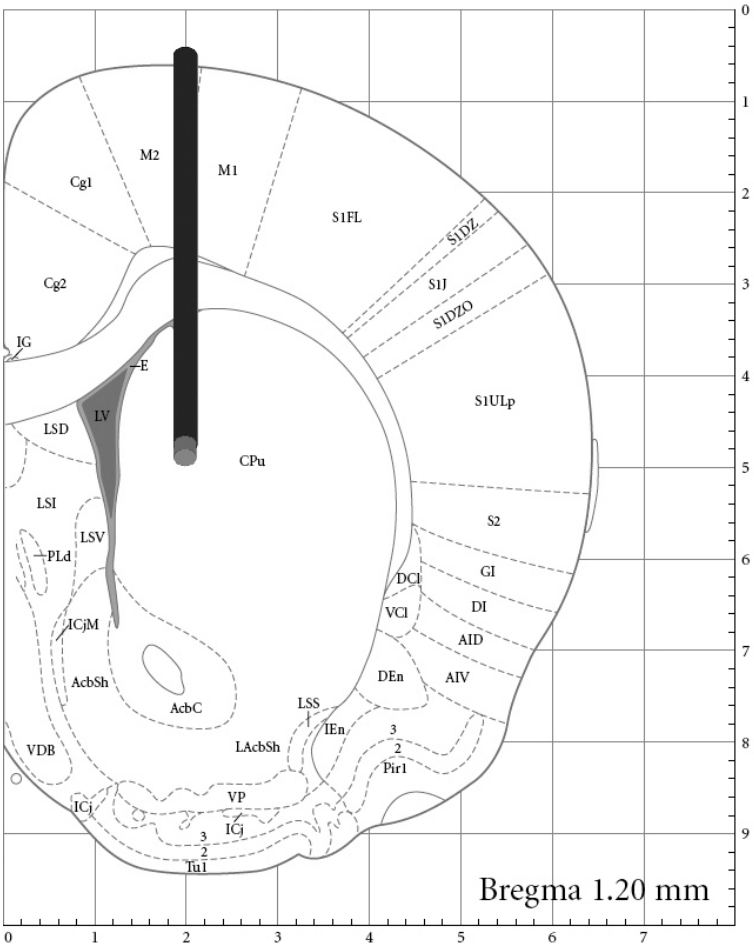

Figure 6.3: A CFE in the caudete putamen. Black: glass pipette, gray: protruding carbon fiber. Only the right cerebral hemisphere is shown. The guide cannula through which the CFE is lowered in the brain is not shown. Schematic not drawn to scale. Figure modified from [117].

6.3.5 Data detection and amplification apparatus

The CFE was connected via a gold contact pin to the negative input terminal of a low noise amplifier (OPA111AM, Texas Instruments, Dallas, TX), soldered onto a custom built circuit board. Fig. 6.4 shows the circuit design. The low noise amplifier was configured with negative feedback (R_f in parallel with C_f) creating a low-pass filter of ~6.4 kHz cutoff frequency. The CFE voltammetric

current was converted to a voltage through the feedback resistor. To subtract the applied potential a differential amplifier (OP27G, Texas Instruments) was used with 10 $k\Omega$ input and feedback resistors. Four capacitors were used to reduce the power supply voltage noise (lower left of Fig. 6.4).

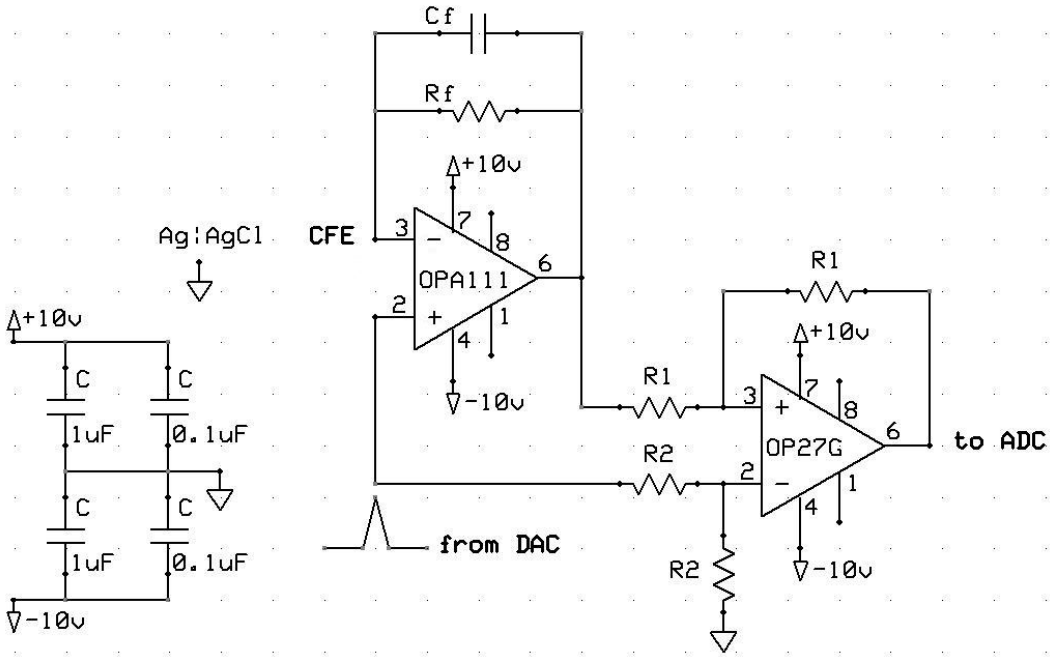

Figure 6.4: Electronic circuit for *in vivo* measurements. Values of passive components: $R_f = 5M\Omega$, $C_f = 5pF$, $R_1 = R_2 = 10k\Omega$.

6.3.6 Data acquisition hardware and software

The electronic circuit of Fig. 6.4 was interfaced with a personal computer using a commercially available data acquisition setup (Heien Instruments, Normal, IN) which utilized two PCI boards (PCI-6711 and PCI-6052 both by National Instruments). The software Tar Heel CV (Heien Instruments) was utilized to apply the potential waveform to the CFE, digitize the CFE current, apply the stimulating pulse train to the bipolar stimulating electrodes, and generate all

the necessary control signals.

6.3.7 Fast-scan cyclic voltammetry

Fast-scan cyclic voltammetry (FSCV) was performed using a voltage waveform applied to the working CFE versus the reference Ag|AgCl wire that consisted of a 9.3 ms triangular segment, during which the electrode voltage was scanned from -400 mV to +1,300 mV and back to -400 mV at a rate of ±400 V/s respectively. The peak potential of this waveform was extended to +1,300 mV because overoxidation of CFEs enhances DA detection [97]. The triangular segment was followed by a resting period during which the electrode potential was constant at -400 mV (Fig. 6.5). The total duration of the applied potential was 100 ms. Voltammetric currents were digitized at ~117 kHz sampling rate. Experiments were performed at room temperature.

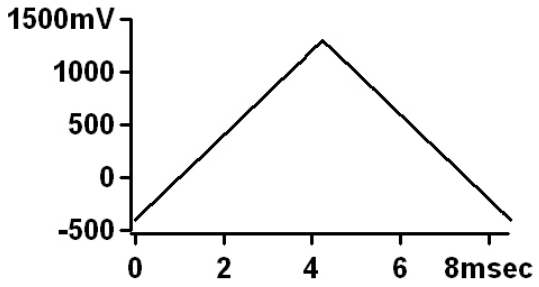

Figure 6.5: Potential waveform applied to the CFE during *in vivo* measurements.

6.4 Results

6.4.1 *In vivo* recordings with wired setup

On the day of the experiments, the animal was brought from the animal housing facility and placed in a plexiglass box located inside a Faraday cage to perform low-noise *in vivo* electrochemical measurements. A CFE was placed in the manipulator (Fig. 6.2) and carefully inserted in the animal's striatum. The implanted bipolar stimulating electrodes were connected to a current stimulator. The voltage waveform shown in Fig. 6.5 was repetitively applied to the CFE.

Fig. 6.6 shows the CFE current sampled at the +522 mV point of the anodic ramp (positive slope). At t=5 s, dopaminergic neurons were stimulated by a bipolar current pulse train (24 pulses of amplitude 100 μA, duration 4 ms and frequency 60 Hz). The transient increase in the oxidation current is correlated with the onset of the stimulating pulse train, the duration of which is indicated by the two gray squares in Fig. 6.6.

The current responses during the first 50 voltammetric cycles (0 - 4.9 s) was averaged to obtain the background current. The following 10 cycles (5-5.9 s) were averaged providing an average background+redox signal. Their difference (redox current) plotted versus the applied potential is shown in Fig. 6.7 and reveals the signature voltammogram of DA molecules. Fig. 6.8 shows the background-subtracted voltammogram for the sweep of the peak oxidation current, which occurred at t=5.5 s (the background current was the same as in Fig. 6.7). The voltammogram of Fig. 6.8 indicates that the oxidation current was due to increased DA levels in the vicinity of the CFE.

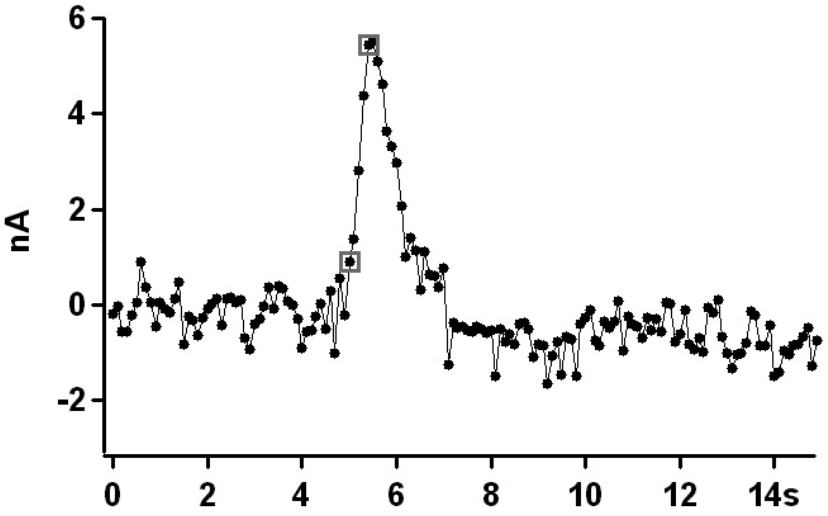

Figure 6.6: *In vivo* recording of CFE current sampled at the +522 mV applied potential and plotted versus time. The two gray squares indicate the duration of the stimulating pulses (24 bipolar pulses, at 60 Hz frequency and with 100 μA amplitude).

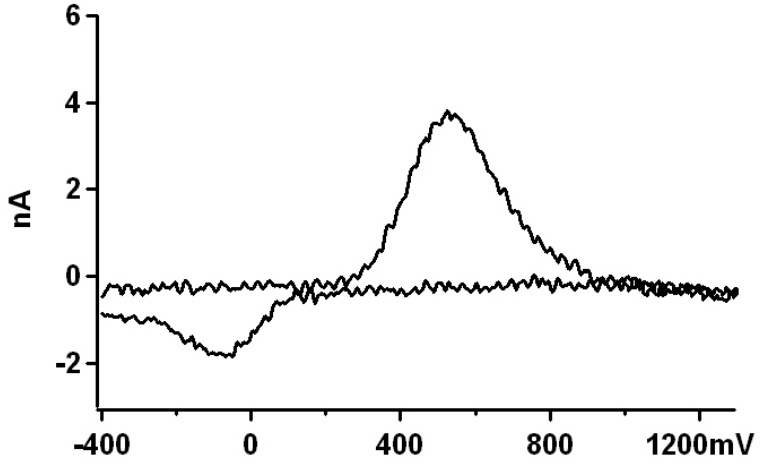

Figure 6.7: The current of the first 50 (0-4.9 s) voltammetric cycles of Fig. 6.6 was averaged to determine the background signal. The following 10 cycles (5-5.9 s) were averaged to obtain the average background+redox signal. Their difference plotted versus the applied potential is the background-subtracted voltammogram.

Figs. 6.9 and 6.10 are similar to Figs. 6.6 and 6.7 respectively, with the difference that the amplitude of the stimulating pulses was increased from 100 to 300

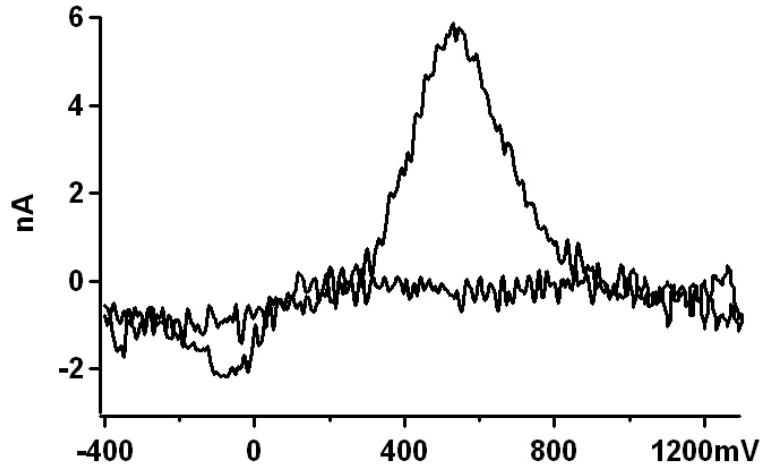

Figure 6.8: Background-subtracted voltammogram for the peak current of Fig. 6.6 which occurred at t=5.5 *s*. For the subtraction, the same background current as in Fig. 6.7 was used.

μA. The same CFE and the same animal were used for both measurements. The amplitude of the measured oxidation current is larger for the 300 μA amplitude stimulating pulses, compared to the 100 μA amplitude pulses. A comparison of the oxidation currents in Figs. 6.6 and 6.9 indicates that the oxidation current does not depend linearly on the stimulating pulse amplitude.

6.4.2 Modified apparatus for data detection and amplification

To measure FSCV currents *in vivo*, the data detection system is required to have a high dynamic range due to the very large capacitive background currents (black trace of Fig. 6.11A) generated at the interface between the CFE and the electrolyte (brain extracellular matrix), when fast voltage ramps are applied to the CFE. The redox current generates only a small change on top of the background current (dashed red trace of Fig. 6.11A). In wired setups, the amplifier supply voltage is typically ±10 V, and the gain is adjusted such that the redox current is

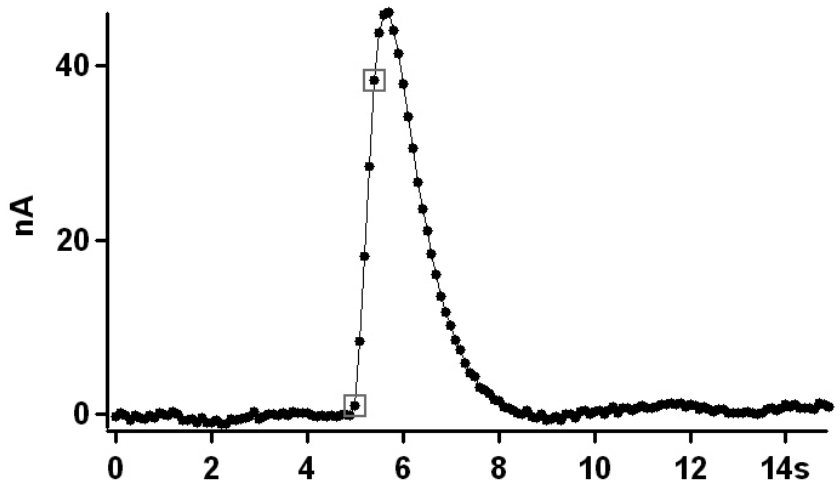

Figure 6.9: *In vivo* recording of CFE current sampled at the +662 *mV* applied potential and plotted versus time. The two gray squares indicate the duration of the stimulating pulses (24 bipolar pulses, at 60 *Hz* frequency and with 300 μA amplitude).

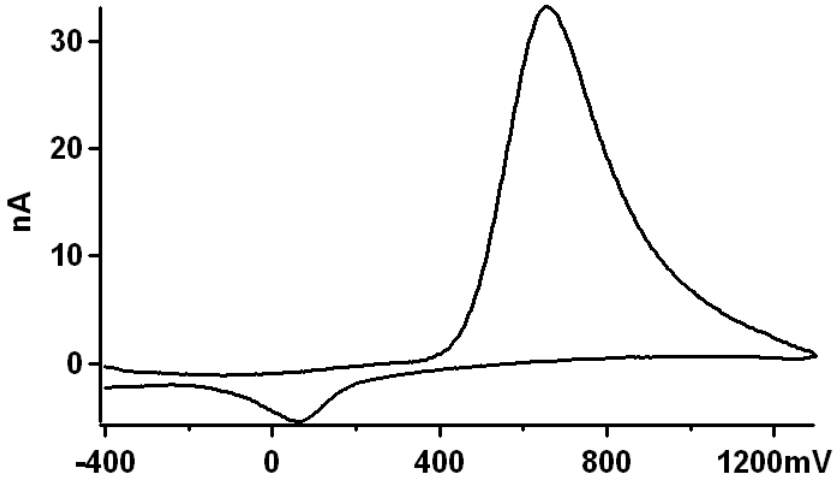

Figure 6.10: The current of the first 50 (0-4.9 *s*) voltammetric cycles of Fig. 6.9 was averaged to construct the background current. The current for 15 voltammetric cylces starting at 5.2 *s* was averaged to construct the DA signal. The difference (redox minus background) of the two plotted versus the applied potential (background-subtracted voltammogram).

well above noise levels and background-subtracted voltammograms of DA are clearly detected (Fig. 6.11B). A wireless device, however, must operate with a

battery, which typically generates a voltage of ~3 V. In this case the dynamic range requirement becomes a significant limitation.

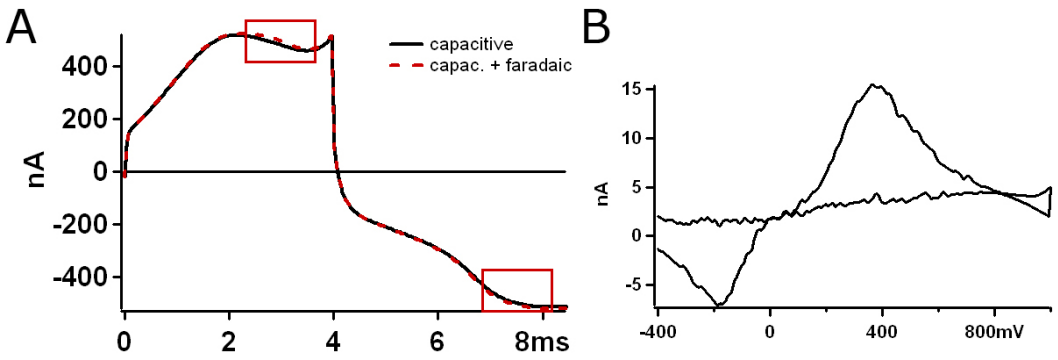

Figure 6.11: (A) FSCV current for a CFE in the buffer solution containing 0 μM (black trace) and 1 μM DA (dashed red trace) respectively. The CFE was connected to an EPC-8 amplifier (HEKA-Elektronik, Germany). (B) Background-subtracted voltammogram.

To lower the dynamic range requirement, the electronic device was modified, such that in addition to the low-noise amplifier (LNA) that detected the CFE current, a second identical LNA was connected to the series combination of an electrical resistor R_C and a capacitor C_C (Fig. 6.12). This series combination models the Debye double layer at the CFE-electrolyte interface. The capacitance value was chosen as $C_C = 1\ nF$, because this value is typical for *in vivo* recordings during which 100 μm long CFEs (2.5 μm radius tip) are typically used. The double layer capacitance of the electrode is approximately: $C = \epsilon\epsilon_0 \frac{A}{d} = 1.1\ nF$, where A is the electrode area, d the Debye length (~1 nm for physiological saline), ϵ_0 the permittivity of vacuum (8.85 pF/m), and $\epsilon = 80$ the dielectric constant of water.

Fig. 6.13A shows the FSCV current of the CFE utilized in the measurements of Fig. 6.11. The CFE was placed in the buffer solution and connected to the electronic circuit of Fig. 6.12. When the voltage ramps were applied, both the

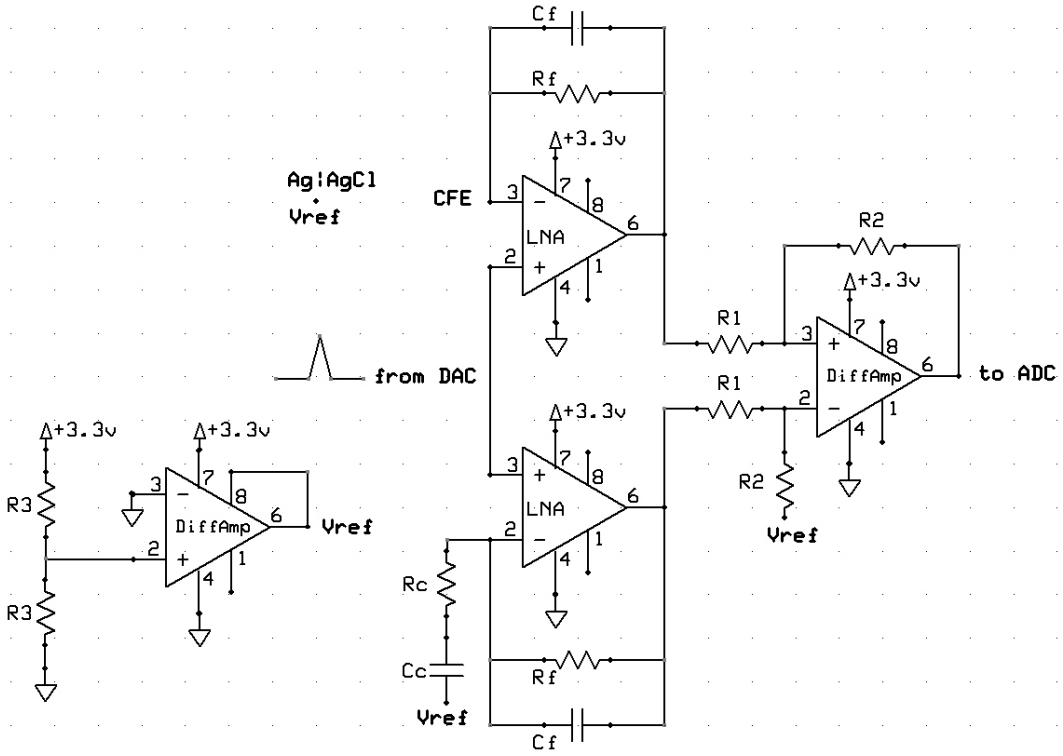

Figure 6.12: Design of the electronic circuit for wireless FSCV. The circuit includes a capacitance compensation to lower the dynamic range requirement. Values of passive components: $R_f = 1M\Omega, C_f = 25pF, R_1 = 40k\Omega, R_2 = 80k\Omega, R_3 = 2.7k\Omega, R_C = 100k\Omega, C_C = 1nF$. The low-noise amplifiers are two LMV751 opamps (National Semiconductor, Santa Clara, CA), while the differential amplifiers are both in the same INA2132 integrated circuit (Texas Instruments, Dallas, TX). These components were as in [118].

capacitor at the CFE-electrolyte interface and the compensation capacitor C_C are simultaneously charged and discharged. The background current (black trace of Fig. 6.13A) is reduced ~5-fold by the capacitance compensation, and as a result the redox current (red trace of Fig. 6.13A) is clearly apparent (compare to Fig. 6.11A). The reduction of the background current allows three times higher amplification of the measured current at the subsequent stage (differential amplifier at the right of Fig. 6.12). The background-subtracted voltammogram averaged over a 10 s period is shown in Fig. 6.13B.

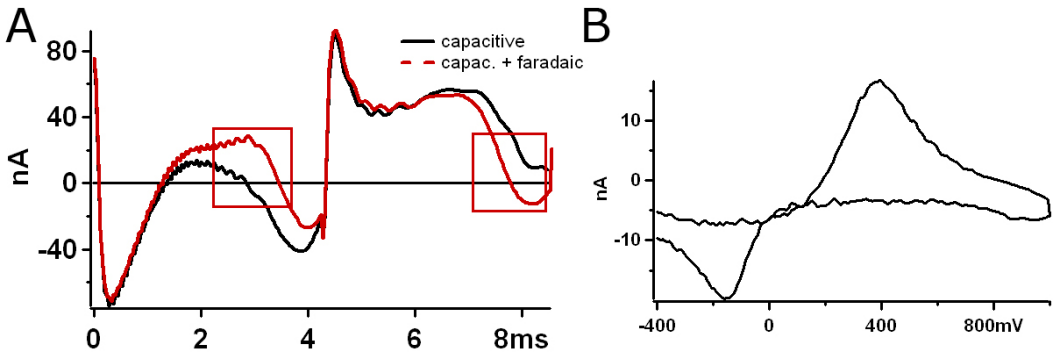

Figure 6.13: (A) FSCV current for a CFE in the buffer containing 0 μM (black trace) and 1 μM DA (red trace) respectively. The CFE was connected to the electronic circuit of Fig. 6.12. (B) Background-subtracted voltammogram averaged over a 10 s segment. The same CFE as in Fig. 6.11 was used.

The circuit of Fig. 6.12 also includes a differential amplifier (lower left section) which applies a constant potential to the Ag|AgCl reference electrode. This reference potential is necessary in order to apply a bipolar voltage ramp and measure both positive and negative (oxidation and reduction) currents. The noise levels of the currents measured with the circuit of Fig. 6.12 are relatively high as can be seen in the voltammetric current recordings of Fig. 6.13A. The reasons for the higher noise levels are still unclear.

6.4.3 Wireless transmission of FSCV data

In order to correlate neurotransmitter action with behavior, it is necessary to allow animals to freely move during electrochemical recordings. When the animal's head is connected with wires to the detection apparatus, the animal is restrained and not completely free to move. Therefore it is desirable to wirelessly transmit the recorded electrochemical data from the animal's brain to a recording device.

A setup for bidirectional wireless communication typically consists of a base station (BS) and a remote unit (RU). The BS is the immobile unit, while the RU is mounted on the mobile object. To allow maximal flexibility for the FSCV experiments, the BS and the RU communicate in a bidirectional wireless fashion. The potential waveform applied to the CFE is transmitted from the BS to the RU, while the measured FSCV current is transmitted from the RU to the BS.

Bluetooth technology has been used for wireless FSCV measurements [118]. For our experiments, we utilized a commercially available integrated chip (F2M03MLA, Free2Move, Halmstad, Sweden), which requires a supply potential of $3.1 - 3.6\ V$, and has 75 mA maximum current consumption during RF transmission. The F2M03MLA module contains 16-bit resolution analog-to-digital and digital-to-analog converters, an audio codec, and a Bluetooth wireless transceiver.

The analog input data are digitized and converted into A2DP (Advanced Audio Distribution Profile) format in the F2M03MLA module. The firmware currently available for the F2M03MLA module allows operation in A2DP format only in sink mode (receive) and not in source mode (transmit). Thus data in A2DP format are received by the RU, but not yet transmitted from the RU to the BS.

Fig. 6.14A shows the FSCV current of a CFE in a buffer containing 0 μM (black trace) and 1 μM DA (red trace) respectively. Fig. 6.14B shows the corresponding background-subtracted voltammogram.

The measured data was stored in a personal computer (PC), converted to A2DP format, and wirelessly transmitted from the PC to the RU using a Blue-

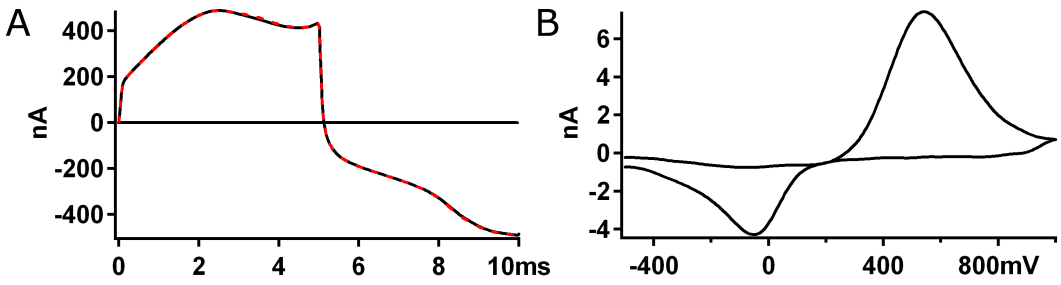

Figure 6.14: (A) (A) FSCV current measured in a buffer containing 0 μM (black trace) and 1 μM DA (red trace) respectively. (B) Corresponding background-subtracted voltammogram. Recordings were made with an EPC-8 amplifier (Heka Elektronik, Germany) connected to an ITC-18 data converter (Instrutech Corp, Bellmore, NY).

tooth Universal Serial Bus adapter (GBU221, IOGEAR Inc., Irvine, CA). The data received at the RU was again digitized with the ITC-18 data acquisition board and is shown in Fig. 6.15A and B. This serves as a proof of principle that the A2DP data transmission format is suitable for wireless *in vivo* FSCV, such that future implementation of reverse direction A2DP in the firmware should make the device a complete bidirectional telemetric system.

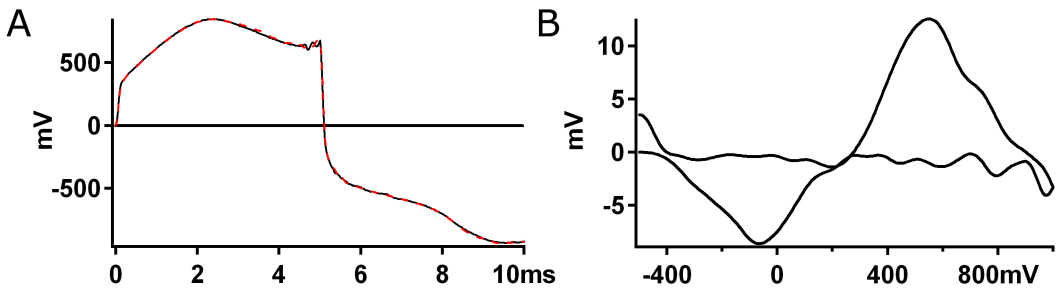

Figure 6.15: (A) The data of Fig. 6.14A after wireless transmission using the A2DP Bluetooth protocol. (B) Background-subtracted voltammogram of the received data averaged over a 10 s period.

6.5 Discussion

In vivo monitoring of neurotransmitter levels is a powerful tool which can illuminate the role of neurotransmitters in animal behavior. Detection of DA in the brain of freely moving rats was presented above. DA release was elicited by a stimulating current pulse train. Comparing Figs. 6.6 and 6.9, one can see that the oxidation current does not depend linearly on the stimulating pulse amplitude, presumably because neuronal stimulation has a non-linear dependence on the amplitude of the stimulating pulses.

The *in vivo* data presented above were obtained using a working CFE connected with wires to the data acquisition setup. To truly correlate neurotransmitter action with animal behavior, a wireless setup is needed, in order to provide complete freedom of motion to the research animals. The principal design of such a wireless device was presented. The device includes a simple capacitance compensation circuit, which subtracts directly on the chip part of the background FSCV current, increasing the signal to background ratio. This allows higher amplification of the data before their wireless transmission, thus improving the dynamic range. Although the wireless system tested in the present work is not yet bidirectional, future firmware improvements could make the device fully bidirectional, making it suitable for *in vivo* FSCV measurements.

CHAPTER 7

CONCLUSIONS AND OUTLOOK

Electrochemical measurements of oxidizable neurotransmitters such as dopamine, norepinephrine, epinephrine and serotonin have revealed a wealth of information from single vesicle release in cultured cells to neurosecretion measurements in the brain of living animals. This thesis presents technical development and experimental results on both levels.

In the present work, cell-attached capacitance measurements and amperometry were utilized in single chromaffin cells where either actin polymerization or nonmuscle myosin II function was inhibited. The results indicated that the rate of catecholamine secretion from single chromaffin vesicles is enhanced by the functions of F-actin and nonmuscle myosin II. These experiments also provided the first direct evidence that F-actin facilitates the expansion of the early fusion pore.

These novel findings indicate that exocytosis in neuroendocrine cells does not merely depend on the SNARE complex formation; there is rather a multitude of intracellular proteins that contribute to vesicle fusion and secretion. Uncovering the dynamic interplay between the various intracellular molecules that contribute to vesicle formation, fusion and release will shed more light into the details of the amount of neurotransmitters (quantal size) stored in single vesicles and their secretion time course. Both quantal size and transmitter release time course have huge biomedical significance. Several neurological diseases, such as Parkinson's disease and Alzheimer's disease, are correlated with the *in vivo* levels of neurotransmitters, regulated by vesicular release [119]. Understanding the fundamental mechanisms of vesicle formation and secretion will thus

facilitate the development of treatments for these devastating diseases. It could be possible to design drugs that would increase the amount of neurotransmitters stored within vesicles or accelerate the rate at which vesicles release their contents. In Parkinson's disease such treatments increase striatal dopamine levels thereby compensating at least in part for the reduction of dopamine due to neuronal degeneration.

The improved platinum electrodes (PtEs) developed in the present work resulted in mechanically robust and chemically stable devices, enriching the toolkit available to biophysicists, electrochemists and neuroscientists. Due to all their advantages demonstrated in Chapter 4, we anticipate the electrochemical detector arrays to be utilized in various experiments providing a better understanding of the molecular machinery underlying exocytosis in different cell types, including neurons. It could also be possible to use the SiO_2-insulated PtEs as a medical diagnostic tool, by chronically implanting them to monitor *in vivo* neurotransmitter levels. In the current work we developed a technique to pattern a chemical stimulus at a specific spatial location with micrometer precision, and electrochemically monitor catecholamine secretion as cellular response to the patterned stimulus. This technique could address issues such as cell membrane compartmentalization and spatiotemporal dynamics of stimulus-secretion coupling. For instance, in an experiment utilizing a multielectrode array, a chemical stimulus may be patterned near one electrochemical detector to stimulate a region of the cell near that electrode. Simultaneous amperometric recordings by the different electrodes in the array will indicate how secretion is localized relative to spatial localization of the patterned stimulus, indicating if local stimulation induces local release or if the stimulus spreads through the cell inducing release from different regions of the cell membrane.

Random walk simulations are well suited for modeling molecular motion in arbitrary geometries [43]. The RWS as well as the time-domain deconvolution developed in the present work revealed that in addition to secretion, the amperometric spikes measured with an ECD array are also affected by the diffusion of catecholamines towards the individual detectors. The data were fitted well using values of the diffusion constant smaller than that of catecholamines diffusing in an aqueous solution. The RWS indicated that the slow diffusion rate may by due to reversible binding of catecholamines onto the cell surface. The RWS is not restricted by any particular geometric constraint, it can thus be used for modeling catecholamine motion in a glass pipette in patch-amperometry experiments. RWS can also model neurotransmitter secretion *in vivo*, for example in a three dimensional reconstruction of the striatum.

Electrochemistry in the brain of research animals is a powerful tool which has allowed correlating the role of dopamine in behavior [115, 116]. The setups currently utilize a carbon fiber electrode connected to the detection apparatus with wires, which hinder animal motion. A wireless setup would thus be an invaluable tool for neuroscientists to investigate the role of neurotransmitters in behavior. The technique of capacitance compensation presented in Chapter 6 of this thesis should serve as a first step towards the development of such a device. Although more sophisticated methods of removing the capacitive background current of FSCV measurements have been developed [120], they would require complicated hardware and would be difficult to implement in wireless measurements. The method presented in Chapter 6 is a very simple one, which has minimum space and power consumption requirements. Coupled with a reasonably good bidirectional telemetry system, this method should enable the wireless monitoring of DA in the brain of freely behaving animals. In addi-

tion to serving as a fundamental research tool for neuroscientists, such a device could also serve as a therapeutic instrument. As an example, this device could be coupled with a deep brain stimulation system, which is a technique used for the real time treatment of Parkinson's disease patients. When the wireless DA sensor would detect critically low DA levels in the striatum, it would initiate the deep brain stimulation system, such that striatal DA levels would be increased before the patient starts experiencing the devastating symptoms of Parkinson's disease.

BIBLIOGRAPHY

[1] B. Alberts, D. Bray, J. Lewis, M. Raff, K. Roberts, and J.D. Watson. *Molecular Biology of the Cell.* Garland Publishing, Inc, 1983.

[2] R. Jahn, T. Lang, and T.C. Südhof. Membrane fusion. *Cell*, 112:519–533, 2003.

[3] R.B. Sutton, D. Fasshauer, R. Jahn, and A.T. Brunger. Crystal structure of a SNARE complex involved in synaptic exocytosis at 2.4Å resolution. *Nature*, 395:347–353, 1998.

[4] T. Söllner, S. Whiteheart, M. Brunner, H. Erdjument-Bromage, M. Geromanos, P. Tempst, and J.E. Rothman. SNAP receptors implicated in vesicle targeting and fusion. *Nature*, 362:318–323, 1993.

[5] J. Rizo and T.C. Südhof. SNAREs and Munc18 in synaptic vesicle fusion. *Nature Reviews Neuroscience*, 3:641–653, 2002.

[6] M. Lindau and G. Alvarez de Toledo. The fusion pore. *Biochimica et Biophysica Acta*, 1641:167–173, 2003.

[7] E.D. Korn, M.A. Atkinson, H. Brzeska, J.A. Hammer 3rd, G. Jung, and T.J. Lynch. Structure-function studies on Acanthamoeba myosins IA, IB, and II. *Journal of Cellular Biochemistry*, 36:37–50, 1988.

[8] P.A. Garris, J.R. Christensen, G.V. Rebec, and R.M. Wightman. Real-time measurement of electrically evoked extracellular dopamine in the striatum of freely moving rats. *Journal of Neurochemistry*, 68:152–161, 1997.

[9] D.L. Robinson, A. Hermans, A.T. Seipel, and R.M. Wightman. Monitoring rapid chemical communication in the brain. *Chemical Reviews*, 108:2554–2584, 2008.

[10] P. Fatt and B. Katz. An analysis of the end-plate potential recorded with an intracellular electrode. *Journal of Physiology*, 115:320370, 1951.

[11] D. Axelrod, N.L. Thompson, and T.P. Burghardt. Total internal inflection fluorescent microscopy. *Journal of Microscopy*, 129:19–28, 1983.

[12] M.D. Wang and D. Axelrod. Time-lapse total internal reflection fluorescence video of acetylcholine receptor cluster formation on myotubes. *Developmental Dynamics*, 201:29–40, 1994.

[13] J.A. Steyer, H. Horstmann, and W. Almers. Transport, docking and exocytosis of single secretory granules in live chromaffin cells. *Nature*, 388:474–478, 1997.

[14] D. Axelrod. Selective imaging of surface fluorescence with very high aperture microscope objectives. *Journal of Biomedical Optics*, 6:6–13, 2001.

[15] M.W. Allersma, M.A. Bittner, D. Axelrod, and R.W. Holz. Motion matters: secretory granule motion adjacent to the plasma membrane and exocytosis. *Molecular Biology of the Cell*, 17:2424–438, 2006.

[16] J.M. Fernandez, E. Neher, and B.D. Gomperts. Capacitance measurements reveal stepwise fusion events in degranulating mast cells. *Nature*, 312:453–455, 1984.

[17] L.J. Breckenridge and W. Almers. Currents through the fusion pore that forms during exocytosis of a secretory vesicle. *Nature*, 328:814–817, 1987.

[18] J. Zimmerberg, M. Curran, F.S. Cohen, and M. Brodwick. Simultaneous electrical and optical measurements show that membrane fusion precedes secretory granule swelling during exocytosis of beige mouse mast cells. *PNAS*, 84:1585–1589, 1987.

[19] M. Lindau. Time-resolved capacitance measurements: monitoring exocytosis in single cells. *Quarterly Reviews of Biophysics*, 24:75–101, 1991.

[20] K. Lollike, N. Borregaard, and M. Lindau. The exocytotic fusion pore of small granules has a conductance similar to an ion channel. *Journal of Cell Biology*, 129:99–104, 1995.

[21] K. Debus and M. Lindau. Resolution of patch capacitance recordings and of fusion pore conductances in small vesicles. *Biophysical Journal*, 78:2983–2997, 2000.

[22] X. Han, C.T. Wang, J. Bai, E.R. Chapman, and M.B. Jackson. Transmembrane segments of syntaxin line the fusion pore of Ca^{2+}-triggered exocytosis. *Science*, 304:289–292, 2004.

[23] L. He, X.S. Wu, R. Mohan, and L.G. Wu. Two modes of fusion pore opening revealed by cell-attached recordings at a synapse. *Nature*, 444:102–105, 2006.

[24] R.M. Wightman, J.A. Jankowski, R.T. Kennedy, D.T. Kawagoe, T.J. Schroeder, D.J. Leszczyszyn, J.A. Near, E.J. jr. Diliberto, and O.H. Viveros. Temporally resolved catecholamine spikes correspond to single vesicle release from individual chromaffin cells. *PNAS*, 88:10754–10758, 1991.

[25] R.H. Chow, Lv Rüden, and E. Neher. Delay in vesicle fusion revealed by electrochemical monitoring of single secretory events in adrenal chromaffin cells. *Nature*, 356:60–63, 1992.

[26] R.M. Wightman. Detection technologies. probing cellular chemistry in biological systems with microelectrodes. *Science*, 311:1570–1574, 2006.

[27] A. Albillos, G. Dernick, H. Horstmann, W. Almers, G. Alvarez de Toledo, and M. Lindau. The exocytotic event in chromaffin cells revealed by patch amperometry. *Nature*, 389:509–512, 1997.

[28] G. Dernick, L.W. Gong, L. Tabares, G. Alvarez de Toledo, and M. Lindau. Patch amperometry: high-resolution measurements of single-vesicle fusion and release. *Nature Methods*, 2:699–708, 2005.

[29] G. Dernick, G. Alvarez De Toledo, and M. Lindau. *The Patch Amperometry Technique: Design of a Method to Study Exocytosis of Single Vesicles. In: Electrochemical Methods for Neuroscience. Editors: Michael AC and Borland LM*. Boca Raton, FL: CRC Press, 2006.

[30] S.J. An and W. Almers. Tracking SNARE complex formation in live endocrine cells. *Science*, 306:1042–1046, 2004.

[31] G. Grynkiewicz, M. Poenie, and R.Y. Tsien. A new generation of Ca^{2+} indicators with greatly improved fluorescence properties. *Journal of Biological Chemistry*, 260:3440–3450, 1985.

[32] O.P. Hamill, A. Marty, E. Neher, B. Sakmann, and F.J. Sigworth. Improved patch-clamp technique for high-resolution current recording from cells and cell-free membrane patches. *Pflügers Archiv European Journal of Physiology*, 391:85–100, 1981.

[33] E. Neher and A. Marty. Discrete changes of cell membrane capacitance

observed under conditions of enhanced secretion in bovine adrenal chromaffin cells. *PNAS*, 79:6712–6716, 1982.

[34] G. Dernick, G. Alvarez de Toledo, and M. Lindau. Exocytosis of single chromaffin granules in cell-free inside-out membrane patches. *Nature Cell Biology*, 5:358–362, 2003.

[35] M. Lindau and E. Neher. Patch-clamp techniques for time-resolved capacitance measurements in single cells. *Pflügers Archiv European Journal of Physiology*, 411:137–146, 1988.

[36] F. Gonon, R. Cespuglio, J.L. Ponchon, M. Buda, M. Jouvet, R.N. Adams, and J.F. Pujol. In vivo continuous electrochemical determination of dopamine release in rat neostriatum. *C R Acad Sci Hebd Seances Acad Sci D*, 286:1203–1206, 1978.

[37] B. Sakmann and E. Neher. *Single-channel recording, 2nd edition*. Plenum Press, New York, 1995.

[38] A.J. Bard and L.R. Faulkner. *Electrochemical methods: fundamentals and applications*. New York: Wiley, 1980.

[39] K. Pihel, T.J. Schroeder, and R.M. Wightman. Rapid and selective cyclic voltammetric measurements of epinephrine and norepinephrine as a method to measure secretion from single bovine adrenal-medullary cells. *Analytical Chemistry*, 66:4532–4537, 1994.

[40] R.P. Feynman. There's plenty of room at the bottom. *Annual meeting of the American Physical Society*, 1959.

[41] A.F. Dias, G. Dernick, V. Valero, M.G. Yong, C.D. James, H.G. Craighead, and M. Lindau. An electrochemical detector array to study cell biology on the nanoscale. *Nanotechnology*, 13:285–289, 2002.

[42] I. Hafez, K. Kisler, K. Berberian, G. Dernick, V. Valero, M.G. Yong, H.G. Craighead, and M. Lindau. Electrochemical imaging of fusion pore openings by electrochemical detector arrays. *PNAS*, 102:13879–13884, 2005.

[43] H.C. Berg. *Random walks in biology, Expanded Edition*. Princeton, N.J.: Princeton University Press, 1993.

[44] M. Malacombe, M.F. Bader, and S. Gasman. Exocytosis in neuroendocrine

cells: new tasks for actin. *Biochimica et Biophysica Acta*, 1763:1175–1183, 2006.

[45] D. Aunis and M.F. Bader. The cytoskeleton as a barrier to exocytosis in secretory-cells. *Journal of Experimental Biology*, 139:253–266, 1988.

[46] M.L. Vitale, E.P. Seward, and J.M. Trifaro. Chromaffin cell cortical actin network dynamics control the size of the release-ready vesicle pool and the initial rate of exocytosis. *Neuron*, 14:353–363, 1995.

[47] S.D. Rose, T. Lejen, L. Casaletti, R.E. Larson, T.D. Pene, and J.M. Trifaro. Myosins II and V in chromaffin cells: myosin V is a chromaffin vesicle molecular motor involved in secretion. *Journal of Neurochemistry*, 85:287–298, 2003.

[48] P. Neco, D. Giner, S. Viniegra, R. Borges, A. Villarroel, and L.M. Gutierrez. New roles of myosin II during vesicle transport and fusion in chromaffin cells. *Journal of Biological Chemistry*, 279:27450–27457, 2004.

[49] P. Neco, C. Fernandez-Peruchena, S. Navas, L.M. Gutierrez, G. Alvarez de Toledo, and E. Ales. Myosin II contributes to fusion pore expansion during exocytosis. *Journal of Biological Chemistry*, 283:10949–10957, 2008.

[50] T.D. Parsons, J.R. Coorssen, H. Horstmann, and W. Almers. Docked granules, the exocytic burst, and the need for ATP hydrolysis in endocrine cells. *Neuron*, 15:1085–1096, 1995.

[51] K. Pihel, E.R. Travis, R. Borges, and R.M. Wightman. Exocytotic release from individual granules exhibits similar properties at mast and chromaffin cells. *Biophysical Journal*, 71:1633–1640, 1996.

[52] I.F. Sbalzarini and P. Koumoutsakos. Feature point tracking and trajectory analysis for video imaging in cell biology. *Journal of Structural Biology*, 151:182–195, 2005.

[53] H. Qian, M.P. Sheetz, and E.L. Elson. Single particle tracking. Analysis of diffusion and flow in two-dimensional systems. *Biophysical Journal*, 60:910–921, 1991.

[54] J.B. Manneville, S. Etienne-Manneville, P. Skehel, T. Carter, D. Ogden, and M. Ferenczi. Interaction of the actin cytoskeleton with microtubules regu-

lates secretory organelle movement near the plasma membrane in human endothelial cells. *Journal of Cell Science*, 116:3927–3938, 2003.

[55] A.F. Straight, A. Cheung, J. Limouze, I. Chen, N.J. Westwood, J.R. Sellers, and T.J. Mitchison. Dissecting temporal and spatial control of cytokinesis with a myosin II inhibitor. *Science*, 299:1743–1747, 2003.

[56] E.V. Mosharov and D. Sulzer. Analysis of exocytotic events recorded by amperometry. *Nature Methods*, 2:651–658, 2005.

[57] J. Xu, X.P. Gao, R. Ramchandran, Y.Y. Zhao, S.M. Vogel, and A.B. Malik. Nonmuscle myosin light-chain kinase mediates neutrophil transmigration in sepsis-induced lung inflammation by activating beta2 integrins. *Nature Immunology*, 9:880–886, 2008.

[58] L.W. Gong, G. Alvarez de Toledo, and M. Lindau. Exocytotic catecholamine release is not associated with cation flux through channels in the vesicle membrane but Na^+ influx through the fusion pore. *Nat Cell Biol*, 9:915–922, 2007.

[59] R.H. Austin, K. Beeson, L. Ieisenst, H. Frauenfe, I.C. Gunsalus, and V.P. Marshall. Dynamics of carbon-monoxide binding by heme proteins. *Science*, 181:541–543, 1973.

[60] R.H. Austin, K.W. Beeson, L. Eisenstein, H. Frauenfelder, and I.C. Gunsalus. Dynamics of ligand binding to myoglobin. *Biochemistry*, 14:5355–5373, 1975.

[61] T. Lang, I. Wacker, I. Wunderlich, A. Rohrbach, G. Giese, T. Soldati, and W. Almers. Role of actin cortex in the subplasmalemmal transport of secretory granules in PC-12 cells. *Biophysical Journal*, 78:2863–2877, 2000.

[62] A.P. Somlyo and A.V. Somlyo. Ca^{2+} sensitivity of smooth muscle and nonmuscle myosin II: modulated by G proteins, kinases, and myosin phosphatase. *Physiol Rev*, 83:1325–1358, 2003.

[63] H. Tokuoka and Y. Goda. Myosin light chain kinase is not a regulator of synaptic vesicle trafficking during repetitive exocytosis in cultured hippocampal neurons. *Journal of Neuroscience*, 26:11606–11614, 2006.

[64] J.R. Monck, A.F. Oberhauser, G. Alvarez de Toledo, and J.M. Fernandez.

Is swelling of the secretory granule matrix the force that dilates the exocytotic fusion pore? *Biophysical Journal*, 59:39–47, 1991.

[65] M. Lindau and H. Rüppel. Evidence for conformational substates of rhodopsin from kinetics of light-induced charge displacement. *Photobiochemistry and Photobiophysics*, 5:219–228, 1983.

[66] R. Fernandez-Chacon and G. Alvarez de Toledo. Cytosolic calcium facilitates release of secretory products after exocytotic vesicle fusion. *FEBS Letters*, 363:221 – 225, 1995.

[67] J. Hartmann and M. Lindau. A novel Ca^{2+} - dependent step in exocytosis subsequent to vesicle fusion. *FEBS Letters*, 363:217 – 220, 1995.

[68] S. Scepek, J.R. Coorssen, and M. Lindau. Fusion pore expansion in horse eosinophils is modulated by Ca^{2+} and protein kinase C via distinct mechanisms. *European Molecular Biology Organization Journal*, 17:4340–4345, 1998.

[69] J.A. Jankowski, T.J. Schroeder, E.L. Ciolkowski, and R.M. Wightman. Temporal characteristics of quantal secretion of catecholamines from adrenal medullary cells. *Journal of Biological Chemistry*, 268:14694–14700, 1993.

[70] R.M. Wightman, K.P. Troyer, M.L. Mundorf, and R. Catahan. The association of vesicular contents and its effects on release. *Ann N Y Acad Sci*, 971:620–626, 2002.

[71] T.J. Schroeder, R. Borges, J.M. Finnegan, K. Pihel, C. Amatore, and R.M. Wightman. Temporally resolved, independent stages of individual exocytotic secretion events. *Biophysical Journal*, 70:1061–1068, 1996.

[72] F. Felmy. Modulation of cargo release from dense core granules by size and actin network. *Traffic*, 8:983–997, 2007.

[73] M.S. Montesinos, J.D. Machado, M. Camacho, J. Diaz, Y.G. Morales, D. Alvarez de la Rosa, E. Carmona, A. Castaneyra, O.H. Viveros, D.T. O'Connor, S.K. Mahata, and R. Borges. The crucial role of chromogranins in storage and exocytosis revealed using chromaffin cells from chromogranin A null mouse. *Journal of Neuroscience*, 28:3350–3358, 2008.

[74] A.M. Sokac, C. Co, J. Taunton, and W. Bement. Cdc42-dependent actin polymerization during compensatory endocytosis in Xenopus eggs. *Nature Cell Biology*, 5:727–732, 2003.

[75] C. Amatore, Y. Bouret, and L. Midrier. Time-resolved dynamics of the vesicle membrane during individual exocytotic secretion events, as extracted from amperometric monitoring of adrenaline exocytosis from chromaffin cells. *Chemistry-a European Journal*, 5:2151–2162, 1999.

[76] S. Gasman, S. Chasserot-Golaz, M. Malacombe, M. Way, and M.F. Bader. Regulated exocytosis in neuroendocrine cells: a role for subplasmalemmal Cdc42/N-WASP-induced actin filaments. *Molecular Biology of the Cell*, 15:520–531, 2004.

[77] C. Desnos, J.S. Schonn, S. Huet, V.S. Tran, A. El-Amraoui, G. Raposo, I. Fanget, C. Chapuis, G. Menasche, G. de Saint Basile, C. Petit, S. Cribier, J.P. Henry, and F. Darchen. Rab27A and its effector MyRIP link secretory granules to F-actin and control their motion towards release sites. *Journal of Cell Biology*, 163:559–570, 2003.

[78] B.W. Doreian, T.G. Fulop, and C.B. Smith. Myosin II activation and actin reorganization regulate the mode of quantal exocytosis in mouse adrenal chromaffin cells. *Journal of Neuroscience*, 28:4470–4478, 2008.

[79] K. Berberian, A.J. Torres, Q. Fang, K. Kisler, and M. Lindau. F-actin and myosin II accelerate catecholamine release from chromaffin granules. *Journal of Neuroscience*, 29:863–870, 2009.

[80] E. Pothos, M. Desmond, and D. Sulzer. L-3,4-Dihydroxyphenylalanine increases the quantal size of exocytotic dopamine release in vitro. *Journal of Neurochemistry*, 66:629–636, 1996.

[81] E.H. Jaffe, A. Marty, A. Schulte, and R.H. Chow. Extrasynaptic vesicular transmitter release from the somata of substantia nigra neurons in rat midbrain slices. *Journal of Neuroscience*, 18:3548–3553, 1998.

[82] E.N. Pothos, V. Davila, and D. Sulzer. Presynaptic recording of quanta from midbrain dopamine neurons and modulation of the quantal size. *Journal of Neuroscience*, 18:4106–4118, 1998.

[83] R.G. Staal, E.V. Mosharov, and D. Sulzer. Dopamine neurons release transmitter via a flickering fusion pore. *Nature Neuroscience*, 7:341–346, 2004.

[84] T.L. Colliver, E.J. Hess, E.N. Pothos, D. Sulzer, and A.G. Ewing. Quantitative and statistical analysis of the shape of amperometric spikes recorded from two populations of cells. *Journal of Neurochemistry*, 74:1086–1097, 2000.

[85] X. Sun and K.D. Gillis. On-chip amperometric measurement of quantal catecholamine release using transparent indium tin oxide electrodes. *Analytical Chemistry*, 78:2521–2525, 2006.

[86] X. Chen, Y. Gao, M. Hossain, S. Gangopadhyay, and K.D. Gillis. Controlled on-chip stimulation of quantal catecholamine release from chromaffin cells using photolysis of caged Ca^{2+} on transparent indium-tin-oxide microchip electrodes. *Lab on a Chip*, 8:161–169, 2008.

[87] M. Lindau and O. Nüβe. Pertussis toxin does not affect the time course of exocytosis in mast cells stimulated by intracellular application of GTP-γ-S. *FEBS Letters*, 222:317–321, 1987.

[88] E.V. Mosharov, L.W. Gong, B. Khanna, D. Sulzer, and M. Lindau. Intracellular patch electrochemistry: regulation of cytosolic catecholamines in chromaffin cells. *Journal of Neuroscience*, 23:5835–5845, 2003.

[89] R.M. Wightman, T.J. Schroeder, J.M. Finnegan, E.L. Ciolkowski, and K. Pihel. Time course of release of catecholamines from individual vesicles during exocytosis at adrenal medullary cells. *Biophysical Journal*, 68:383–390, 1995.

[90] M. Lindau and J.M. Fernandez. IgE-mediated degranulation of mast cells does not require the opening of ion channels. *Nature*, 319:150–153, 1986.

[91] J.W. Coleman, S.T. Holgate, M.K. Church, and R.C. Godfrey. Immunoglobulin E decapeptide-induced 5-hydroxytryptamine release from rat peritoneal mast cells. comparison with corticotropin-(1-24)-peptide, polyarginine, polylysine and antigen. *Biochemical Journal*, 198:615–619, 1981.

[92] B. Ilic and H.G. Craighead. Topographical patterning of chemically sensitive biological materials using a polymer-based dry lift off. *Biomedical Microdevices, pp 317-322*, 2000.

[93] D. Bruns and R. Jahn. Real-time measurement of transmitter release from single synaptic vesicles. *Nature*, 377:62–65, 1995.

[94] D.O. Wipf, E.W. Kristensen, M.R. Deakin, and R.M. Wightman. Fast-scan cyclic voltammetry as a method to measure rapid, heterogeneous electron-transfer kinetics. *Analytical Chemistry*, 60:306–310, 1988.

[95] J. Millar, J.J. O'Connor, S.J. Trout, and Z.L. Kruk. Continuous scan cyclic voltammetry (CSCV): a new high-speed electrochemical method for monitoring neuronal dopamine release. *Journal of Neuroscience Methods*, 43:109–118, 1992.

[96] M.R. Deakin, P.M. Kovach, K.J. Stutts, and R.M. Wightman. Heterogeneous mechanisms of the oxidation of catechols and ascorbic acid at carbon electrodes. *Analytical Chemistry*, 58:1474–1480, 1986.

[97] M.L. Heien, P.E. Phillips, G.D. Stuber, A.T. Seipel, and R.M. Wightman. Overoxidation of carbon-fiber microelectrodes enhances dopamine adsorption and increases sensitivity. *Analyst*, 128:1413–1419, 2003.

[98] H. Lee, S.M. Dellatore, W.M. Miller, and P.B. Messersmith. Mussel-inspired surface chemistry for multifunctional coatings. *Science*, 318:426–430, 2007.

[99] D.J. Leszczyszyn, J.A. Jankowski, O.H. Viveros, E.J. jr. Diliberto, J.A. Near, and R.M. Wightman. Nicotinic receptor-mediated catecholamine secretion from individual chromaffine cells. *Journal of Biological Chemistry*, 265:14736–14737, 1990.

[100] R.J. Forster, P. Loughman, and T.E. Keyes. Effect of electrode density of states on the heterogeneous electron-transfer dynamics of osmium-containing monolayers. *Journal of the American Chemical Society*, 122:11948–11955, 2000.

[101] M. Buda, F. Gonon, R. Cespuglio, M. Jouvet, and J.F. Pujol. In vivo electrochemical detection of catechols in several dopaminergic brain regions of anaesthetized rats. *European Journal of Pharmacology*, 73:61–68, 1981.

[102] M.K. Zachek, A. Hermans, R.M. Wightman, and G.S. McCarty. *Journal of Electroanalytical Chemistry*, 614:113120, 2008.

[103] M. Wu, D. Holowka, H.G. Craighead, and B. Baird. Visualization of plasma membrane compartmentalization with patterned lipid bilayers. *PNAS*, 101:13798–13803, 2004.

[104] S. Ayers, K.D. Gillis, M. Lindau, and B.A. Minch. Design of a CMOS potentiostat circuit for electrochemical detector arrays. *IEEE Transactions on Circuits and Systems I-Regular Papers*, 54:736–744, 2007.

[105] J.J. Burmeister, T.D. Coates, and G.A. Gerhardt. Multisite microelectrode arrays for measurements of multiple neurochemicals. *Conference Proceedings: IEEE Engineering in Medicing and Biology Society*, 7:5348–5351, 2004.

[106] J.L. Ponchon, R. Cespuglio, F. Gonon, M. Jouvet, and J.F. Pujol. Normal pulse polarography with carbon fiber electrodes for in vitro and in vivo determination of catecholamines. *Analytical Chemistry*, 51:1483–1486, 1979.

[107] C. Amatore, Y. Bouret, E.R. Travis, and R.M. Wightman. Adrenaline release by chromaffin cells: Constrained swelling of the vesicle matrix leads to full fusion at the ENS. *Angewandte Chemie International Edition*, 39:1952–1955, 2000.

[108] A. Einstein. The motion of elements suspended in static liquids as claimed in the molecular kinetic theory of heat. *Annalen Der Physik*, 17:549–560, 1905.

[109] G.E.P. Box and M.E. Muller. A note on the generation of random normal deviates. *Annals of Mathematical Statistics*, 29:610–611, 1958.

[110] G.A. Gerhardt and R.N. Adams. Determination of diffusion coefficients by flow injection analysis. *Analytical Chemistry*, 54:2618–2620, 1982.

[111] C. Nicholson and J.M. Phillips. Ion diffusion modified by tortuosity and volume fraction in the extracellular microenvironment of the rat cerebellum. *Journal of Physiology*, 321:225–257, 1981.

[112] B.D. Bath, D.J. Michael, B.J. Trafton, J.D. Joseph, P.L. Runnels, and R.M. Wightman. Subsecond adsorption and desorption of dopamine at carbon-fiber microelectrodes. *Analytical Chemistry*, 72:5994–6002, 2000.

[113] E. Laviron. The use of polarography and cyclic voltammetry for the study of redox systems with adsorption of the reactants - heterogeneous vs surface path. *Journal of Electroanalytical Chemistry*, 382:111–127, 1995.

[114] R.M. Wightman, E. Strope, P. Plotsky, and R.N. Adams. In vivo voltammetry: monitoring of dopamine metabolites in CSF following release by electrical stimulation. *Brain Research*, 159:55–68, 1978.

[115] P.E.M. Phillips, G.D. Stuber, M.L.A.V. Heien, R.M. Wightman, and R.M.

Carelli. Subsecond dopamine release promotes cocaine seeking. *Nature*, 422:614–618, 2003.

[116] D.L. Robinson, B.J. Venton, M.L.A.V. Heien, and R.M. Wightman. Detecting subsecond dopamine release with fast-scan cyclic voltammetry in vivo. *Clinical Chemistry*, 49:1763–1773, 2003.

[117] G. Paxinos and C. Watson. The rat brain in stereotaxic coordinates. *Elsevier Academic Press*, 2005.

[118] P.A. Garris, R. Ensman, J. Poehlman, A. Alexander, P.E. Langley, S.G. Sandberg, P.G. Greco, R.M. Wightman, and G.V. Rebec. Wireless transmission of fast-scan cyclic voltammetry at a carbon-fiber microelectrode: proof of principle. *Journal of Neuroscience Methods*, 140:103–115, 2004.

[119] J. Lotharius and P. Brundin. Pathogenesis of Parkinson's disease: Dopamine, vesicles and α-synuclein. *Nature Reviews Neuroscience*, 3:932–942, 2002.

[120] A. Hermans, R.B. Keithley, J.M. Kita, L.A. Sombers, and R.M. Wightman. Dopamine detection with fast-scan cyclic voltammetry used with analog background subtraction. *Analytical Chemistry*, 80:4040–4048, 2008.